# Contents

# 1. First feasibility experiment for EXL

It is a well-known fact that the study of light-ion induced direct reactions, like elastic and inelastic scattering, transfer, and charge-exchange reactions, provides important information on the structure of nuclei. Hence, elastic and inelastic scattering experiments with light projectiles like proton have been routinely performed in the past. Before having the radioactive ion beams (RIB), such studies were limited to the use of stable or long-lived nuclei as targets in normal kinematics experiments. But with the advent of RIB facilities there is a possibility to extend the nuclear structure investigations to exotic nuclei as well. In this way, virtually the whole chart of the nuclei opens up for research so that theoretical models can be tested and verified all the way up to the limits of nuclear existence: the proton and neutron drip lines [1]. In particular, using stored radioactive beams and exploiting reactions in inverse kinematics inside a storage ring using thin internal targets enables, comparing to investigations with external targets, high resolution measurements down to very low momentum transfers. This technique allows, in many cases, to deduce essential nuclear structure information. It also provides a gain in luminosity from accumulation and recirculation of the radioactive beams [2]. The high luminosities provided in these kinds of ring experiments allow measurements at very small momentum transfers with high accuracy; the very thin targets permit the low-energy scattered target-like recoil ions to make it through the target-beam interaction region and to enter the detectors installed around the target without major distortion of energy and angular resolution. The possibility of studying these low-energy recoil particles is especially important when getting away from the region of stable nuclei, since it will allow us to study the periphery of exotic nuclei. For example, one of the most outstanding discoveries was the finding that the nuclear matter may appear under certain conditions with a qualitatively new type of nuclear structure, so-called "halo" structure [3, 4, 5]. It magnifies, among other nuclear structure aspects, the importance of studying such systems in the limits of very low momentum transfers. Other aspects like the in-medium interactions in proton-neutron asymmetric nuclear matter, giant resonances with strength distributions totally different from those known in stable nuclei, the shell structure in nuclei of extreme proton-to-neutron asymmetry leading to disappearance of the known magic numbers and, in turn, to the appearance of new shell gaps could also be studied well in the low momentum transfer region. These were all the motivations to start with the design of a new detection system in the framework of the upcoming FAIR[1] facility [6]. In

[1] Facility for Antiproton and Ion Research

order to perform a feasibility study for the EXL[2] setup [7] at the NESR storage ring, a test experiment was set up at the existing storage ring ESR[3] in December 2005 at GSI Darmstadt, Germany. In this feasibility test, we used the ESR storage ring to study the reactions resulting from the interaction of a stable $^{136}$Xe beam with an internal hydrogen target. The test experiment was intended to investigate the performance of the detector systems and the background conditions in a realistic storage ring scenario.

## 1.1 Experimental setup

For the feasibility experiment, detector elements representing all the major detector systems of the future EXL setup, along with an internal hydrogen gas-jet target were installed at the ESR (Fig. 1.1). Most of the various detector elements in this experiment covered only a small fraction of the total available phase space. A $^{136}$Xe beam with an energy of 350 MeV/$A$ was injected into the ESR from the heavy-ion synchrotron SIS, periodically exposed to electron cooling and moderately bunched by an RF cavity. We had two bunches of totally 100 ns length; the circumference of the ESR storage ring was about 108 m ($\approx$ 500 ns). The beam storage lifetime was found to be about 30 min; on average more than $10^9$ ions were circulating with a revolution frequency of $2 \times 10^6$/s, scattering off the internal hydrogen gas-jet target (with a thickness of $\approx 10^{12}$ atoms/cm$^2$) which was installed inside the vacuum chamber [8]. The detector setup for fast ejectiles consisted of two arrays with a total of 15 organic scintillators, each coupled with an iron converter, for detection of fast neutrons and light charged particles which are detectable mostly at forward angles due to their relativistic velocities when being produced in beam-target interaction. The two scintillator arrays were installed at about 230 cm and 400 cm downstream from the target (Figs. 1.1 and 1.2). Every scintillator and iron element had a rectangular cuboid shape with the dimensions of $10 \times 50 \times 4$ cm$^3$ and $10 \times 50 \times 5$ cm$^3$, respectively. Each iron-scintillator couple was mounted in such a way that we had 4 cm of scintillator material in the beam direction preceded by 5 cm iron. In total we had eight iron-scintillator couples put together in a square-like frame making the first array and seven put together as a wall making the second array. For detection, identification, and fast timing of the beam-like reaction products we had a position sensitive silicon p-i-n diode (of 300 $\mu$m thickness and $45 \times 45$ mm$^2$ surface area) followed by a 1 mm thick scintillation detector. They were installed further downstream the target after the first dipole magnet in a movable vacuum pocket driven in and out of the beam tube. Furthermore, a multi-wire proportional chamber (MWPC) for detection of the product of atomic charge-exchange reactions and a photomultiplier (PM) for luminosity measurements were the other detector

[2] EXotic nuclei studied in Light-ion induced reactions

[3] Experimental Storage Ring

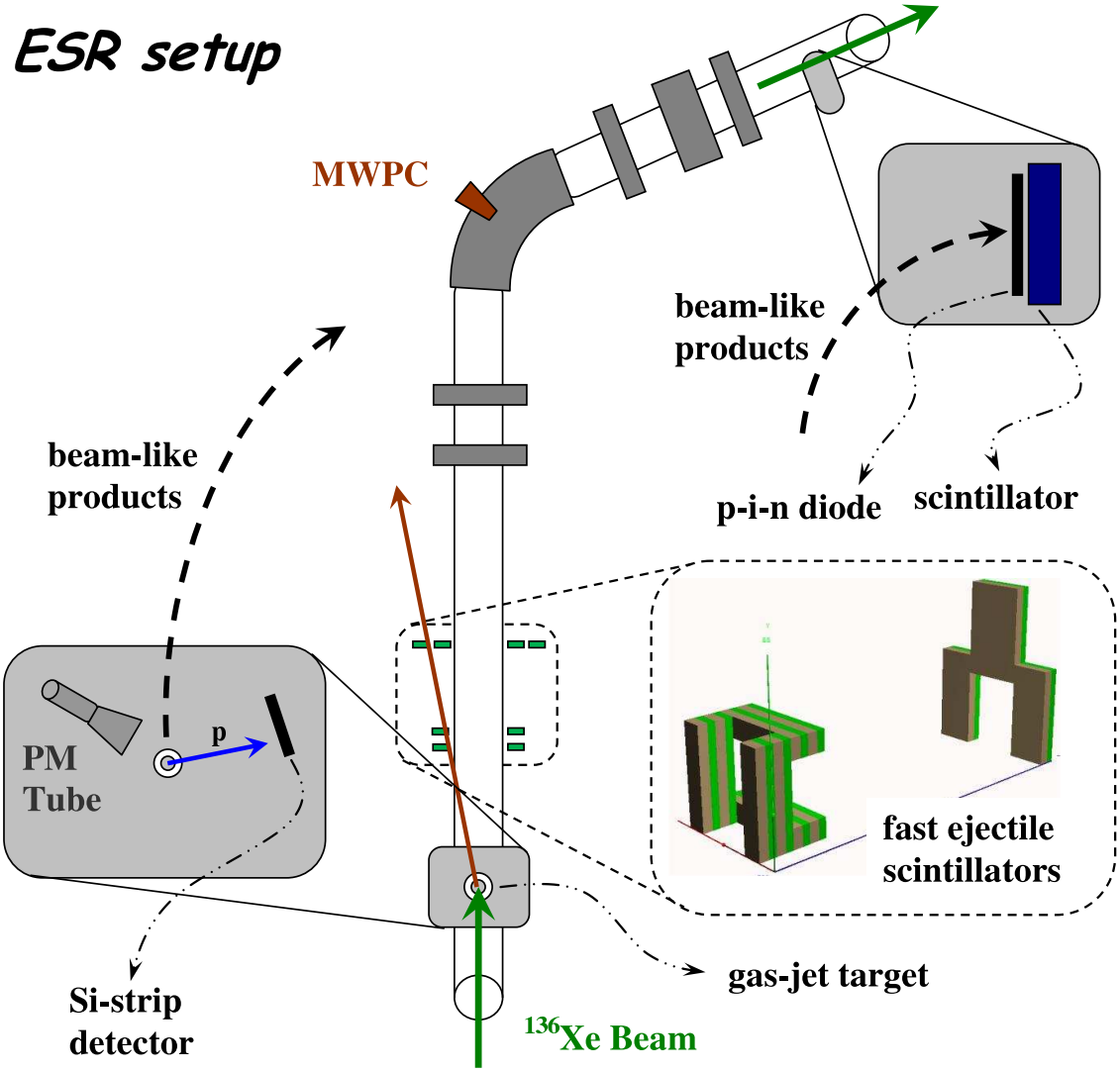


**Figure 1.1:** Experimental setup for the EXL test experiment performed at the storage ring ESR at GSI. For details see the text.

elements in the setup which were mounted outside the UHV (Ultra High Vacuum) reaction chamber. A UHV compatible single-sided Si-strip detector (Fig. 1.3) of 1 mm thickness and $40 \times 40$ mm$^2$ area (totally 40 strips) for detection of the target-like reaction products was the only detector element mounted inside the UHV of the vacuum chamber. The detector was designed [9] on the basis of a special vacuum compatible ceramic support and connected to the preamplifiers located outside of the reaction chambers via home-made copper wires with glass pearls acting as isolation. The Si-strip detector was read out in five groups of silicon strips, each of which with eight strips, and was used to detect the recoil protons. Energy deposition and position of the particles were reconstructed using a charge-division method

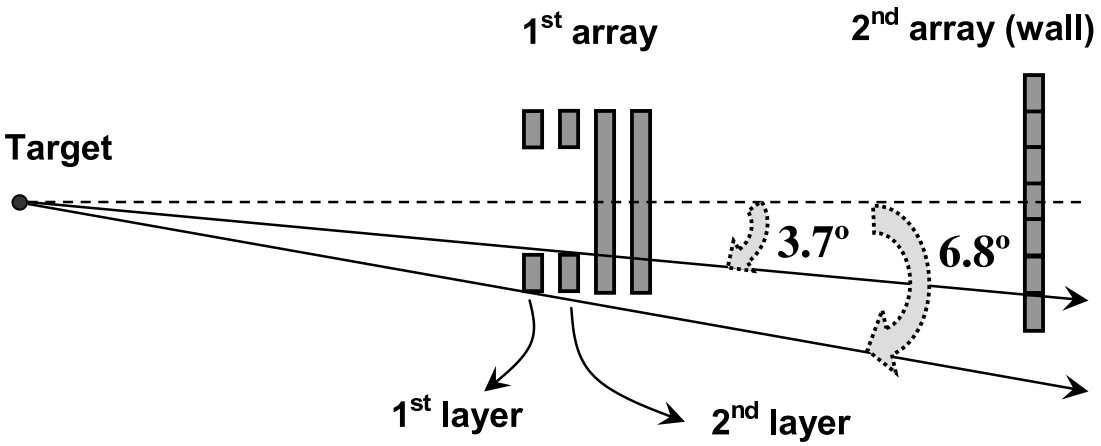


**Figure 1.2:** Top view of the organic scintillators used for detection of fast ejectiles. The angular ranges that are shown here represent the range of the scattering angle $\theta$ that covers the whole of the two detector layers labeled as "$1^{st}$ layer" and "$2^{nd}$ layer". Note that the iron converters in front of the scintillator bars are not shown here.

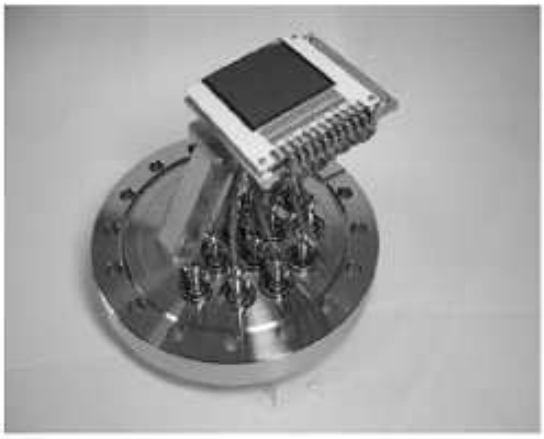

**Figure 1.3:** Photo of the UHV compatible Si-strip detector used in the EXL test experiment, together with the mounting flange and the wiring.

(Fig. 1.4). The detector was first tested with an $^{241}$Am $\alpha$-source and an energy resolution of 25 keV at 5 MeV (0.5%) was obtained (Fig. 1.5). It also showed a very good position resolution in terms of having well separated peaks (Fig. 1.6). The UHV conditions in the storage ring require any equipment placed inside to be resistant to high temperatures. The Si-strip detector was tested and it was shown that it can withstand temperatures of up to 200° Celsius [10].

Geometrically, the silicon detector edges were placed at angles of about 89.5° and 73.4° with respect to the beam direction ($z$-axis) in such a way that the normal vector to the detector surface, passing through the mid-point of the detector, points

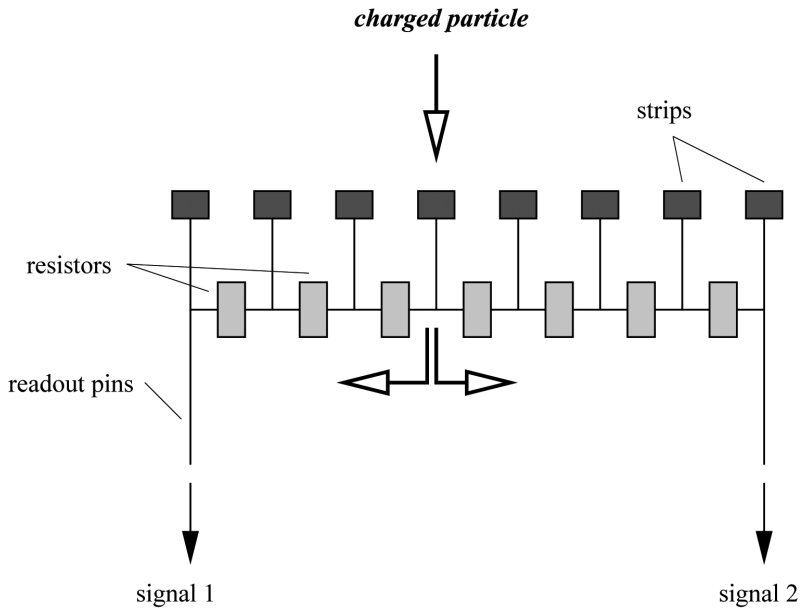


**Figure 1.4:** Charge-division readout for the Si-strip detector. The sum of signal 1 and signal 2 gives the energy deposited in the detector, and their ratio gives information about the coordinate of the particle [9].

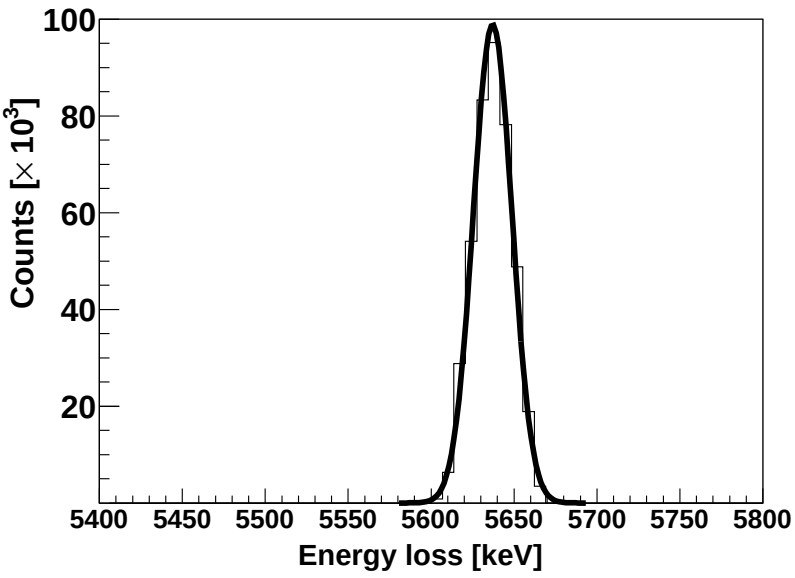


**Figure 1.5:** Energy spectrum of individual strips of the Si-strip detector, tested with an $^{241}$Am $\alpha$-source. The fit is a Gaussian with $mean = 5637.11 \pm 0.02$ keV and $sigma = 11.63 \pm 0.01$ keV [9].

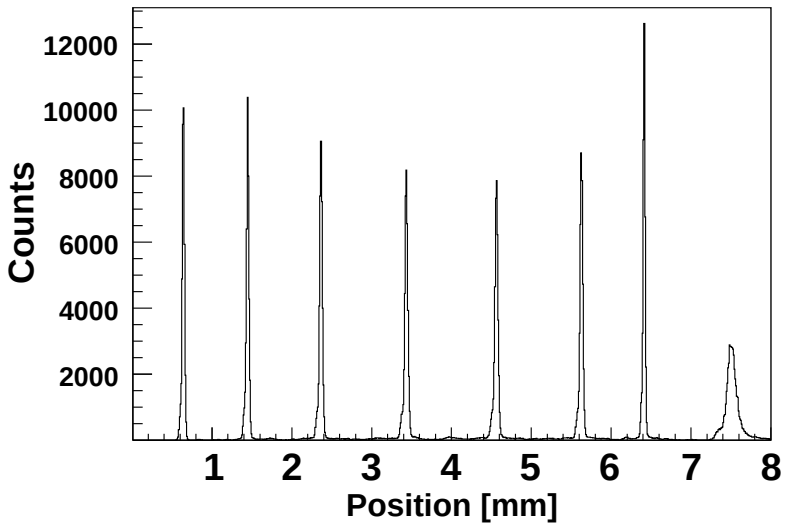


**Figure 1.6:** Position resolution of one group of the Si-strip detector, tested with an $^{241}$Am $\alpha$-source. The individual strips are clearly separated [9].

straight to the center of the interaction point inside the target chamber (Fig. 1.7); the distance of the mid-point of the detector square surface to the target point was about 14.3 cm. To protect the detector from the UV light coming from beam-target

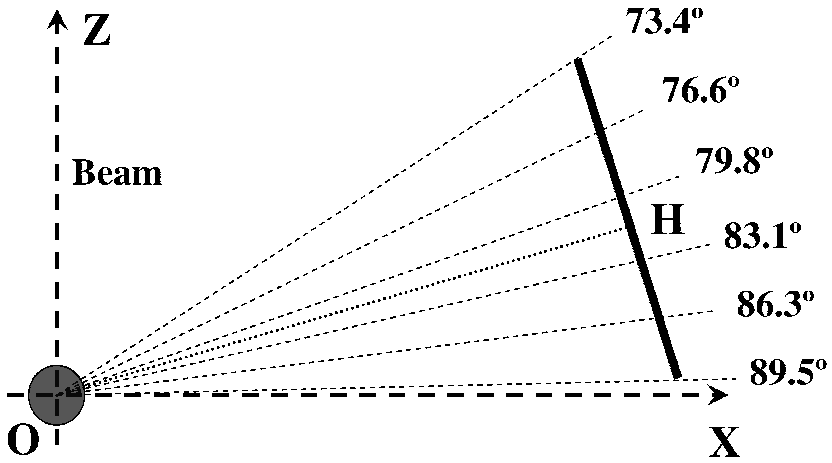


**Figure 1.7:** Position of the Si-detector with respect to the beam direction and the interaction-profile center O (OH is perpendicular to the mid-point of the detector and is about 14.3 cm long). The angular positions of the edges of the five groups of silicon strips with respect to the beam direction in laboratory frame (LAB) are shown as well. The circle drawn at the target point represents the extended target. Note that the dimensions are not to scale.

interactions, a thin nickel foil of 1 $\mu$m thickness was mounted in front of it.

## 1.2 Luminosity monitors

During the test experiment the beam was moved horizontally along the $x$-axis (perpendicular to the beam axis and the direction of the gas-jet injection) over the target in order to measure the extension of the interaction profile by different relative luminosity monitors. Three detector elements were used to measure the relative luminosity: a MWPC that was used to detect the ($Xe^{54+} \rightarrow Xe^{53+}$) beam ions deflected out of the central orbit of the ring after atomic charge exchange, a photomultiplier installed close to the target that was used to detect UV light produced from the beam-target interaction, and the silicon detector that was used to detect the recoil light particles. The interaction profiles obtained from these three detectors are shown in Fig. 1.8. The size of the target profile is obtained to be about 7.4 mm (FWHM) after unfolding the beam size which was estimated to be about 5 mm in diameter. The absolute luminosity was calculated measuring the beam intensity (by means of a current transformer) and the target density and reached the value of $(6 \pm 2) \times 10^{27}$ cm$^{-2}$ s$^{-1}$. The target density was constantly recorded during the experiment and the beam intensity was also registered during each period of data acquisition (run) with cooled and stabilized beam. For a specific run with the duration of 18976 seconds, the registered ESR beam current was about 6.16 mA and the average target density during the run time was obtained to be about $2.29 \times 10^{12}$/cm$^2$ (the target density was recorded every 3 seconds). This results in a luminosity of about $1.6 \times 10^{27}$ cm$^{-2}$ s$^{-1}$ for a fully stripped $^{136}_{54}$Xe. It is comparable to the luminosity calculated from the nominal values of the average number of ions circulating in the ring ($\approx 10^9$) and the revolution frequency of ions ($\approx 2$ MHz).

## 1.3 Heavy-ion and forward detector systems

The detection system for beam-like reaction products in the ESR test experiment consisted of a silicon p-i-n diode detector with a thickness of 300 $\mu$m and an area of $45 \times 45$ mm$^2$ followed by a thin scintillator of 1 mm thickness, which was used for triggering and fast timing of the beam-like particles. The system was installed about 21 m downstream from the target ($\approx 6$ m after the dipole magnets; see Fig. 1.1). The energy resolution of the scintillator did not allow for isotope separation; thus, the energy loss of heavy-ions was measured by the p-i-n diode. There was a possibility for the p-i-n diode to be moved in and out of the ring; during the refilling of the ESR ring and before the beam was cooled down we needed to bring out the detector in order to keep it away from any possible radiation damage caused by the direct intense beam. This feature allowed us as well to change the distance of the detector with respect to the center of the ring during the experiment (the surface of the detector was perpendicular to the beam direction). This way, one could scan for

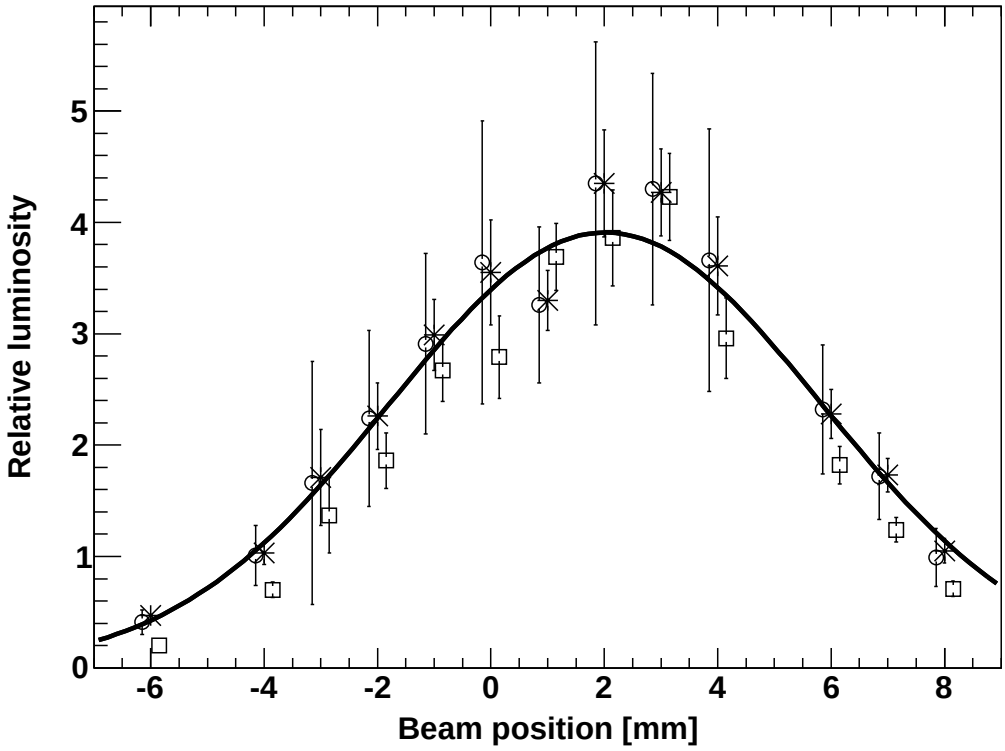


**Figure 1.8:** The interaction profile as measured by three different detection systems [11]. Asterisks, hollow squares, and hollow circles represent data from MWPC, Photomultiplier (PM), and Si-detector, respectively. For the sake of clarity, the data points of PM and Si-detector are shifted a bit to the right and the left side of the MWPC data, respectively. The fit is made to the MWPC data. The interaction profile has a width of $8.95 \pm 0.22$ mm (FWHM).

the heavy ions deflected from the beam direction, which are basically those which undergo an interaction.

Using the combination of the heavy-ion detection setup and the two series of scintillator assemblies, installed about 2.3 m and 4 m downstream of the target, one can identify different reaction channels like $(p, n)$, $(p, pxn)$, and $(p, 2pxn)$. In such reactions there is a possibility that the light ejectiles, emitted at forward angles due to relativistic velocities, are detected by the scintillator arrays in coincidence with the beam-like particles hitting the small area p-i-n diode. The result of such a coincidence measurement is shown in Fig. 1.9 (middle panel). We also used the Geant4 package to compare data with simulations. Comparing to the results of the simulations (bottom panel), it reveals the identification of at least two reaction channels, namely $^{136}$Xe$(p, np)$ and $^{136}$Xe$(p, 2p)$. The simulations are performed for $^{135}$Xe and $^{135}$I of 350 MeV/nucleon.

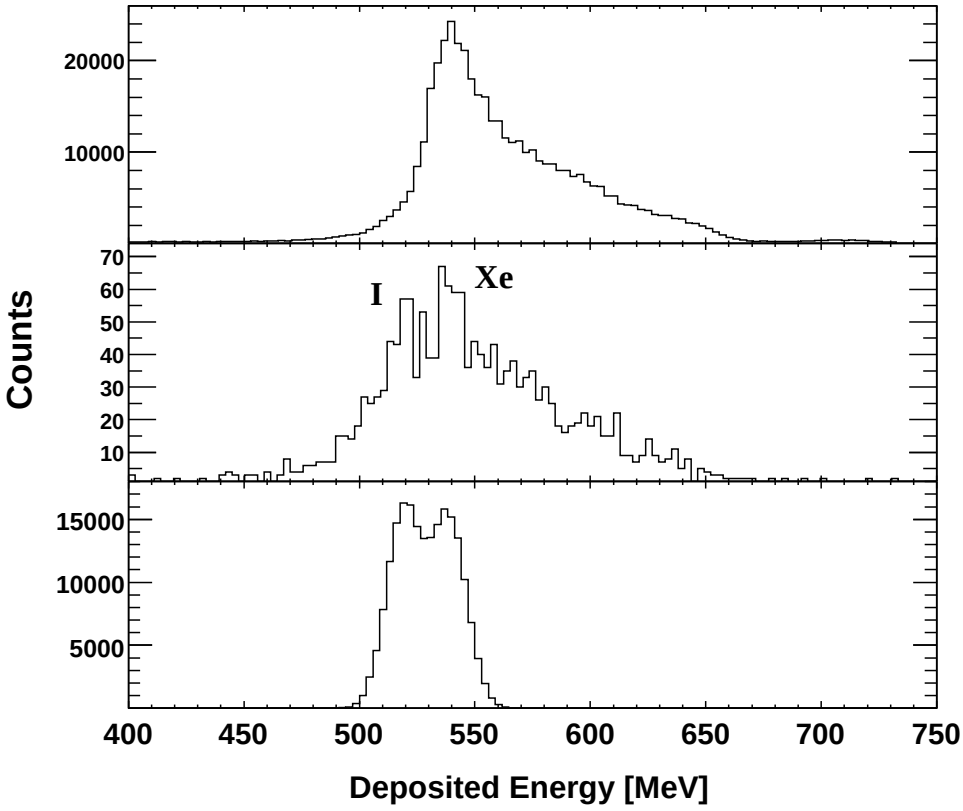


**Figure 1.9:** Identification of the reaction channels. The top panel shows the deposited energy (in MeV) of heavy ions in the p-i-n diode. Here, all the reaction products are registered. In the middle panel the reaction channels are differentiated through requiring a coincidence between two coupled detectors in the first series of scintillators (the two detectors are labeled as "$1^{st}$ layer" and "$2^{nd}$ layer" in Fig. 1.2). The spectrum of the first panel clearly shows the dominance of single channel, when compared to the middle panel in terms of the amount of statistics after requiring coincidence. The bottom panel shows the Geant4 simulation results for $^{135}$I and $^{135}$Xe ions of 350 MeV/nucleon that are detected by the p-i-n diode in the reaction channels $^{136}\mathrm{Xe}(p, 2p)$ and $^{136}\mathrm{Xe}(p, np)$, respectively. The left peak corresponds to I isotopes and the right one to Xe. The results of the upper two panels are calibrated to the simulations at the Xe peak.

Fig. 1.10 shows the deposited energy in the two consecutive scintillator layers of the first series of the fast ejectile scintillators (see Fig. 1.2). The results are from data analyses and simulations in Geant4 and Geant3 as well. The Geant3 results were obtained using the Virtual Monte Carlo (VMC)[4] package. The two simulation

[4] The Virtual Monte Carlo provides an abstract interface into the Monte Carlo transport codes: Geant3, Geant4 and Fluka. The user VMC based application, independent from the specific Monte Carlo codes, can then be run with all three simulation programs. [12]

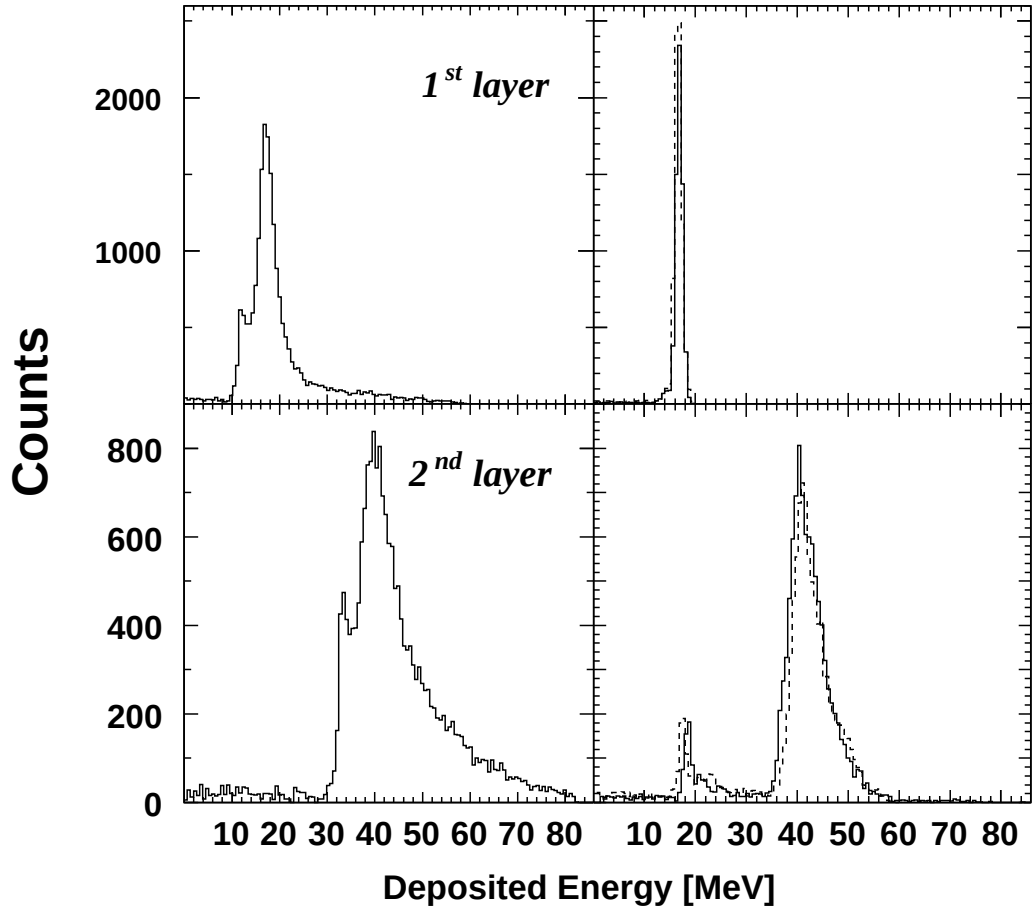


**Figure 1.10:** Deposited energy (in MeV) in the two consecutive layers of the first series of fast ejectile scintillators (shown in Fig. 1.2). On the left side the experimental spectra are shown. These spectra were obtained using the coincidence condition between the two scintillators labeled as "$1^{st}$ layer" and "$2^{nd}$ layer" in Fig. 1.2. Shown on the right are the corresponding simulation results of 350 MeV protons thrown isotropically. The solid and dotted histograms are the results of simulations with Geant4 and Geant3 (using the VMC package), respectively.

results of Geant3 and Geant4 are well comparable. There is a small peak, appearing at around 20 MeV, in the simulated spectrum of the "$2^{nd}$ layer" which is not present in the experimental data. It is built up by those protons which are scattered at angles around 3.7° (see Fig. 1.2) and hit the "$1^{st}$ layer" at the upper edge while they miss the first iron layer before this scintillator layer. Thus, the small peak appears more or less at the same position as that of the peak of the "$1^{st}$ layer", since it is built up by those events which effectively pass through one layer of iron placed right before the "$2^{nd}$ layer"; the peak of the "$1^{st}$ layer" is built up by events which essentially pass through the first iron layer before being registered by the "$1^{st}$ layer". The reason

that we do not see the small peak of the "$2^{nd}$ layer" in the data should be due to the misalignment of the iron-scintillator layers resulting in a geometry slightly different from what we implemented in the simulations (Fig. 1.2).

## 1.4 Silicon strip detector; data analysis and results

In the feasibility experiment we used different detector elements in order to study different reaction channels by installing them at appropriate positions. This way, we could detect various interaction products such as the light ejectiles and the projectile-like particles by (at least) partly covering the predicted phase space of the expected interactions. In order to study the elastic scattering channel of proton-$^{136}$Xe a UHV-compatible single-sided silicon strip detector of 1 mm thickness preceded by a 1 $\mu$m thick foil of nickel was installed inside the target chamber. Using the data from the first group of strips of the Si-strip detector, the $^{136}$Xe$(p,p)$ elastic scattering differential cross section was determined. Since the registered data by the silicon detector (including the first group) comprises the elastic as well as inelastic scattering events, the most appropriate way of studying the elastic scattering channel would be to measure the scattering angles with a good resolution. Although the silicon detector did not have a sufficient angular resolution, measurement of the proton elastic scattering cross section was possible using the first group of the Si-detector. This is because in the first group of strips primarily elastic scattering events are expected, since the inelastic scattering cross section is expected to be negligibly small at angles covering this group of strips. The solid angle coverage of the first group of strips can easily be calculated from Fig. 1.7 to be about 15.4 msr. Apart from the elastic scattering channel, there is a possibility to study the inelastic scattering channels provided that the solid angle covered by the Si-detector overlaps (at least partly) with the phase-space coverage of the respected channels.

### 1.4.1 Elastic scattering cross section

The elastic scattering cross section could be measured knowing that the first group of the Si detector is thick enough to effectively stop the elastically-scattered protons. This is also confirmed through simulations by calculating the deposited energy of elastically-scattered protons in this group. It is convenient to make use of the Mandelstam variable $-t$, which is defined as the square of the four momentum transfer. For the proton-$^{136}$Xe elastic scattering one can measure the cross section as a function of $-t$, which is expressed in terms of the proton scattering angle $\theta_p$ in LAB, as follows (Eq. A.49):

$$-t = 4\left(cp^{CM}\right)^2 \left(\frac{1}{1+\left(\gamma^{LAB}\right)^2 \tan^2\theta_p^{LAB}}\right).$$

It is also possible to express $-t$ in terms of the proton kinetic energy $K_p^{LAB}$ after collision with the heavy ion (Eq. A.52):

$$2m_pK_p^{LAB} = 2\left(cp^{CM}\right)^2\left(1+\cos\theta_p^{CM}\right) \equiv -t,$$

in which $m_p$, $K_p^{LAB}$, and $\theta_p^{CM}$ are the rest mass of the proton, kinetic energy of the recoil proton in the LAB frame, and scattering angle of proton in the center-of-mass frame (with its $z$-axis along the beam direction), respectively. In order to determine $-t$ from the recoil energy $K_p^{LAB}$ (since the angular resolution of the Si-detector was not good enough), the energy of the protons was corrected for their energy loss in the nickel foil which was mounted in front of the Si-detector. For a $^{136}$Xe beam energy of 350 MeV/nucleon, the parameters $cp^{CM}$ and $\gamma^{LAB}$ are obtained to be 0.8779 GeV and 1.3695, respectively. Figs. 1.11 and 1.12 show the experimental differential cross section (solid squares) as a function of $-t$, obtained using Eq. A.52 after correcting for the energy loss in the nickel foil and assuming that the recoil protons would not punch through in the first group of the Si-detector. The curve shows the prediction of the Glauber multiple-scattering theory for the elastic scattering cross section [16, 9]. For comparison, the simulations for point-like and extended interaction profiles are shown as well. The simulations were performed by implementing the geometry in a Geant4/VMC[5] code. Exploiting the VMC package allowed us to compare the Geant3 and Geant4 simulation results. We started from the Glauber theory for the elastic scattering cross section (solid curve) and used it as the generator for the elastic scattering channel. There is a cut-off in the simulations for the point-like target (asterisks in the top panel of Fig. 1.11) at about $-t = 0.0067$ (GeV/c)$^2$ which corresponds to the maximum scattering angle with respect to 90° in LAB at which a proton can be generated at the target point and still end up in the first group of silicon strips. In the absence of threshold, the simulation points should, in principle, start to show up from about $-t = 0.0001$ (GeV/c)$^2$, which corresponds to protons generated with kinetic energies of about 70 keV.

In Fig. 1.11 (bottom panel), the shape of the simulations for the extended interaction profiles agree reasonably well with the experimental results up to a value of about $-t = 0.011$ (GeV/c)$^2$, however, beyond this value of $-t$, there is an abrupt drop in the number of counts which is not compatible with the trend at lower $-t$ values. This might have to do with the operation of the Si-detector in this experiment. Fig. 1.12 compares the Geant4 simulation results for two extended interaction profiles with the experimental data. The simulated data points start to show up at around $-t = 0.0011$ (GeV/c)$^2$ due to the energy threshold of 500 keV of the silicon detector. This is also visible in the experimental data points at very low values of $-t$. The shapes of the simulations for the extended interaction profiles agree reasonably well (over the shown range of $-t$) with the experimental results; with the best agreement for a profile with a FWHM of 10.5 mm (star) in the $z$-direction. Due

[5] Virtual Monte Carlo

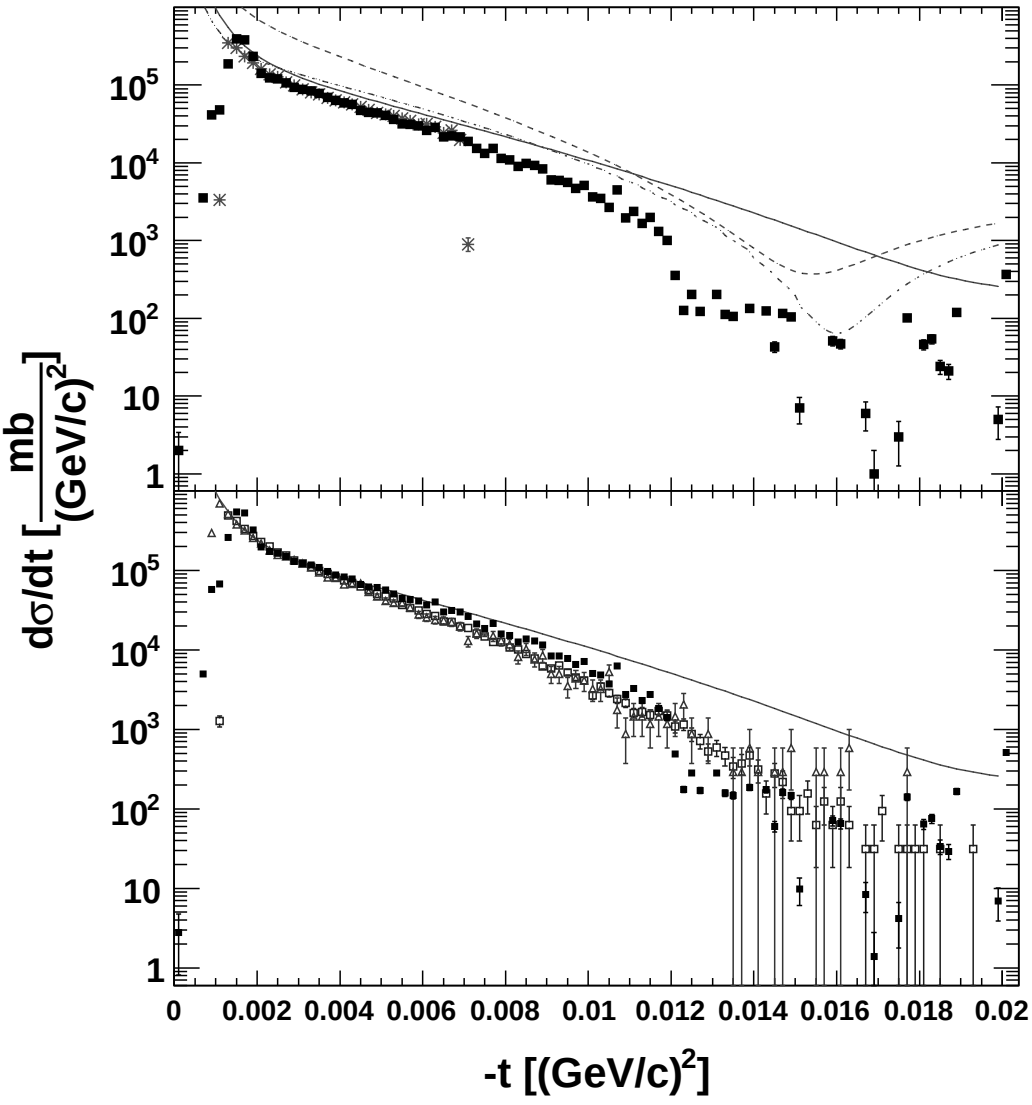


**Figure 1.11:** The curves show the proton-$^{136}$Xe elastic scattering cross section as a function of four-momentum-transfer squared, as predicted by the Glauber theory [13] (solid curve), Eikonal approximation (dashed curve [14]), and Edad2 calculation (dash-dotted curve [15]). The solid squares show the experimental absolute elastic scattering cross section. Top: The asterisks, which are normalized to data at $-t = 0.0031$ (GeV/c)$^2$, are the simulation results for the point-like target using the Glauber theory prediction. Bottom: the hollow squares and triangles are, respectively, Geant4 and Geant3 simulations (using the VMC package) which, together with the experimental data, are normalized to the theory curve at $-t = 0.0031$ (GeV/c)$^2$. The simulations for the extended interaction profile were done for an interaction profile of FWHM$_z$ = 7.4 mm, using the Glauber theory.

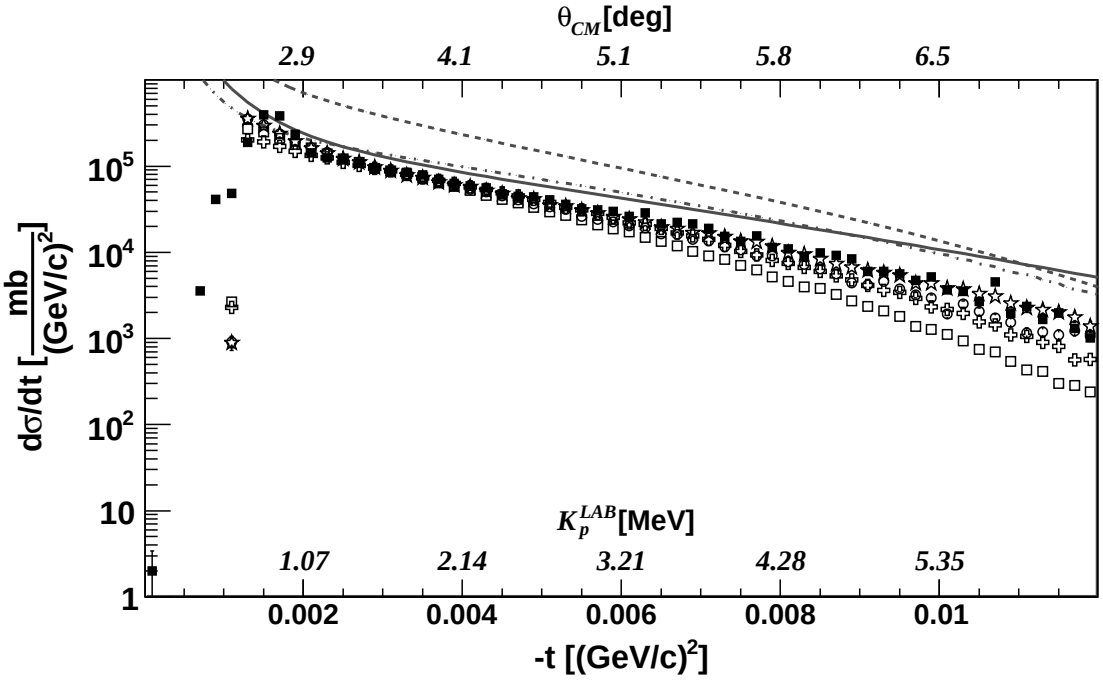


**Figure 1.12:** The curves and solid squares are the same as in Fig. 1.11 (top panel). Circles and stars show the simulation results, based on the Glauber theory (solid curve), for interaction profiles of $\mathrm{FWHM}_z = 7.4$ and 10.5 mm, respectively. Hollow squares and pluses show the simulation results for the elastic scattering cross section, based on the Eikonal approximation (dashed curve) and Edad2 calculation (dash-dotted curve), for an interaction profile of $\mathrm{FWHM}_z = 7.4$ mm. The simulation data points (obtained using Geant4) are normalized to the experiment at $-t = 0.0031$ $(\mathrm{GeV/c})^2$ and the error bars are statistical. $K_p^{LAB}$ is the recoil energy of the proton in the laboratory frame and $\theta_{CM}$ is the angle of the recoil proton in the center-of-mass frame with respect to $-\hat{z}$, in which $\hat{z}$ represents the direction of the beam.

to the small dimensions of the first group of the Si-detector and its placement close to 90° as well as the small extension of the interaction profile, (compared with its distance to the first group of silicon strips), the extension of the interaction profile along the $x$- or $y$-axis has a quite negligible effect on the shape of the simulations. This negligible effect was confirmed through simulations, even at the order of 1 cm for the $\mathrm{FWHM}_x$ or $\mathrm{FWHM}_y$. This shows that the main source in shaping the slope of the cross section is due to the much higher sensitivity of the cross section to the extension of the interaction profile along the $z$-axis rather than the other two axes. Nevertheless, the simulation results presented here are obtained using a full three-dimensional Gaussian profile as the position density of generation. For the four simulation results that are presented in Fig. 1.12, the Gaussian extension of the interaction profile along the $x$- and $y$-axes were assumed to be $\mathrm{FWHM}_x = 9.0$ mm (corresponding to a target extension of 7.4 mm) and $\mathrm{FWHM}_y = 5$ mm (since we

had a beam diameter of 5 mm and since we expect no folding with target along the direction of injection of the gas-jet target, namely along the $y$-axis, with the assumption of a rather uniform target density in the interaction region). Along the $z$-axis the position distribution for generating protons was chosen according to a Gaussian of $\mathrm{FWHM}_z = 7.4$ mm (circles and hollow squares) or $\mathrm{FWHM}_z = 10.5$ mm (stars).

In order to deduce a cross section from the data, the experimental data points must be unfolded for geometrical effects by using appropriate correction factors. The correction factors are inter-related to the geometrical acceptance of the first group of silicon strips and were calculated through simulations which will be discussed hereafter. In order to understand the descending behavior of the elastic scattering cross section, we can decompose the effects of various independent sources that have influence on the shape of the deduced cross section (solid squares in Fig. 1.12). The first source is the intrinsic shape of the cross section itself. The other source is the geometrical acceptance of the Si-detector for which we expect, for the specific geometry in our experiment, that more particles miss the detector at larger values of $-t$ (the effective solid angle is $t$-dependent). One can calculate the acceptance of the detector for a particular scattering angle through simulations, provided that the interaction profile is well known. Thus, in order to study the effect of geometrical acceptance, we performed simulations for the recoil detector using an isotropic angular distribution for the generation of particles. Fig. 1.13 compares the correction factors that are obtained, using a uniform angular distribution, for the interaction profiles of $\mathrm{FWHM}_z = 7.4$ mm and 10.5 mm. It is reasonable to use these correction factors (respectively, corresponding to the circles and stars in Fig. 1.13) in order to correct the experimental data and to compare them with any theoretical predictions. This way, we can reliably correct the experimental data, taking into account the geometrical conditions and the energy cut-off. The results are shown in Fig. 1.14, where all the data sets are normalized to the theory at $-t = 0.0031$ $(\mathrm{GeV/c})^2$. It shows that the results corresponding to an interaction profile of $\mathrm{FWHM}_z = 10.5$ mm agree best with the theoretical prediction. This fact could be interpreted as an indication of an asymmetric target profile with respect to the $x$- and $z$-axes. In case of a symmetric target profile with respect to the $x$- and $z$-axes, we would have a conical extension of the gas-jet which would be essentially symmetric around the $y$-axis (direction of the gas-jet injection). It should be mentioned that, in the simulations of Fig. 1.13, $-t$ was calculated based on Eq. A.52, since the effect of those few protons which punch through at areas close to the edges of the first group of the Si-detector was found to be negligible (see Fig. 1.17, top panel).

The effect of profile asymmetry discussed above is shown by simulations to be approximately the same as the effect of either a slightly rotated Si-detector around the target point or a shifted interaction profile along the beam direction. It is quite possible that the exact position of the Si-detector with respect to the nominal target point has not been calculated very accurately in the experiment. Even if the position of the Si-detector during the experiment had been calculated with a good accuracy

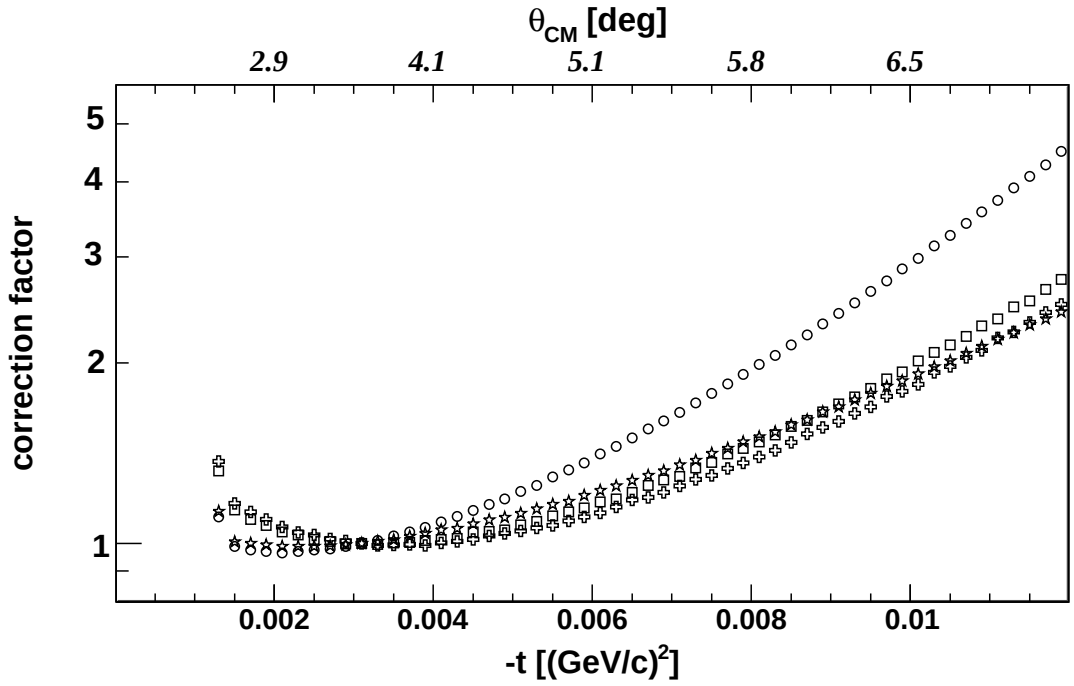


**Figure 1.13:** Required correction factors for unfolding the acceptance of the first group of the Si-detector from the cross section, as obtained from simulations, using the uniform distribution. In the simulations we used the kinematics of proton-$^{136}$Xe elastic scattering. Circles and stars show the simulation results with FWHM$_z$ =7.4 mm and 10.5 mm, respectively, as the extension of the interaction profile. Squares and pluses are obtained with an interaction profile of FWHM$_z$ =7.4 mm, respectively, when the Si-detector is rotated 0.5° around the $y$-axis toward the $z$-axis and when the Si-detector is only shifted (no rotation around the $y$-axis) by 1.5 mm toward $-\infty$ in the $z$-direction. Since in the simulations for the registered counts by the first group of the Si-detector all points are normalized to a constant (uniform distribution) at $-t = 0.0031$ (GeV/c)$^2$, the correction factor is equal to 1 at this value of $-t$.

with respect to the center of the interaction chamber, the center of the interaction region could have been easily off-centered by a few millimeters from the nominal position. The effect of an interaction point shifted by 1.5 mm toward $-\infty$ in the $z$-direction is comparable, up to a few percent, to the case when we have a rotated the Si-detector by about 0.5° toward the $z$-axis (Fig. 1.13). Simulation results for the elastic scattering cross section, using an interaction profile of FWHM$_z$ = 7.4 mm and a rotated geometry of 0.5° (or a shifted geometry of 1.5 mm) would reasonably agree with the shape of the experimental curve in Fig. 1.12. This can be inferred, since the correction factors, in Fig. 1.13, corresponding to the rotated (or shifted) geometry are well comparable to the correction factors of an interaction profile of FWHM$_z$ = 10.5 mm, which were already shown to agree reasonably with data. This means that the interaction profile could still be the same as the one measured

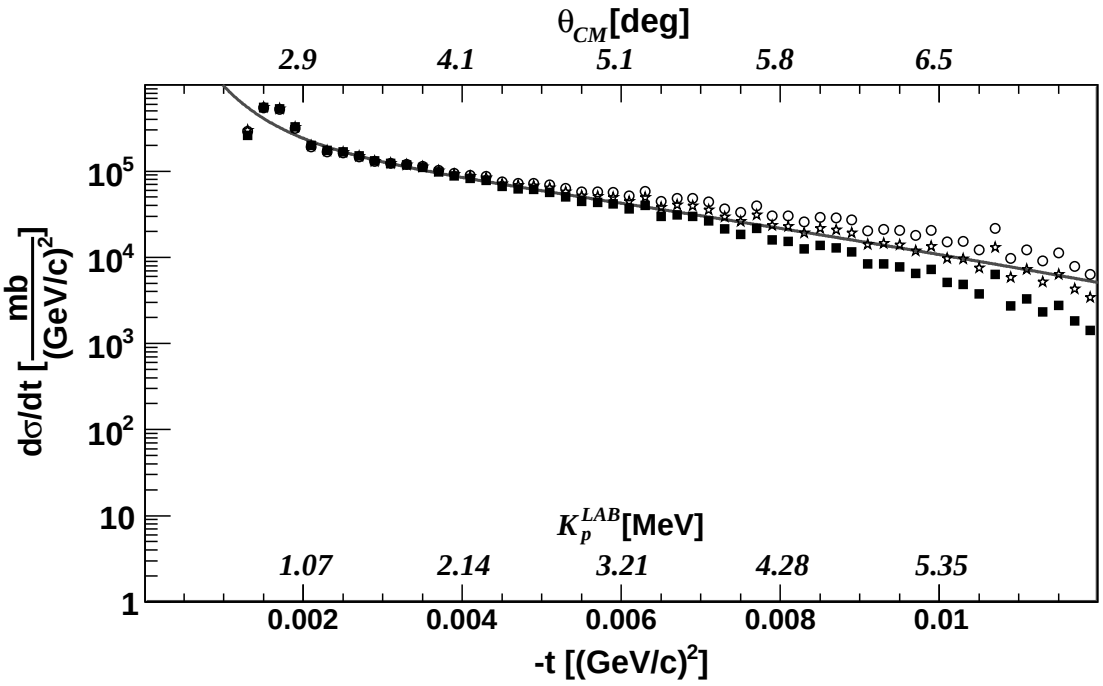


**Figure 1.14:** The curve and solid squares are the same as in Fig. 1.12. The hollow circles and stars represent the corrected experimental data for the interaction profiles of $\mathrm{FWHM}_z = 7.4$ mm and 10.5 mm, respectively. All data points are normalized to the curve at $-t = 0.0031$ $(\mathrm{GeV/c})^2$.

by the luminosity monitors. However, we cannot rule out the possibility of having extraordinarily extended target profile in the $z$-direction as the measurement of the luminosity was done through scanning the target with the beam in the $x$-direction. We could not disentangle the exact geometrical condition that we might have had during the experiment (a slightly rotated geometry with respect to the target point or a slightly shifted interaction profile with respect to the center of the interaction chamber or an asymmetric profile). Nevertheless, based on simulations, the net result of the three scenarios would be the same as far as the elastic scattering cross section is concerned.

One can imagine other scenarios for the shape of the interaction profile than simply a Gaussian; especially when seeking an explanation for the abrupt drop in the cross section at $-t$ values higher than $-t \approx 0.011$ $(\mathrm{GeV/c})^2$ (Fig. 1.11), other than the malfunctioning of the detector. It could be that we had a non-uniform (and/or discontinuous) luminosity resulting from the non-uniformity of the target density over the area of interaction with the beam. In subsection 1.4.2, we will try to understand the unusual behavior of the data points at higher $-t$ values merely based on the interaction profile analysis.

## Discussion

Fig. 1.15 (top panel) compares the elastic scattering cross-section calculations for an interaction profile of $\mathrm{FWHM}_z = 7.4$ mm for both cases of a uniform distribution and Glauber theory predictions as the angular density generators for the cross section. Clearly the difference between the two data points (related to the uniform and Glauber distributions) at each $-t$ reflects the deviation of the cross section from uniformity. Similarly, the amount of change in the difference between the two data points at $-t$ and $-t + \delta(-t)$ is directly related to the slope of the line connecting the two neighboring corrected points at $-t$. It is the slope of the fit to the corrected data points which would determine the local slope of the derived theory at a certain $-t$. Following the trend of the circles in this figure, we can intuitively conclude that, over the region of smaller CM scattering angles, the acceptance of the detector falls with $-t$ (or equivalently with the energy of the scattered protons) faster than exponentially. Over the larger values of the CM scattering angle (away from 90° in LAB), the acceptance falls rather exponentially.

It is necessary to investigate the amount of contamination of punch-through events in the results of the top panel in Fig. 1.15. This is because we established our arguments on the geometrical acceptance of the first group of silicon detector based on the assumption of having negligible amount of punch-through events. For the interaction profiles of $\mathrm{FWHM}_z = 7.4$ and 10.5 mm (with $\mathrm{FWHM}_x = 9.0$ mm and $\mathrm{FWHM}_y = 5$ mm) the simulations show that majority of the generated protons stop in the first group of the Si-detector of 1 mm thickness (Fig. 1.15, bottom panel). The shaded region in this figure is due to those few protons which punch through at areas close to the edges of the first group of the Si-detector.

There is a possibility that we had an effective thickness of less than 1 mm for the silicon detector. In such a case protons might punch through the silicon detector, thereby changing the shape of the calculated elastic scattering cross section (based on Eq. A.52). In order to have an estimate of this change, we can take an exaggerated case considering a thickness of 0.5 mm (half of the nominal thickness) for the silicon detector. Fig. 1.16 shows the results using a uniform distribution for the cross section and interaction profiles of $\mathrm{FWHM}_z = 7.4$ and 10.5 mm (with $\mathrm{FWHM}_x = 9.0$ mm and $\mathrm{FWHM}_y = 5$ mm). Up to $-t = 0.0085$ $(\mathrm{GeV/c})^2$ the simulated cross sections decrease smoothly; however, at higher values of $-t$, there are significant deviations from this smooth trend of the cross section. It has to do with those protons punching through the nickel foil and 0.5 mm thick silicon detector at high enough energies. Simulations show that, for the detector geometry in our setup, those protons that are generated at around $z = -5$ mm down to $-\infty$ can punch through the first group of the Si-detector. Based on this fact, we can compensate for the punch-through protons and extract the cross section. By incorporating the proper FWHM for the interaction profile into our simulations as well as normalizing the simulations to the statistics of our experiment, we can obtain $-t$ which is now different from the one extracted through Eq. A.52 due to the punch through; this is particularly important

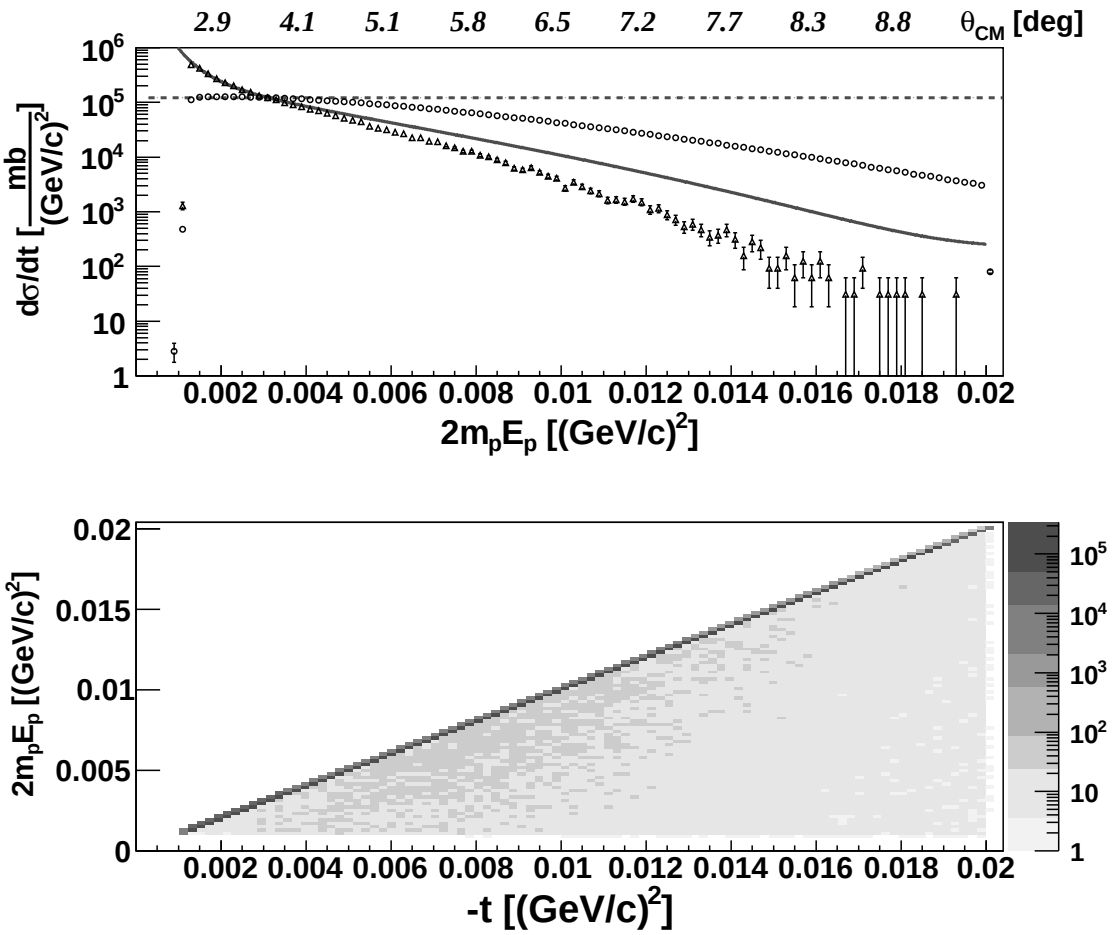


**Figure 1.15:** Top: proton-$^{136}$Xe elastic scattering cross section as a function of four-momentum-transfer squared, calculated based on Eq. A.52 (assuming no punch through). The curve is the Glauber theory prediction and the dotted line represents the uniform distribution. Circles and triangles show the simulation results with FWHM$_z$ = 7.4 mm as the extension of the interaction profile using the uniform distribution and Glauber theory, respectively. $E_p$ is the deposited energy in the first group of the Si-detector and all points are normalized to the curve at $-t = 0.0031$ (GeV/c)$^2$. Bottom: simulations of the 1 mm thick Si-detector, showing four-momentum-transfer squared on the $y$-axis, calculated based on the deposited energy in the Si-detector with the assumption of no punch through, versus the one calculated from angular relations (Eq. A.49) on the $x$-axis. Here, the interaction profile of FWHM$_z$ = 10.5 mm and a uniform cross section is used in the simulations in order to magnify the influence of the probable punch-through events. The same pattern is expected when using a FWHM$_z$ = 7.4 mm.

when we want to compensate for the punch-through protons in the experimental data. Therefore, by doing simulations with Glauber theory used as the generator for the cross section, we can repeat the same procedure as in the case of uniform

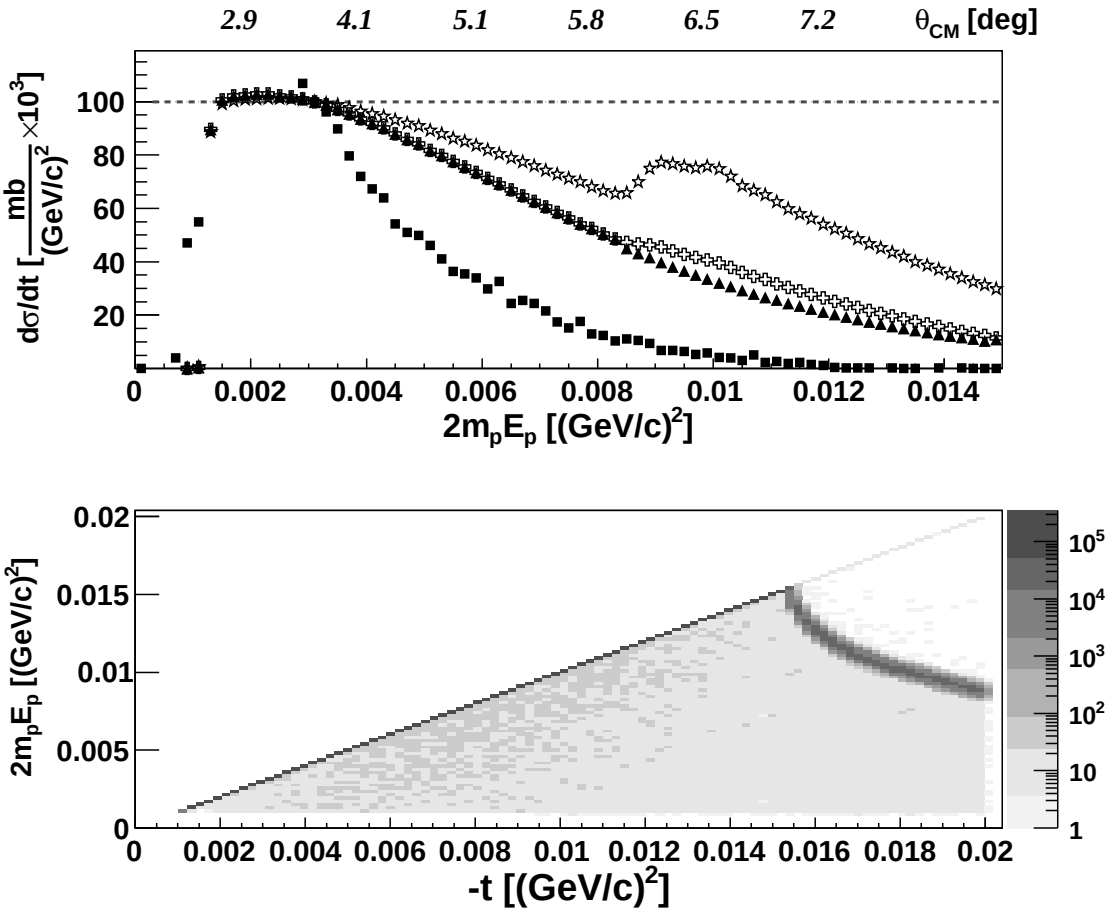


**Figure 1.16:** Top: proton-$^{136}$Xe elastic scattering cross section as a function of four–momentum-transfer squared, calculated based on Eq. A.52. The solid squares show the experimental data. The other three symbols represent the simulations for a Si-detector of 0.5 mm thickness with a uniform phase space density generator (the dotted line); stars: simulations with an interaction profile of FWHM$_z$ = 10.5 mm, pluses: simulations with an interaction profile of FWHM$_z$ = 7.4 mm, and triangles: simulations with an interaction profile of FWHM$_z$ = 7.4 mm compensated for the punch-through protons. All experimental and simulated data points are normalized to the line at $-t = 0.0031$ (GeV/c)$^2$. Bottom: simulations of the recoil detector, with 0.5 mm thickness for the Si-detector, showing four-momentum-transfer squared, calculated based on Eq. A.52, versus the one calculated from angular relation (Eq. A.49). The interaction profile of FWHM$_z$ = 7.4 mm (corresponding to the plus signs in the top panel) is used in the simulations.

distribution to see how much we need to compensate for the punch-through events in our experimental data. Fig. 1.17 shows the result of these simulations with an interaction profile of FWHM$_z$ = 7.4 mm. It confirms that the punch-through protons have negligible contribution in changing the shape of the elastic scattering

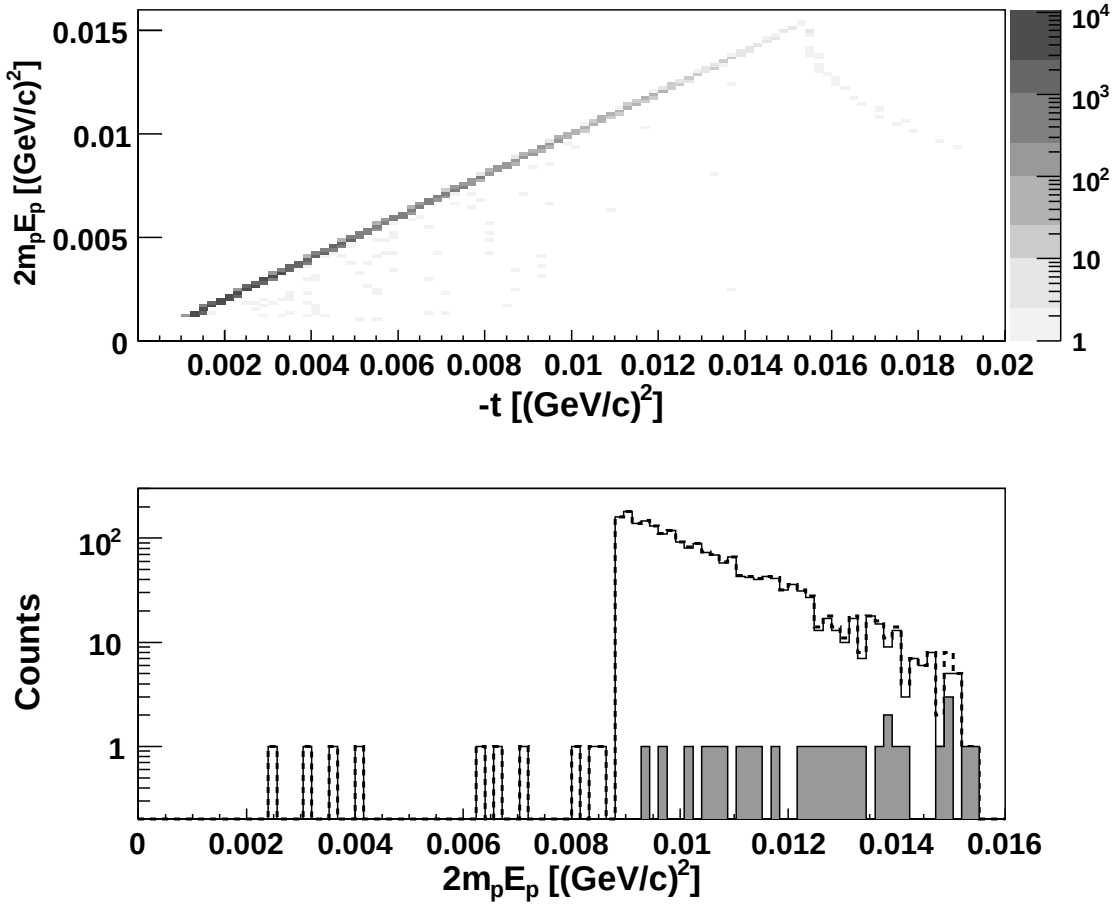


**Figure 1.17:** Top: same as Fig. 1.16 (bottom panel), using the Glauber theory as the generator for the elastic scattering cross section. Bottom: elastic scattering cross section obtained using Eq. A.52 (dotted line; projection of the top histogram on the $y$-axis), contribution of the punch-through protons to the elastic scattering cross section (shaded area), and elastic scattering cross section compensated for the punch-through protons (solid line), all shown within the range of the detected four-momentum-transfer squared over which the protons could punch through.

cross section, calculated based on Eq. A.52. Even a 0.5 mm thick Si-detector can effectively stop the protons (knowing the fact that the underlying cross section is, like the Glauber theory curve, a sharply decreasing function with respect to $-t$) so that we expect no significant change in the extracted shape of the cross section. Therefore, the probable minute deviations in the effective thickness of the Si-detector from 1 mm should not be a potential source of concern (see Fig. 1.17) in making use of Eq. A.52 to calculate the elastic scattering cross section. Therefore, unlike Fig. 1.16 (for the case of a uniform cross section and 0.5 mm thick Si-detector), it is not necessary to compensate for the punch-through events at all.

The compensation for the probable punch-through events in the experimental data would first require normalizing simulations to data. In this sense one has to be careful regarding the procedure of normalization; we can perform the simulations with the same amount of statistics as we had in the experiment or we can normalize to one point. Clearly, either of the two methods would lead to (even slightly) different compensation factors and that means slightly different contributions of the punch-through protons (shaded region in Fig. 1.17).

### 1.4.2 Effect of various interaction-profile shapes on the acceptance (target profile asymmetry)

Assuming that the drop in the elastic scattering cross section happens at $-t \approx 0.011$ (GeV/c)$^2$ (Fig. 1.11), one can obtain the corresponding value of the proton scattering angle $\theta$, from Eq. A.47, to be 85.32°. In the following procedure this $\theta$ value represents the angle at which the proton is generated and ended up at the upper edge of the first group of the Si-detector; the generation point of the proton (say on the $z$-axis) is essentially where the target density (and equivalently the interaction profile) undergoes a discontinuity. The idea is to see whether or not we can translate back the abrupt drop in the cross section to a possible discontinuity in the pressure profile (target density). Based on the position of the first group of the Si-detector, this density discontinuity must have started at $z = -2.52$ mm, assuming the center of interaction to be at $z = 0$. Therefore, we simply assume that (possibly) a pressure drop in the target must have occurred over the region of $z < -2.52$ mm. For simplicity, I proceed with assuming a discontinuity only along the $z$-axis, since we know that the discontinuity in the density along the $x$- or $y$-axis should have very small effect on the outcome of the simulations for the cross section. This small effect on the shape of the cross section is even more negligible than the principal effect of the extension of the target profile along the $x$- and $y$-axes. This is, of course, because of the far less impact of the derivative of the interaction profile along the latter two axes on the overall cross section, when we already see a quite small impact from the sheer extension of the interaction profile along these axes. Now I consider for the continuous part of the generation region to be a Gaussian along the $z$-axis, with the centroid at $z = 0$ and $\text{FWHM}_z = 7.4$ mm, bounded in the interval $z \in [-2.52\text{ mm}, +\infty]$. But, for the region of $z \in [-\infty, -2.52\text{ mm}]$, we can think of different possibilities for the generator functional form such as: uniform, damping sinusoidal or even diffraction-like patterns. Doing simulations we can study the influence of these scenarios for the shape of the interaction profile, even though it seems hard to seek physical and experimental explanations backing any of these functional forms. For $-t = 0.02$ (GeV/c)$^2$, we would find $z = -14.46$ mm as the lowest point (along the $z$-axis) from which a proton can be generated and ended up at the first group of strips right at the edge of the detector located at $\theta = 89.5°$. This way, we make sure that the contribution to the cross section in the interval $0.011 < \frac{-t}{(\text{GeV/c})^2} < 0.02$ is solely made by the generation points in the interval

$z \in [-14.46\text{ mm}, -2.52\text{ mm}]$. Practically, here, $z = -14.46$ mm is equivalent to $-\infty$. In order to reproduce the shape of the cross-section data, shown in Fig. 1.11, which resembles a step-like behavior at $-t \approx 0.011$ (GeV/c)$^2$, three functional forms were used as follows:

1) A diffraction-like pattern as sketched in Fig. 1.18.

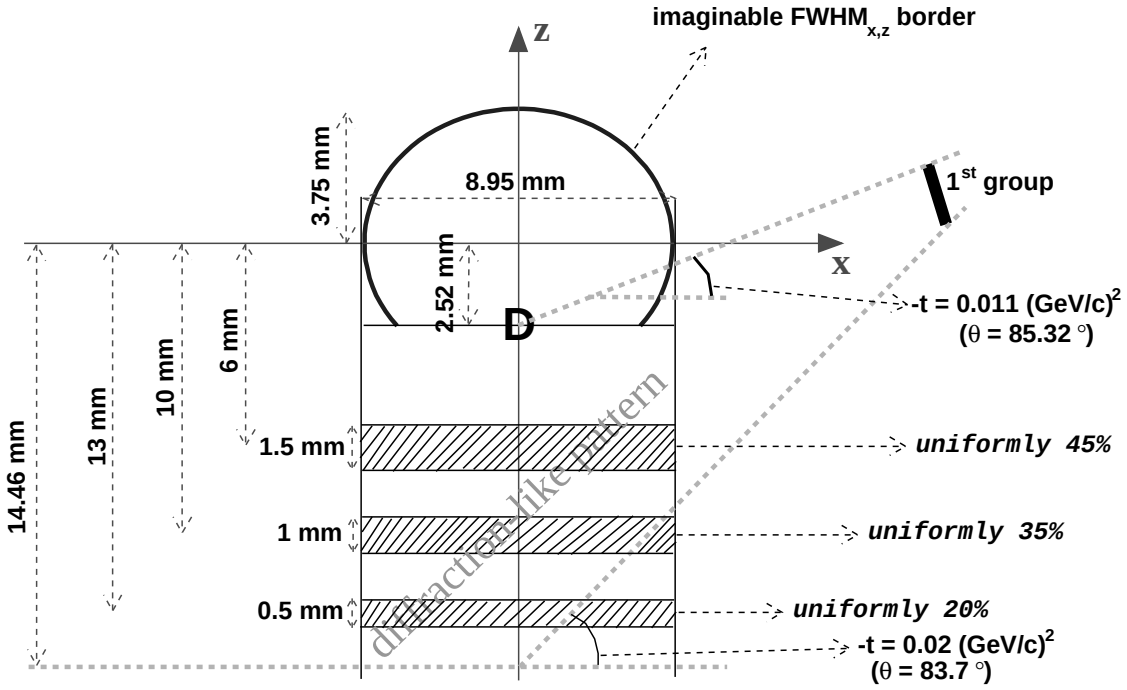


**Figure 1.18:** An exaggerated sketch (in terms of the scales) of a diffraction-like pattern, which was assumed as the area over which the proton generation was performed for the discontinuous generation region extended from the point labeled as D down to $-\infty$ along the beam direction. The continuous Gaussian generator extends along the beam direction from D up to $+\infty$. The $x$- and $y$-components of the generation points are continuously distributed; $y$: uniformly, $x$: uniformly before and Gaussian after D along the beam direction.

2) A damping sinusoidal of the form $\frac{\sin^2(z)}{z^2}$ for generation density defined over $z \in [-\infty, -2.52\text{ mm}]$. The generation along the $x$- and $y$-axes was performed as continuous Gaussians of FWHM = 9 and 5 mm, respectively, all over the $z$-axis (beam direction).

3) A uniform function defined over $z \in [-\infty, z_0]$, followed by a gap defined over $z \in [z_0, -2.52\text{ mm}]$. For an optional value of $z_0 = -10$ mm, the result (Fig. 1.19, bottom left panel) shows a very small enhancement around $-t = 0.013$ (GeV/c)$^2$.

Fig. 1.19 (top left panel) shows the specific functional forms that were chosen for

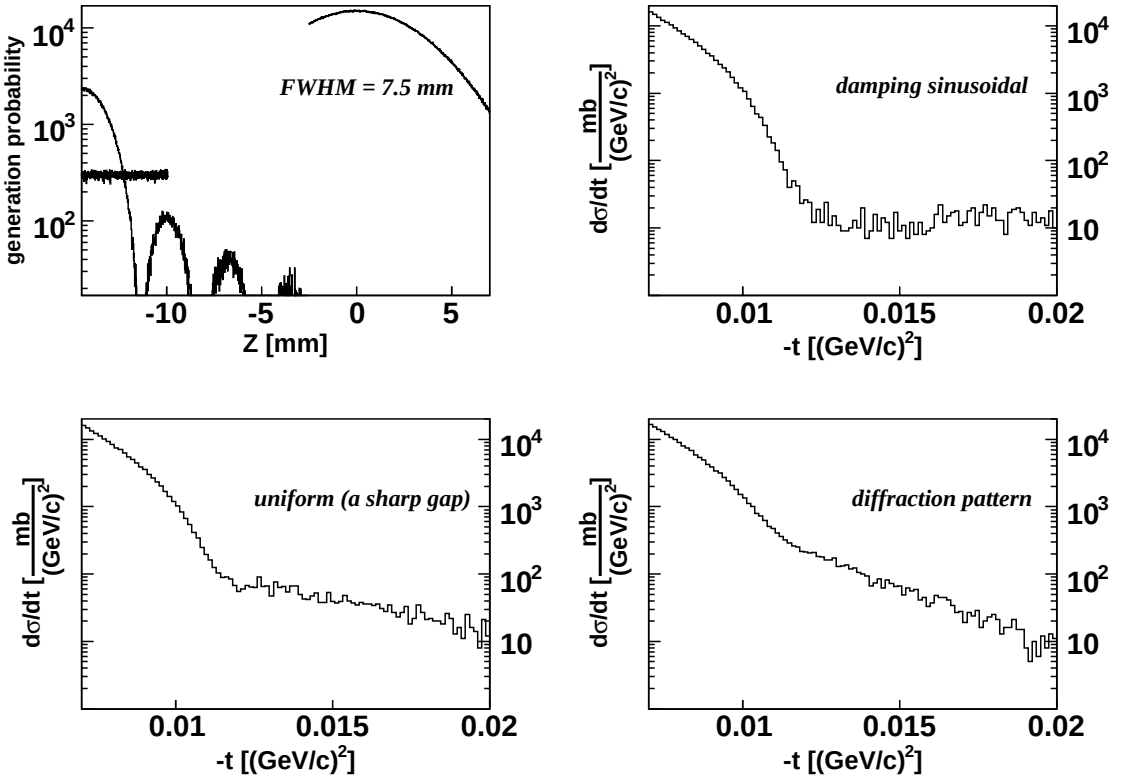


**Figure 1.19:** Top left: functional forms (uniform and damping sinusoidal) for discontinuous generation region together with a Gaussian for the continuous generation region used as the interaction profile for particle generation along the beam direction ($z$-axis). The corresponding elastic scattering cross sections at high values of $-t$ can be compared with the cross section calculated based on the diffraction-like pattern (Fig. 1.18).

the step-like uniform and damping sinusoidal generators together with the resulting cross sections. In all the three procedures 97% of the events were dedicated to the continuous Gaussians, while 3% to the discontinuous regions. In fact, there is only a slight difference between the results of the second and third functional forms; in the case of a 'damping sinusoidal' the range of $z \in [-12\text{ mm}, -2.52\text{ mm}]$ acts effectively as a gap (see Fig. 1.19, top left panel), which is a longer gap than what I used in the 'uniform generation' approach, and that is the reason of having no enhancement around $-t = 0.013\ (\text{GeV/c})^2$. On the other hand, the high probability of generation around $z = -14$ mm, in the case of a damping sinusoidal, causes a small enhancement at very high values of $-t$ (as compared to the case of 'uniform generation'). The latter two arguments could well explain the kind of fluctuations in the resulting cross section of the 'damping sinusoidal' as opposed to the one obtained for the 'step-like uniform generation'. For a generator of diffractive form, the cross section shape (Fig. 1.19, bottom right panel) at higher values of $-t$ does not seem to

be compatible with the experiment at all, since it has a smoothly decreasing trend rather than a uniform one (the assumption of the step-like behavior of data at high values of $-t$). This favors especially the idea of a 'gap' since, in terms of the target density distribution in the discontinuous region, the density of gas (in case of gap or damping sinusoidal) goes in the opposite direction, as compared to the assumed diffraction-like pattern, as we Go to a large negative distance along the $z$-axis. For the discontinuous region in Fig. 1.18, I optionally chose spatially uniform generation over three regions. Thus, for instance, I have only dedicated 0.6% of total events to the farthest generation region. The choice of the shape of this diffraction-like pattern should not matter, as long as we are solely interested qualitatively in studying the change in the cross section trend; based on the above discussion, the whole idea of a 'diffraction-like' interaction profile is out of question (see Fig. 1.19, bottom right panel), independent of the specific form of the assumed diffractive pattern.

Apart from the different resulting shapes for the cross section in the region of large $-t$ values (Fig. 1.19), what they show in common is the smoothness in their continuous spectra. Clearly, this cannot explain the broken trend of the cross section at $-t \approx 0.011$ $(\mathrm{GeV/c})^2$ (Fig. 1.11). In other words, we may conclude that whatever shape the interaction profile possesses (continuous or discontinuous), it cannot explain the sudden drop in the experimental cross section. This is a valid point, since we deal with an extended interaction profile in which the contribution from different regions of the interaction profile to the cross section pattern is appreciable in smoothening any abrupt behavior originating from a discontinuous region of the interaction profile.

### 1.4.3 Acceptance correction by using the measured angular distribution

As already mentioned, one needs to correct for (i.e. unfold) the geometrical acceptance of the detector setup in order to obtain the correct elastic scattering cross section that can be properly compared with theoretical calculations. By performing simulations, using a specific angular probability distribution (say theory 1) one can simply use the same theory curve in order to correct back the simulated points. Obviously, the corrected simulated points would, by definition, be exactly back on the curve of theory 1. In principle, one can correct the cross-section data using the correction factors obtained from simulations. However, one cannot compare these corrected data with the same theory prediction in order to draw any conclusion on the agreement between the theory and the experiment. In order to be able to make such a conclusion we need to have another source to be used for our generator other than the theory under investigation. In subsection 1.4.1, we calculated, trigonometrically, the percentage of particles that are generated at a certain $-t$ and missed the first group of the Si-detector (back-tracking the generated protons). This percentage was directly related to the geometrical acceptance of the detector at $-t$ and subsequently provided the correction factor. In the following discussion we will

try to reconstruct the underlying theory by using the measured position in the Si-detector and following a procedure that I will refer to as "trigonometric approach" in calculating $-t$. This will allow us to investigate the possibility of safely extracting the elastic scattering cross section, while making use of the position information of the Si-detector.

Fig. 1.20 shows the measured position in the Si-detector for the first group of strips close to 90° in LAB. Keeping in mind that we had a threshold of about

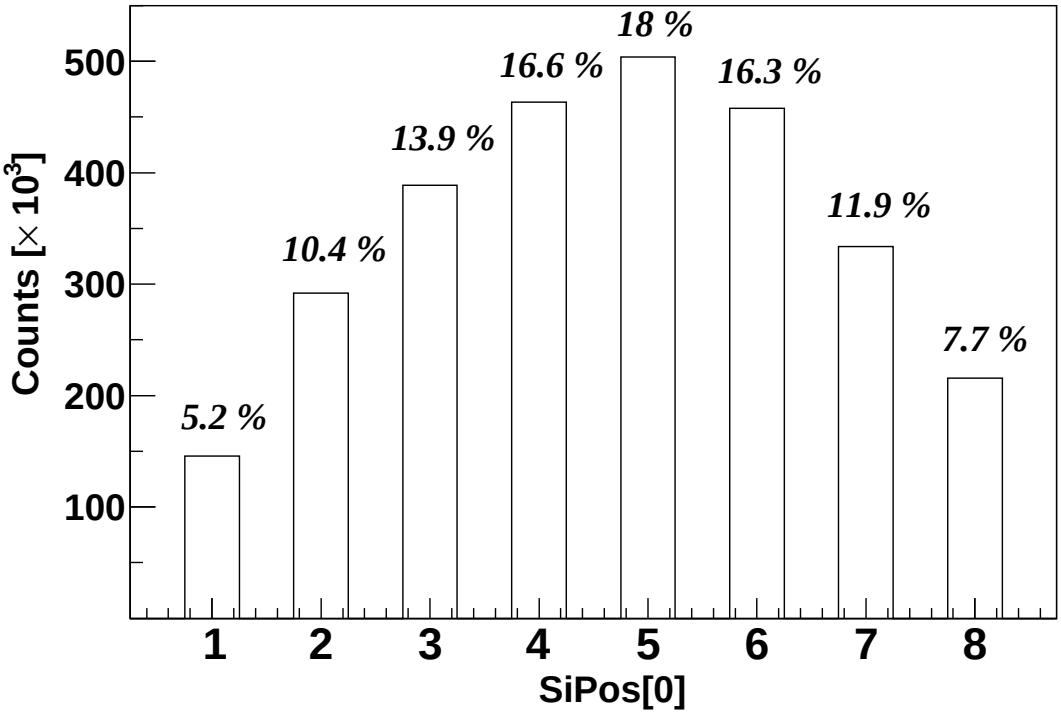


**Figure 1.20:** Position information, as obtained during the measurement, of the detected events by all the eight strips of the first group of the Si-detector. The first peak is originating from the strip which is close to 90°. The percentages on the figure reflect the relative heights of the peaks and sum up to 100%. The Si-detector had a threshold of about 500 keV.

500 keV, one can understand the observed trend of data in this figure. Except for the last three strips, we can see an increase in the number of events registered at each position (strip), while getting away from the closest strip to 90° in LAB (the midpoints of the first and eighth strips of the first group of the silicon strips are placed at 89.3° and 86.5°, respectively). In principle, we would expect a decreasing behavior, since the elastic scattering cross section as well as the detector acceptance decrease with increasing $-t$ or equivalently with decreasing $\theta$. The fact that we see an opposite behavior in this figure (for the first few strips) has to do with the

threshold condition which is discussed below.

First, consider the situation where every strip receives equal number of elastically scattered events. Analytic calculations (trigonometric approach) show that for a target profile of $\mathrm{FWHM}_z = 7.4$ mm, the energy threshold is directly related to the relative heights of the position peaks. Considering a Gaussian interaction profile with 9 mm, 5 mm, and 7.4 mm as the extension of the FWHM along the $x$-, $y$-, and $z$-axes and allowing the generated events at a specific random point to end up uniformly over the area of every strip, we can obtain the corresponding distribution of $-t$ for each strip. We expect identical peak heights for all the strips when we have no threshold, since we are assuming identical number of events ending up at every strip and triggering the detector. On the other hand, when we have a non-zero threshold every strip detects a different percentage of events ending up in them. The resulting spectrum for the triggered events by the strips would show no more peaks of identical heights. Loosely speaking, the peaks would have relative heights as 0.34, 0.5, 0.55, 0.64, 0.74, 0.85, 0.89, and 0.92 as compared to 1 (when we have no threshold). These numbers are simply the ratio of events with $-t \geq 0.0011$ $(\mathrm{GeV/c})^2$ (for a threshold of 500 keV) to the total number of events for each strip. Fig. 1.21 shows $-t$ as it is seen by each strip as well as the cumulative $-t$ seen by the first group of eight strips. For the first few strips, this resembles the rising trend of the peaks' heights in Fig. 1.20. However, what we see in Fig. 1.20 is a combination of the discussed threshold effect as well as the effect of non-uniformity of the elastic scattering cross section. This non-uniformity can be quantified and integrated in the above approach for distributing events; it can be thought of as dedicating different number of events to each strip. Therefore, if we could somehow obtain the relative number of events (based on the real elastic scattering cross section) to be dedicated to each strip, then we would expect a resulting spectrum with relative heights identical to what we see in Fig. 1.20. In principle, we can attribute the effect of the relative (appropriate) number of events to the relative heights of the position peaks by doing the simulations. This should give the exact relative heights of the peaks provided that we implement the exact experimental conditions in the simulations (such as the spatial extension of the interaction profile and the precise position of the Si-detector). In addition to the exact experimental conditions to be implemented in the simulations, we need to know the underlying cross section based on which to generate particles. We can try to make sense of Fig. 1.20, based on the approximate geometrical information (such as an interaction-profile extension of $\mathrm{FWHM}_z = 7.4$ mm, $\mathrm{FWHM}_y = 5$ mm, and $\mathrm{FWHM}_x = 9.0$ mm) and by considering a shear elastic scattering cross section based on the Glauber theory (or the derived cross section in subsection 1.4.1). Fig. 1.22 shows the position information of the detected events by all the eight strips of the first group of the Si-detector, as obtained through simulations with the mentioned assumptions. Comparing the relative heights of the peaks in this figure (bottom panel) with the trend of the percentage of events that can satisfy the threshold condition for each strip in Fig. 1.21, we can qualitatively conclude that the increasing behavior of the peak heights in

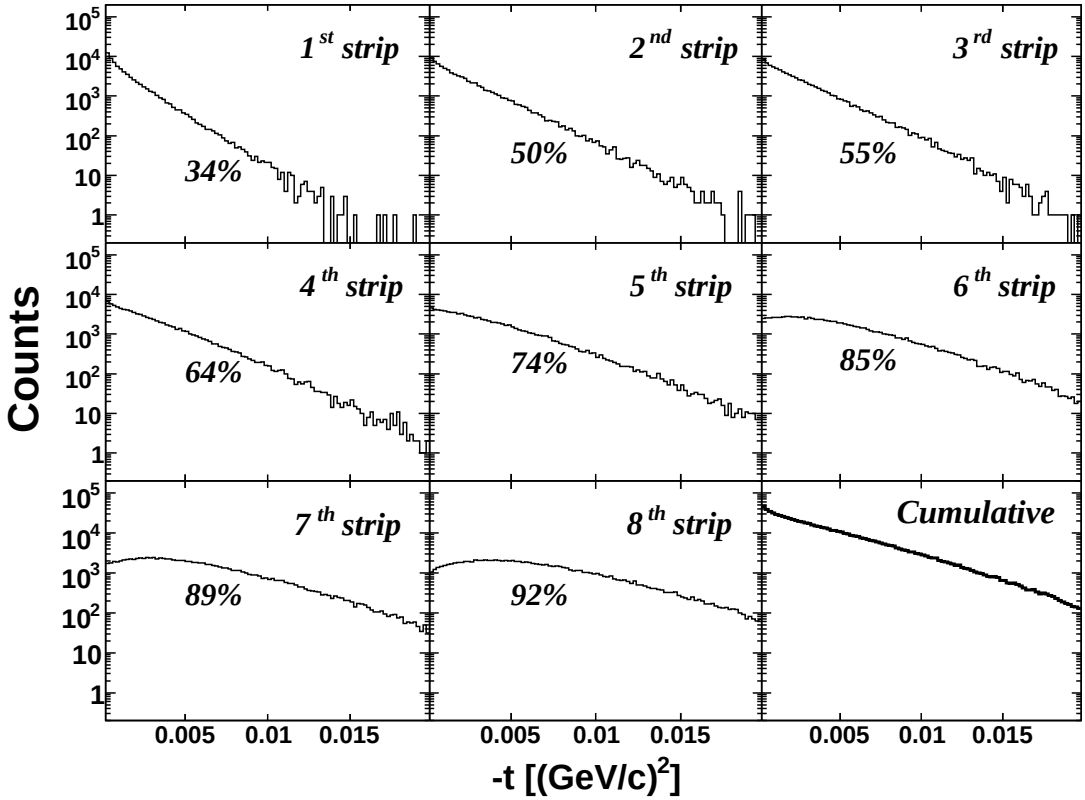


**Figure 1.21:** Analytic (trigonometric) calculation of $-t$ for the elastic scattering, based on Eq. A.49, as seen by each strip of the first group of Si-detector. A Gaussian of 9.0 mm, 5 mm, and 7.4 mm as FWHM along the $x$, $y$, and $z$-axes is considered for the spatial generation of protons and all the events (dedicated to a specific strip) are required to end up at a random point on the strip surface. No threshold is considered here and identical number of events are distributed over each strip. The percentage of events that, for each strip, can satisfy a threshold condition of 500 keV is written under the corresponding curve. The detected $-t$ by the first group is, in principle, the summation of all eight spectra of the individual strips (spectrum on the bottom right hand side).

Fig. 1.22 for the first five peaks is due to the threshold condition. On the other hand, it is the decreasing elastic scattering cross section which counteracts and takes over the threshold action at higher $-t$ values and appears as gradually decreasing heights for the other three strips. Comparing Fig. 1.22 (bottom panel) with Fig. 1.20 we may assume that the relative heights of the position peaks (or at least the rising and falling trend of the peaks' heights) in Fig. 1.20 could mainly be attributed to the elastically scattered protons. Based on this assumption, we may confidently extract the appropriate number of events for each strip from Fig. 1.20 and feed it in our random-generation model to obtain the cumulative elastic scattering cross section.

Fig. 1.23 (dotted curves) shows the same as in Fig. 1.21 with the addition of the

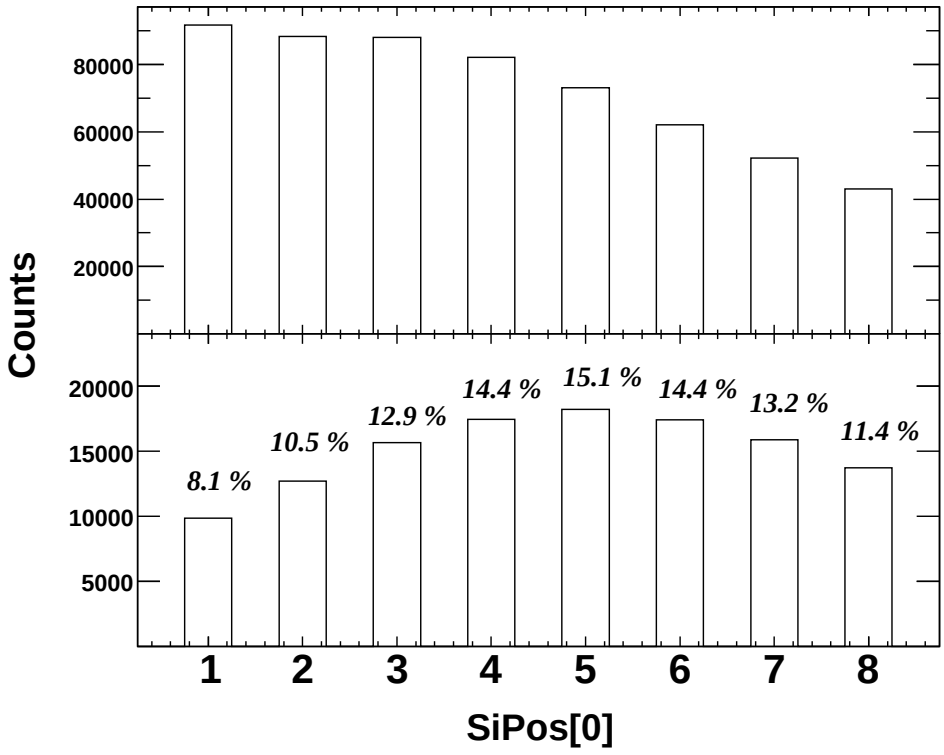


**Figure 1.22:** Same as Fig. 1.20, but obtained through simulations, using the Glauber theory, with threshold energies of zero (top panel) and 500 keV (bottom panel). The percentages on the bottom panel could be compared with the corresponding ones on Fig. 1.20.

threshold as well as using an appropriate number of events for each strip as extracted directly from the experimental result of Fig. 1.20. We can also use strip position information to derive the contribution of individual strips to the elastic scattering cross section obtained through the analysis of the deposited energy. For comparison the corresponding results are also presented in Fig. 1.23 (thin histograms).

If we would have a zero threshold for the Si-detector in the experiment, the dotted curve in the panel that is labeled as "cumulative" (Fig. 1.23) could be regarded as the underlying theory curve. This is true to the extent that we can trust the geometrical assumptions that we made in our analytic calculation and provided that all the detected events by the strips in Fig. 1.20 can be considered as elastic scattering events. In other words, since in this cumulative cross section the acceptance of the detector has already been automatically unfolded, it has to be the same as the underlying cross section. It is because we were assigning a specific number of events (total number of thrown events) to each strip instead of throwing events in the full phase space and then tracing them to see if they end up at the detector or not.

What we see in Fig. 1.20, however, includes the real detector condition of having

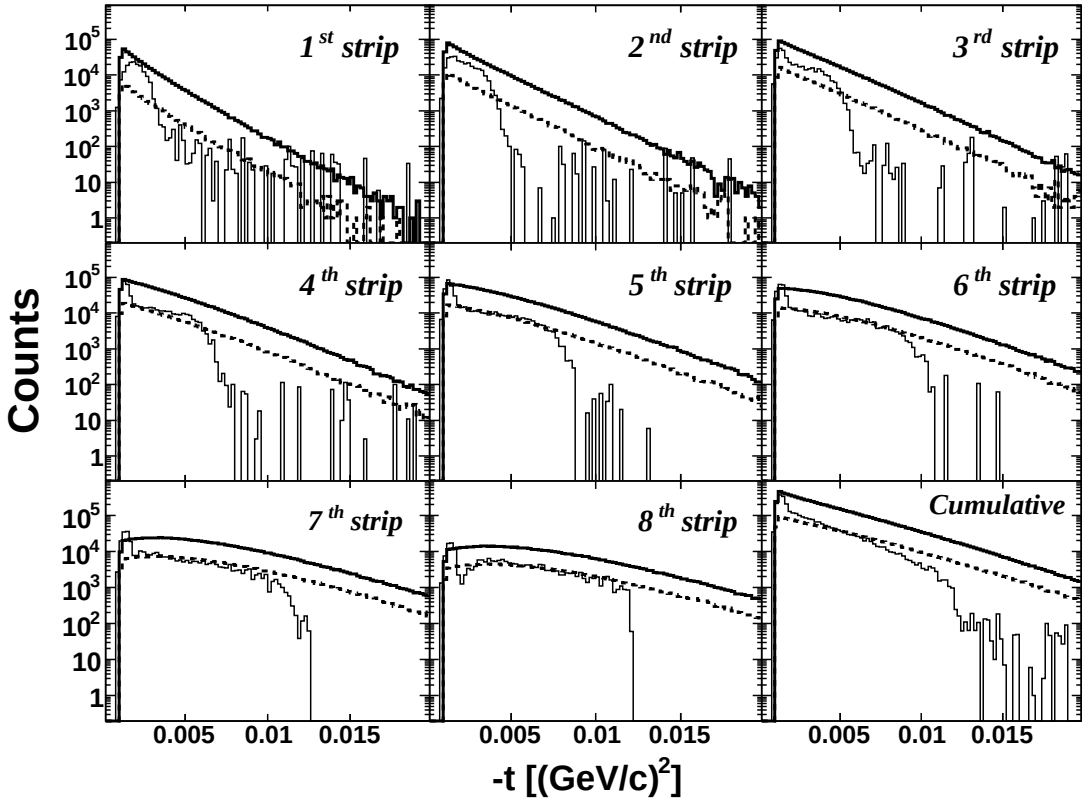


**Figure 1.23:** Thick dotted and solid curves (trigonometric approach): same as Fig. 1.21 but with a threshold of 500 keV for the Si-detector and generating appropriate number of events towards each strip as extracted from Figs. 1.20 (dotted curves) and 1.24 (solid curves). Thin curves (energy deposition approach): Elastic scattering cross section obtained, alternatively, through the experimental analysis of deposited energy in each strip.

a non-zero energy threshold. Although with the explained cumulative method we could unfold the geometry acceptance, detector threshold still remains folded so that we cannot simply feed the raw spectrum of Fig. 1.20 into our generator in order to extract the underlying theory. It could readily be understood if we notice that the underlying theory should be independent of the threshold energy of the Si-detector. In fact, if we could have a zero threshold detector, then we could directly exploit the spectrum of Fig. 1.20 to extract the underlying theory (like what we did to obtain the dotted curve in Fig. 1.23). In the following we will try to unfold, to some extent, the influence of the threshold in shaping the spectrum of Fig. 1.20 by making use of simulations. Considering the simulation results in Fig. 1.22, we can use the ratio of the heights of the peaks of the upper panel to the corresponding ones of the lower panel and use them to enhance (modify) the heights of the peaks in Fig. 1.20. Since this ratio only represents the amount of threshold influence we assume that it should be irrelevant to the theory curve that we used (Glauber) as

our generator. Therefore, we can directly use these ratios to appropriately modify the heights of the peaks of Fig. 1.20. In principle, we would expect the resulting spectrum to show a pattern similar to what we see in the simulations of Fig. 1.22 (top panel). Fig. 1.24 shows the enhanced (modified) spectrum of Fig. 1.20 through exploiting the simulations of Fig. 1.22 with the assumed threshold of 500 keV (solid bars) as well as assuming an optional threshold of 900 keV (dotted bars). In none

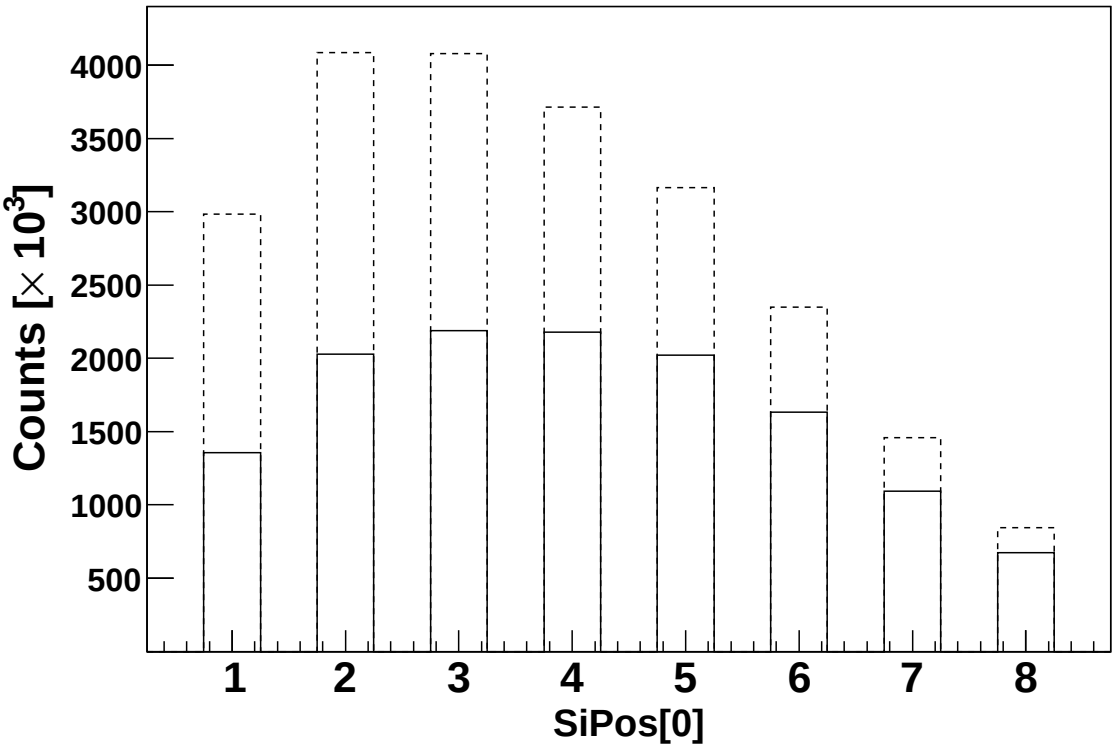


**Figure 1.24:** Modified spectrum of Fig. 1.20, exploiting simulations of Fig. 1.22 with the nominal threshold of 500 keV (solid bars) as well as assuming a threshold of 900 keV (dotted bars). Simulations show that, regardless of the threshold value, the relative counts of at least the first strip (with respect to the others) violates the trend that one should expect from the elastic scattering cross section. This could be an indication that this strip must have been (partly) outside the phase space coverage of the elastically-scattered protons.

of these two results we see a decreasing trend for the heights of the bars as one should expect from the elastic scattering cross section (like in Fig. 1.22, top panel). Different threshold values were used in the simulations in order to investigate the effect of threshold on the relative heights of the modified spectrum. Nonetheless, all of them show smaller heights of the peaks at least for the first strip(s) relative to the next neighboring strip(s). This could be an indication that the detector placement

must have been different; for instance, the spectrum corresponding to 900 keV in Fig. 1.24 can be explained if we consider a geometry of the Si-detector in which the first strip of the first group is placed (at least partly) at an angle more than 90° in LAB. In principle, what we expect from the unfolded spectrum in Fig. 1.24 should resemble the underlying cross section. That means if all the strips were placed at angles less than 90° in LAB, then we would see an ever decreasing pattern in the heights of the peaks (remember that at this stage, the threshold effect is unfolded and we can imagine all the strips with zero threshold capable of detecting all the events corresponding to each of the peaks in Fig. 1.24). Thus, the lower number of counts of the first peak relative to that of the second peak could only mean that this strip must have been located (at least partly) at an angle larger than 90° in LAB so that the phase space of the elastic scattering channel cannot cover the strip. In fact, a rotated geometry of the Si-detector in Fig. 1.7 as much as 1° around the $y$-axis toward the $x$-axis can place the first strip at a slightly larger angle than 90° in LAB. Fig. 1.23 shows as well the cumulative cross section (thick curves), obtained like the dotted curves when feeding the statistics of 500 keV threshold of Fig. 1.24 (instead of Fig. 1.20) into the generator. Fig. 1.25 shows the cumulative cross section, obtained through the trigonometric approach, together with the Glauber theory prediction for the elastic scattering cross section, all normalized to the theory curve.

There is an inherent drawback in this method of calculating $-t$ from the angular placements of individual strips. It arises from the sizable extension of the interaction profile with respect to the widths of the detector strips. The fact that a number of random positions for the generated particles are chosen over a sizable region (interaction profile) and then attributed with equal weights to a specific strip, considerably flattens the fine structure of any underlying cross section. This can easily be seen in Fig. 1.25, especially in the flat structureless region below $-t = 0.003$ $(\mathrm{GeV/c})^2$. As an example we can take two generation points, over the interaction profile, one at $z = z_0$ and the other at $z = -z_0$ which are located symmetrically with respect to the origin. Clearly, the generation probability for the two positions is the same, but that the two generated particles at these points both end up at a specific strip with the same probability is not true. In our analytic approach of calculating $-t$, it is not possible to implement this difference in the probability of ending up at a specific strip for a particle generated at $z_0$ or $-z_0$. Therefore, the bigger the extension of the target profile the less precise would be the calculation of $-t$, when using the trigonometric approach. Thus, one has to be careful in following this approach to calculate $-t$, even when there is a high confidence in the spectrum of Fig. 1.20. For extended target profiles, along the beam direction, this method is the most inaccurate when the detector is installed near 90° in LAB. Hence, there is no way of precisely calculating the elastic scattering cross section (detector installation at 90°), based on this approach, other than minimizing the target extension along the beam direction. Similarly, for other reaction channels, one cannot expect that installing detectors at angles close to zero in LAB could overcome this inherent problem of target extension, because then the calculation of $-t$ gets sensitive to the

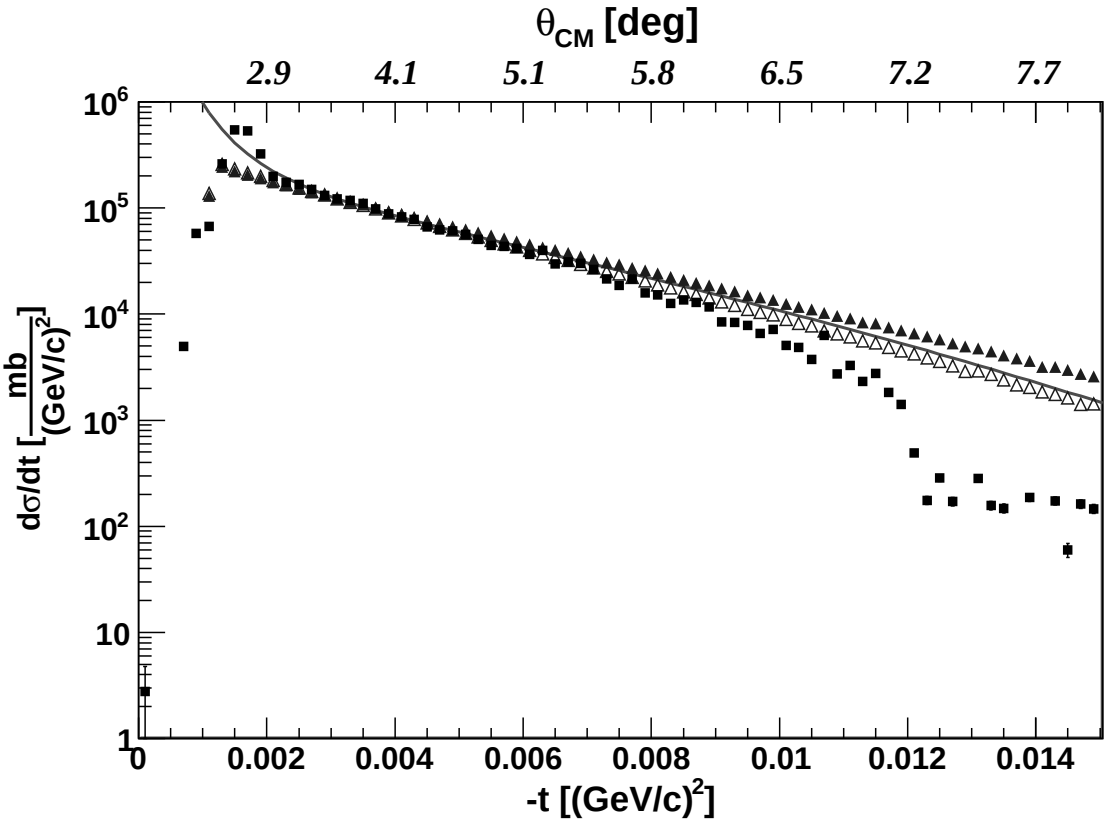


**Figure 1.25:** Elastic proton-$^{136}$Xe scattering cross section as a function of four-momentum-transfer squared. The solid squares are the experimental data (corresponding to the thin histogram in the bottom right panel of Fig. 1.23), as obtained through Eq. A.52 assuming no punch through, and the curve is the Glauber theory prediction. Solid triangles: cumulative $-t$, as in Fig. 1.23 (solid thick curve). The hollow triangles are for when we exclude the events registered in the last two strips of the first group of the Si-detector, using the same approach that led us to obtain cumulative $-t$ in Fig. 1.23. All points are normalized to the curve at $-t = 0.0031$ (GeV/c)$^2$.

target extension along the $x$- and $y$-axes.

There is a possibility that the malfunctioning of the Si-detector (appeared as a drop in the cross section pattern of Fig. 1.11) is due to the operation of the last two or three strips of the first group. In such a case, the registered energy of the events by these defected strips cannot be used to calculate $-t$ from Eq. A.52 and might instead contribute to cross section at lower values of $-t$ than what we expect from an elastic scattering event. This in turn can cause the shape of the elastic scattering cross section, obtained from data analysis, to deviate from the simulations for FWHM = 7.4 mm at the values of $-t$ lower than where the drop happens (Fig. 1.11). In this case, we are not able to exclude these miscalculated events. However, that does not necessarily mean that the relative peak heights of

the last few strips are wrong. If we assume that all of the eight strips of the first group of the Si-detector were triggering correctly (based on the threshold energy), Fig. 1.20 would show a correct pattern of triggering while at the same time the last few strips did not register the correct deposited energy spectrum. Thus, it is possible that this figure could still be used to extract the elastic scattering cross section as the underlying cross section. It is interesting to note that the behavior of (at least) the first strip in Fig. 1.24 undermines the applicability of this method in calculating the cross section over the whole range of $-t$.

Fig. 1.25 compares the results of the analytic calculation of the cumulative $-t$ for the two cases of excluding or including the influence of the last two strips. As can be seen in this figure, apart from the overall shapes of the two calculated cross sections, the inclusion of the statistics of all the strips causes the slope of the cross section to deviate from the theory prediction; even if the pattern in Fig. 1.20 (and consequently in Fig. 1.24) can be considered as a true triggering pattern, there still could be a significant amount of inelastic scattering events in the last two (few) strips which can satisfy the threshold condition. The qualitative similarity of Figs. 1.20 and 1.22 cannot, quantitatively, rule out the significance of inelastic scattering events that were detected by the first group of the Si-detector. Hence, it would not be reasonable to take all the statistics under the peaks (especially the last few peaks) of Fig. 1.20 as having originated from elastic scattering events.

### 1.4.4 Inelastic scattering channel(s)

Using the spectra of the deposited energy in the Si-detector groups (see Fig. 1.7), one can also try to identify inelastic scattering events. In general, these spectra comprise elastic and inelastic scattering events. One can build up the whole spectrum of the deposited energy (in a Si-detector group) by performing simulations for elastic as well as inelastic scattering. It is necessary to know what the dominant inelastic scattering channels are if we want to understand the shape of the experimental spectrum. The procedure would be to use the theoretical estimation for the dominant channels in the Monte Carlo simulations getting protons with appropriate energies and angles in phase space.

The calculation of the inelastic scattering channels in $^{136}$Xe, that leads to the Giant Dipole Resonance (GDR) with an excitation energy of 15 MeV has been performed, using the Eikonal approximation [14]. Fig. 1.26 shows the theoretical calculations for the proton-$^{136}$Xe elastic and inelastic scattering cross sections, based on the Glauber multiple scattering theory and the above-mentioned calculations for the Giant Dipole Resonance in $^{136}$Xe. Fig. 1.27 shows the experimental as well as the simulations results for the deposited energy in all the Si-detector groups. In the spectrum of the deposited energy for the fifth group of the Si-detector we expect the lowest contribution from the elastic scattering events (compared to the other groups of the Si-detector). Whereas, based on the simulations results for this group, we see the highest contribution from the inelastic scattering events, as compared

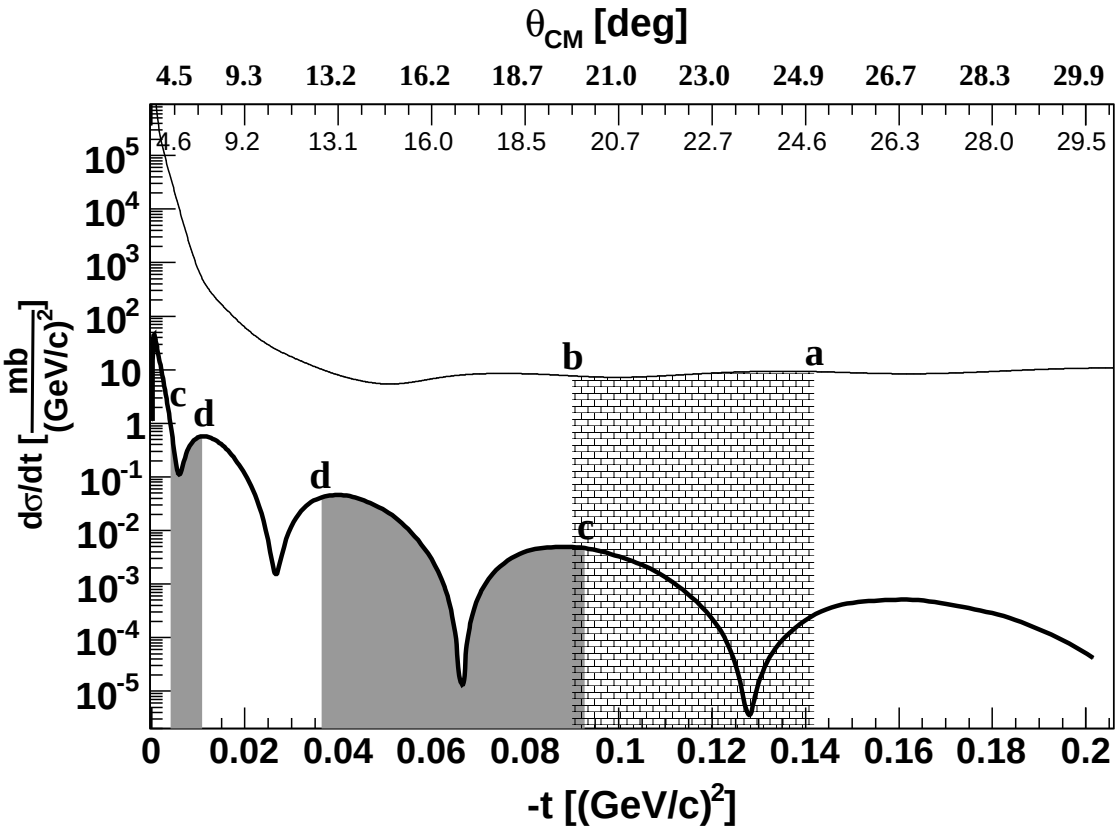


**Figure 1.26:** Theoretical calculations for the cross section of proton-$^{136}$Xe elastic scattering channel (thin curve), based on the Glauber theory, and inelastic scattering channel of giant dipole resonance of $^{136}$Xe with $E_x = 15$ MeV, based on a calculation using the Eikonal method (thick curve [14]). The numbers on the top horizontal axis represent the proton scattering angle in the center-of-mass frame with respect to $-\hat{z}$; the upper row of numbers is related to the inelastic scattering kinematics of proton-$^{136}$Xe with $E_x = 15$ MeV, whereas the lower one is related to the elastic scattering kinematics. The brick- and simple-shaded areas in the picture show, respectively, the covered region of the fifth group of the Si-detector by the elastic and inelastic scattering kinematics for a point-like target. The boundary edges of the two shaded areas correspond to the LAB scattering angles of $a = c = 73.4°$ and $b = d = 76.6°$.

to the amount of inelastic scattering events registered in the other groups for the case of GDR in $^{136}$Xe with $E_x = 15$ MeV. For the simulations in Fig. 1.27, we only considered the elastic and inelastic scattering channels and assigned equal number of events to the two channels to be generated according to their respective kinematics and cross section. In order to have a thorough investigation on the contribution of various reaction channels to the observed spectra, one needs to take into account all the potential reaction channels. Apart from the elastic and inelastic scattering channels one can think of possible transfer reactions as well, *e.g.* $(p, d)$ and $(p, t)$.

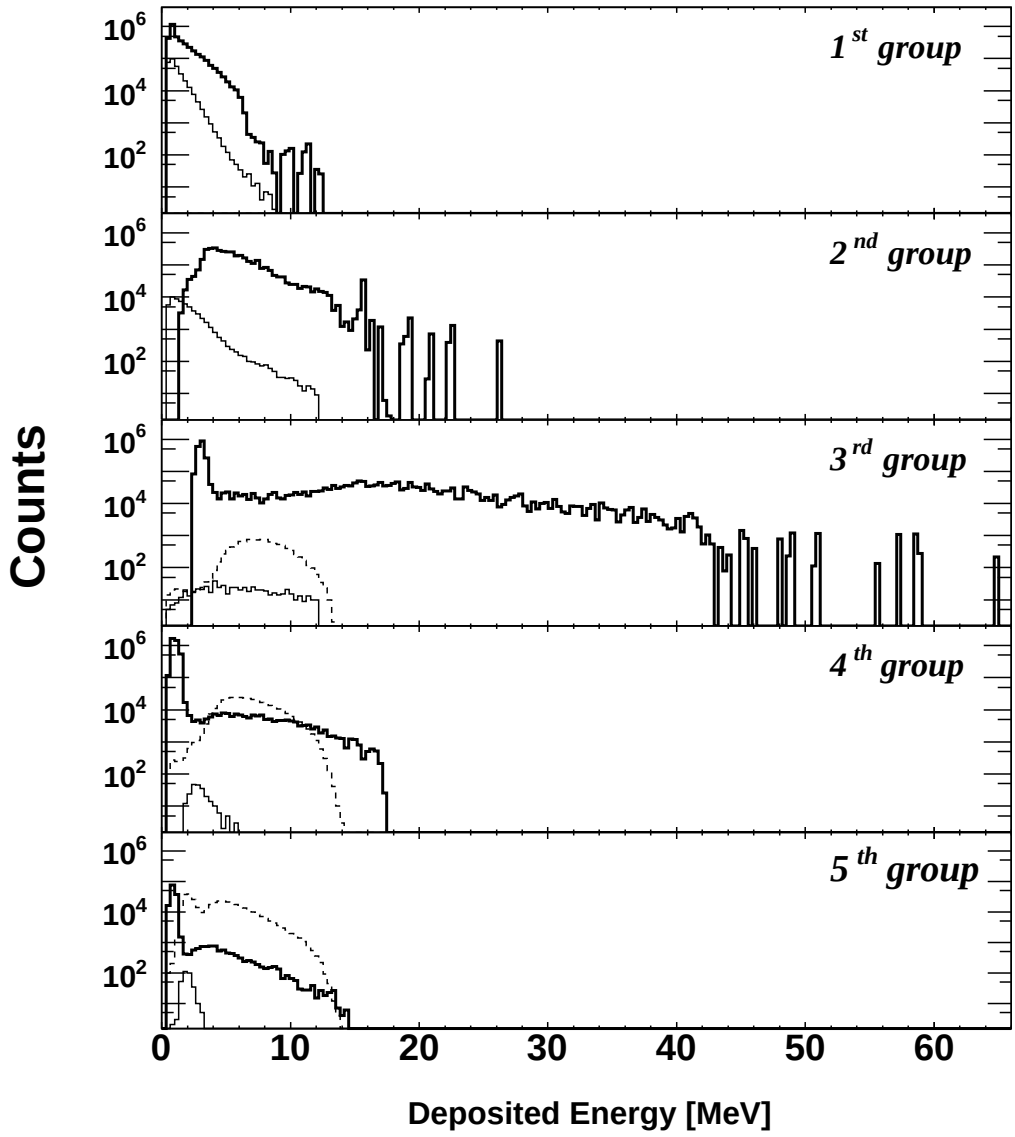


**Figure 1.27:** Deposited energy in the five groups of the Si-detector as measured in the experiment (thick histograms) and obtained through simulations. In the simulations for the elastic (thin histograms) and inelastic (dotted histograms) scattering channels an extended interaction profile of $\mathrm{FWHM}_z = 7.4$ mm is assumed and equal number of events were thrown into the phase space for both channels. In the simulations for the inelastic channel of $^{136}$Xe, a giant dipole resonance with $\mathrm{E}_x = 15$ MeV is considered. The unusual extension of the experimental spectrum of the third group of the Si-detector has to do with the operation of this group.

However, based on the kinematical calculations for these two channels, one would expect no Si-detector exposure from these transfer channels (Fig. 2.3, bottom panel,

shows the respective kinematics).

The inelastic scattering channels may be identified by analyzing the data originating from those groups of the Si-detector which are positioned farther from 90° in LAB (see Fig. 1.7). This is especially fruitful in distinguishing the elastic and inelastic scattering channels, since we expect a narrower distribution in the deposited energy for elastically-scattered protons as we move away from the first group. This is because for smaller laboratory scattering angles, almost all protons punch through the detector and deposit almost the same amount of energy in the detector. This narrower pattern of the deposited energy is clear in the spectrum of elastic scattering of the fifth group as compared to the fourth group, and the fourth group as compared to the third group in Fig. 1.27. If we would not have protons punching through these layers then we would expect a completely different behavior in terms of the extension of the elastic scattering spectrum in these groups. In this case, it is the kinematical curve of Fig. 1.28, rather than the straggling, that influences the amount of extension of the elastic scattering spectrum. Whereas, when we have

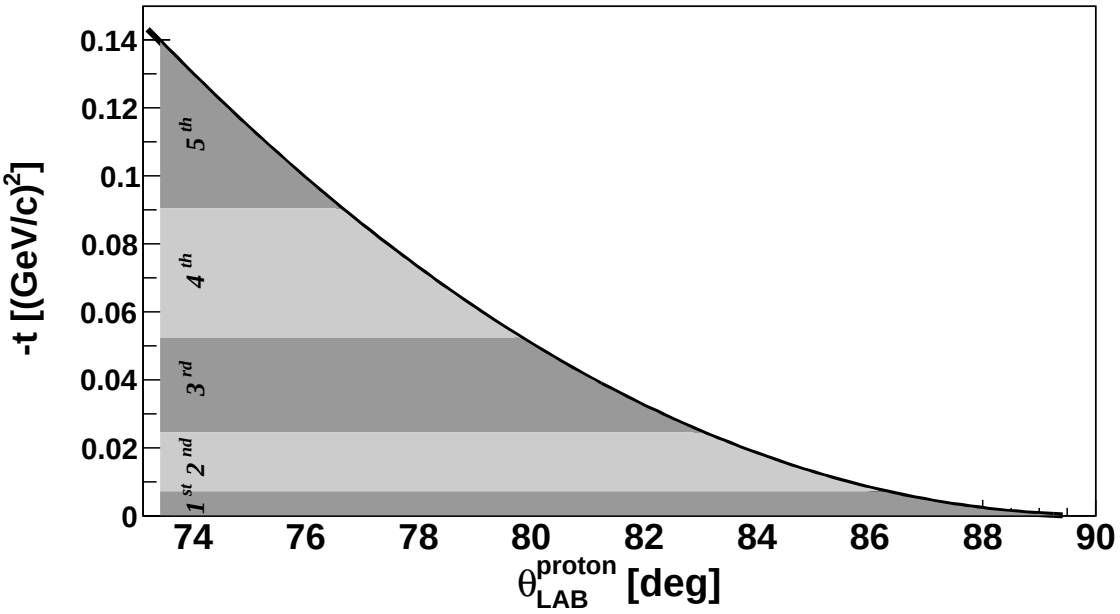


**Figure 1.28:** Four-momentum-transfer squared versus the scattering angle in LAB for the proton-$^{136}$Xe elastic scattering. The scattering is in inverse kinematics with a beam energy of 350 MeV/nucleon. The shaded regions show the coverage of the four-momentum-transfer squared by the five groups of the Si-detector in the case of a point-like scatterer.

punch-through protons, it is the kinematics of Fig. 1.28 as well as the energy of the protons that compete in determining the amount of extension of the spectra of the deposited energy. For instance, based on kinematics, this extension is broader for the fifth group as compared to the fourth group. But since the elastically-scattered protons can punch through both groups, we expect to have lower deposition of en-

ergy (and hence slightly narrower spectrum) in the fifth group. On the other hand, for the first group of the Si-detector, we would expect the extension of $-t$ (or, equivalently, deposited energy) to be the same as what we see in Fig. 1.28 (for a point-like scatterer). It is because we do not expect punch-through events for this group.

Fig. 1.29 compares the amount of GDR inelastic scattering events registered by the fourth and fifth groups of the Si-detector (rotated by 0.5° around the $y$-axis) for an interaction profile of $\mathrm{FWHM}_z = 7.4$ mm. For comparison, the contribution of the non-punch-through events in the fifth group is also presented in the top panel (dotted line). The reduction of the statistics, appearing at around 8 MeV for the punch-through events, is an indication of the inherent fluctuation in the cross section pattern. Based on the results of the second panel, protons start to punch through the fifth group at energies around 12 MeV. Accidently, around the same energy, the inverse kinematics of the two-body proton-$^{136}$Xe inelastic scattering (with 350 MeV/nucleon) requires the scattering angle to turn around (see the bottom panel of Fig. 1.29). This is due to the specific detector thickness in the present setup.

Once we have a thickness for the Si-detector that could stop protons with the kinetic energy corresponding to the turning point of the kinematical curve (point $T$ in Fig. 1.29), then the angular position of the detector could be important as far as the stopping power of the silicon layer is concerned. For instance, imagine that the thickness of the silicon layer is such that protons effectively punch through at kinetic energies higher than the one corresponding to point $P$ (Fig. 1.29). Hence, for the ideal case of having a point-like scatterer, it would be more desirable to install the detector in such a way that $\theta_{LAB}^{(P_2)} > \theta_{LAB}^{(P)}$. This way, we can effectively stop the inelastically-scattered protons. The bigger the extension of the target profile the less effective would be the stopping power of the detector. This is because the extension of the interaction profile exposes the detector to protons with smaller scattering angles in LAB than $\theta_{LAB}^{(P_2)}$; in such a case we may expect to have punch-through events. Therefore, in order for the inelastically-scattered protons generated at $z < 0$ (for an extended target) to be stopped by the fifth group of the Si-detector, one needs to install the detector in such a way that the upper edge of the detector is placed at an angle larger than $\theta_{LAB}^{(P)}$. This, in turn, could slightly limit the exposure area of the detector to inelastic scattering events (depending on the angular extension of the detector). Based on the above discussion, it would be desirable to have thicker detectors in order to stop all the inelastically-scattered protons that are detected by the fifth group. In short, when we are interested in stopping all the inelastically-scattered protons observed by the fifth group of the Si-detector, we could simply increase the detector thickness and move it towards smaller $\theta$-angles to make sure that we will have a thoroughly exposed detector surface. Clearly, as far as the stopping power for the inelastically-scattered protons is concerned, the fifth group of the Si-detector in our experiment was absolutely inefficient. This is because the thickness of the detector is small (1 mm) and $\theta_{LAB}^{(P)}$ is close to $\theta_{LAB}^{(T)}$ ($\approx 77.1°$). The angular positions of the two edges of the fifth group of the Si-detector are $\theta_{LAB}^{(P_2)} = 73.4°$ and $\theta_{LAB}^{(P_1)} = 76.6°$. It is worth mentioning that, based on the kinematics

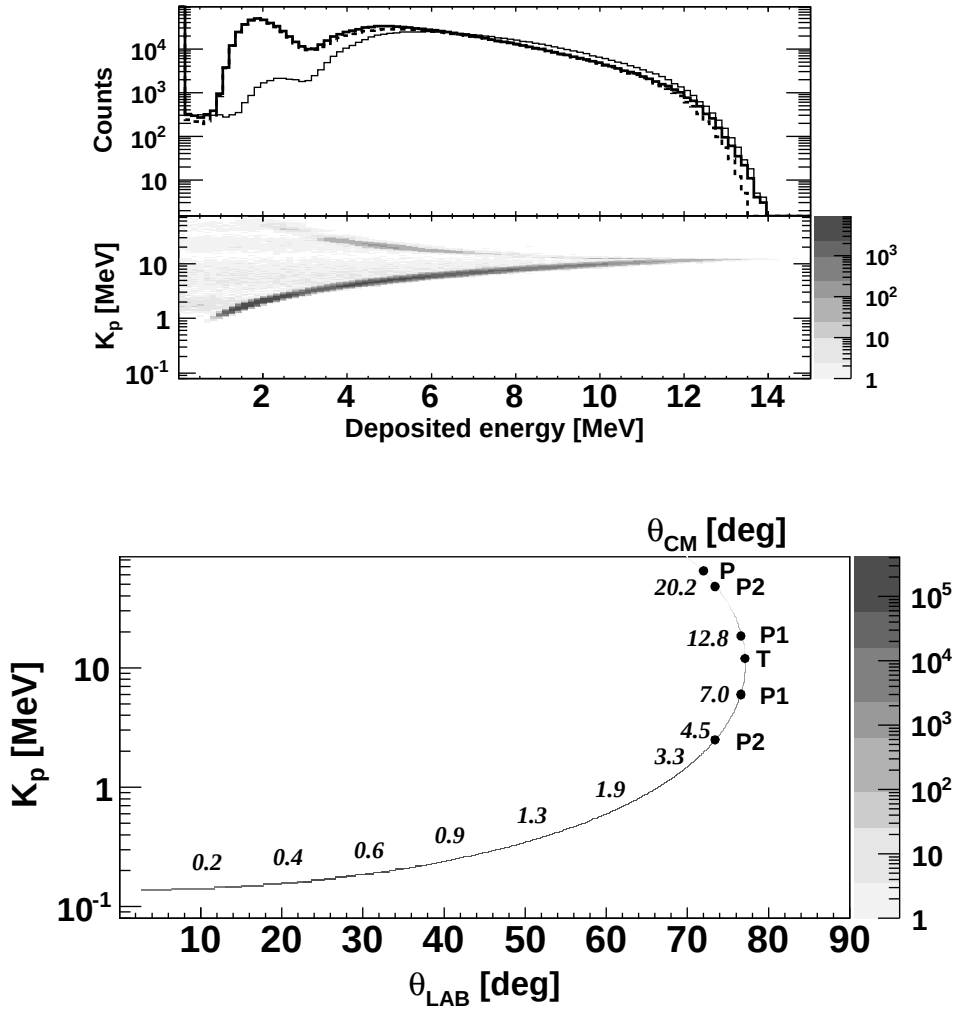


**Figure 1.29:** Top panel: simulation results for the deposited energy in the fifth (thick line) and fourth (thin line) groups of the Si-detector (Fig. 1.7) for the inelastically-scattered events corresponding to the GDR excitation of $^{136}$Xe with $E_x = 15$ MeV. The dotted line shows the deposited energy by the stopped protons in the fifth group of the Si-detector. Second panel: kinetic energy of proton versus the deposited energy in the fifth group of the Si-detector for the GDR events. In the simulations, an interaction profile of $FWHM_z = 7.4$ mm and a rotated geometry by 0.5° around the $y$-axis toward the $z$-axis is considered. Bottom panel: kinetic energy of proton after inelastic scattering versus the proton laboratory scattering angle, calculated using Eqs. A.9 and A.13. The numbers on the histogram show a few proton scattering angles (in degrees) in the center-of-mass frame corresponding to $\theta_{LAB} \approx 10°, 20°, 29°, 40°, 50°, 60°, 70°, 73.4°, 76.6°, 76.6°$, and 73.4°. $P_1$ and $P_2$ represent the location of the edges of the fifth group of the Si-detector on the kinematical curve with the assumption of a point-like target. T represents the turning point of the kinematical curve. See text for further details.

in the bottom panel of Fig. 1.29 and the specific position of the Si-detector groups in the experiment (Fig. 1.7), we would not expect a considerable amount of inelastic scattering events (related to the discussed channel) to be seen by the groups other than the fifth group, when we have a point-like scatterer. Therefore, the spectrum

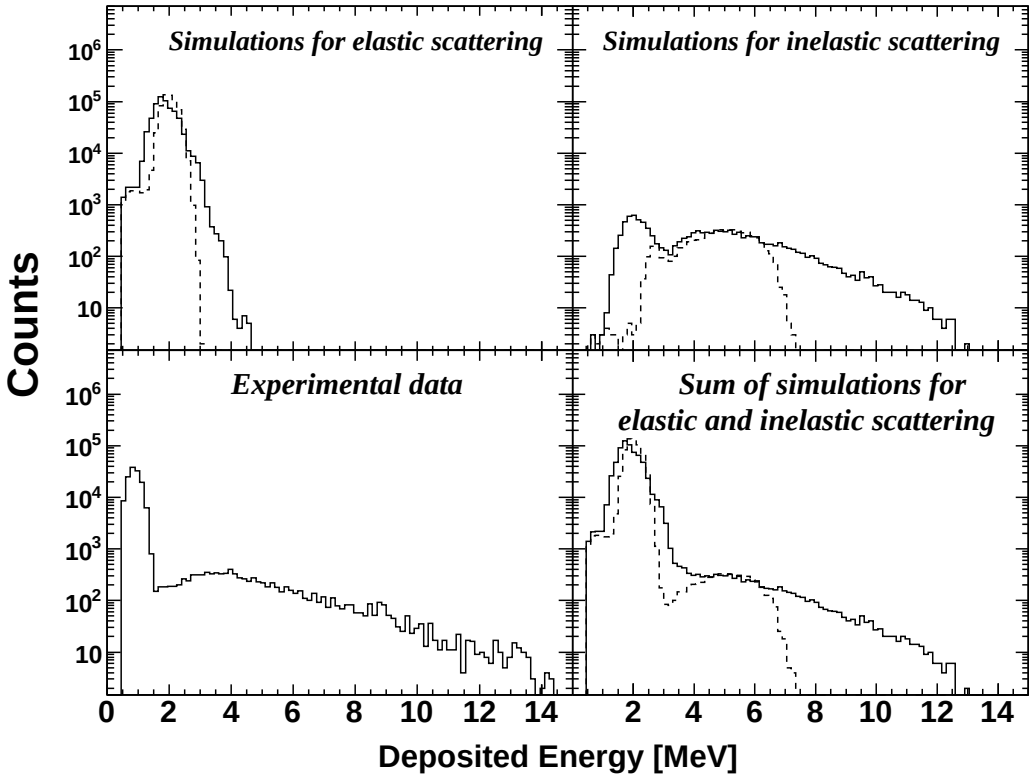


**Figure 1.30:** Simulations and experimental results for the deposited energy in the fifth group of the Si-detector. The simulations are for the elastic as well as the inelastic scattering events for the giant dipole resonance of $^{136}$Xe with $E_x = 15$ MeV. The dotted curves show the simulations for the point-like target, while the solid curves are for an interaction profile with the spatial extension of $FWHM_z = 7.4$ mm, when the Si-detector is rotated 0.5° around the $y$-axis toward the $z$-axis. The spectrum in the bottom right panel is the sum of the two spectra in the top panels.

that we see in the top panel of Fig. 1.29 for deposited energy in the fourth group is mostly constructed by those protons that are generated at spatial points along the $z$-direction lower than the center of the interaction profile ($\theta^{(fourth\ group)}_{upper\ edge} \approx \theta^{(T)}_{LAB}$). This, in turn, is the reason that we have a drastic loss in the registered inelastic scattering events in the third group (see Fig. 1.27).

Fig. 1.30 shows the experimental data for the response of the fifth group of the Si-detector together with the simulation results of the elastic and inelastic (GDR) scattering channels for a point-like target as well as an extended interaction profile.

In the simulations, the ratio of the elastic scattering to inelastic scattering events is taken to be in agreement with the amount of reaction rates observed by the Si-detector for the two reaction channels. Clearly, the extended tail in the experimental data is a sign of the extended target profile, as can be compared to the simulation results. In the simulations of the elastic scattering channel, there is a step-like behavior right after the cut-off of the threshold region. It is due to those protons which punch through the fifth group of the Si-detector at regions close to the edges of this group. Comparing the experimental data with the simulations for $\mathrm{FWHM}_z = 7.4$ mm (for a rotated Si-detector by 0.5° around the $y$-axis toward the $z$-axis), two major differences can be observed: the position of the elastic scattering peak and the existence of a dip right after the elastic scattering peak in the experimental data which is missing in the simulations.

Assuming that we have a correct calibration for the experimental spectrum, one can think of other scenarios in order to reproduce these two characteristics of the experimental spectrum through simulations, namely the position of the elastic scattering peak and the existence of a dip following this peak. Fig. 1.31 shows the same results as in Fig. 1.30 (solid histograms), assuming a significantly smaller thickness of 0.5 mm for the Si-detector. In this case, the simulations can reproduce data with the

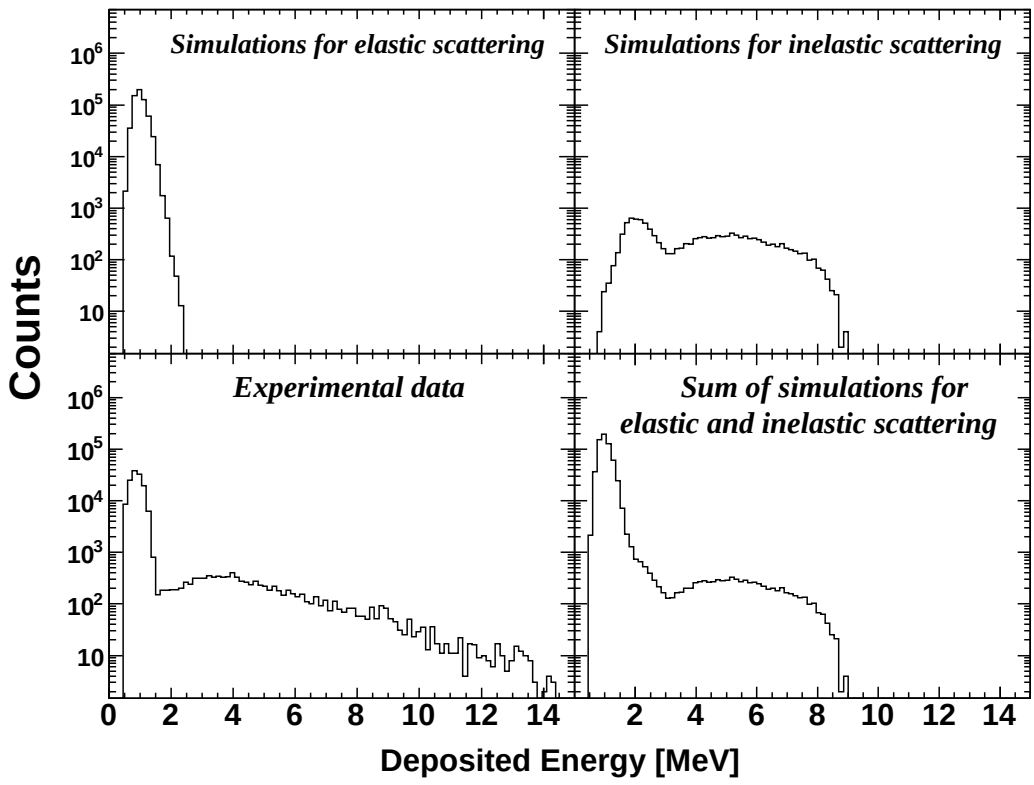


**Figure 1.31:** Same as Fig. 1.30 (solid histograms) but for a 0.5 mm thick Si-detector.

mentioned characteristics. Nevertheless, the tail of the inelastic scattering events in the experimental data is more extended than in the simulations. Simulations show that whatever inelastic scattering channels we consider to have contributed in building up the tail of the experimental data, we cannot reconstruct the contribution corresponding to deposited energies more than $\approx 9$ MeV in this spectrum. This is because a 0.5 mm thick silicon detector is not thick enough to let protons deposit more than about 9 MeV in it. Although the peak position as well as the extension of the peak can be better explained in this case, it is highly improbable that the measurement of the detector thickness had been done with such an uncertainty.

In order to have a consistent picture explaining both the peak position and the end-point of the experimental spectrum, there must have been a combination of a problem with the calibration as well as the nonlinearity behavior of it; the two effects, which are related to the calibration, can shift the experimental peak position toward the higher values of deposited energy and at the same time keep the end-point around the position that simulations predict. Nevertheless, the problem of nonlinearity needs to be further investigated.

# 2. Overall design and future experiments for EXL

The Facility for Antiproton and Ion Research, FAIR, provides unique opportunities in experimental studies on nuclei far off stability, exploring new regions in the chart of nuclides which are of paramount interest in the fields of nuclear structure and astrophysics. The investigations of direct reactions with exotic beams in inverse kinematics gives access to a wide field of nuclear-structure studies in the region far off stability. The objective of the EXL project (Exotic nuclei studied in Light-ion induced reactions at the NESR storage ring) is to capitalize on light-ion induced direct reactions in inverse kinematics by using novel storage-ring techniques and a universal detector system [7]. Light-ion induced direct reactions have been also applied within the last two decades for the investigation of light exotic nuclei with radioactive beams in inverse kinematics [17]. It turned out that the essential nuclear-structure information is deduced from high-resolution measurements at low-momentum transfer. It is exactly because of the kinematical conditions of inverse kinematics that make low-momentum transfer measurements an exclusive domain in storage-ring experiments for studying the unstable nuclei. This way, one can benefit from the luminosities provided in the ring experiments which are superior by orders of magnitude as compared to experiments with external targets.

The possibility of studying low-energy recoil particles is especially important when getting away from the region of stable nuclei, since it will allow us to study large-distance behavior of exotic nuclei. For example, one of the most outstanding discoveries was the finding that nuclei may appear under certain conditions with a qualitatively new type of nuclear structure, so-called "halo" structure [3, 4]. Compared to stable nuclei and nuclei close to stability, in which all the protons and neutrons are essentially distributed uniformly over the nuclear volume, it was found that some light neutron-rich nuclei located at or near the neutron drip line exhibit a widely extended low-density distribution. The low-density distribution is due to nothing else than loosely bound valence neutrons (the halo) surrounding a compact distribution of the majority of nucleons (the core). This phenomenon was a sign of the unusual matter distribution in neutron-rich nuclei near the neutron drip line. It magnifies, among other nuclear structure aspects, the importance of studying such systems in the limits of very low-momentum transfer; aspects like the in-medium interactions in proton-neutron asymmetric nuclear matter, giant resonances with strength distributions totally different from those known in stable nuclei, the shell structure in nuclei of extreme proton-to-neutron asymmetry leading to disappearance of the known magic numbers and, in turn, to the appearance of new shell gaps. These were the motivations to start with the design of a new detection system for

future investigations. Various types of light-ion induced direct reactions serve in these investigations like: elastic scattering of type $(p,p)$, $(\alpha,\alpha)$; inelastic scattering of type $(p,p')$, $(\alpha,\alpha')$; charge exchange reactions of type $(p,n)$, $(d,{}^2\mathrm{He})$; quasi-free reactions of type $(p,2p)$, $(p,pn)$, $(p,p+\mathrm{cluster})$; and transfer reactions of type $(p,t)$, $(p,{}^3\mathrm{He})$, $(p,d)$, $(d,p)$.

Since the domain of low momentum transfer is of interest, extremely thin targets are requested, resulting in too low luminosities if external targets would be used. Likewise, due to their production mechanism, a large momentum spread and large emittance are inherent to the secondary ion beams, which would deteriorate a measurement of the target-recoil momenta and kinetic energies if not counteracted [7]. These problems can be overcome using stored and cooled secondary beams of unstable nuclei interacting with thin internal gas-jet targets. This way we would expect:

- high luminosities due to the continuous beam accumulation and beam recirculation;
- high-resolution detection of low-energy recoil particles due to beam cooling and thin targets; and
- low-background conditions due to pure, windowless targets of H, He, etc.

Within the EXL Technical Proposal, the design of a complex detection setup was investigated with the aim of providing a highly efficient universal detection system. This universal detector system is applicable to a wide class of reactions and would provide high resolution and large solid-angle coverage in kinematically complete measurements. The apparatus, foreseen to be installed at the internal target of the NESR storage cooler ring, is shown schematically in Fig. 2.1. The setup includes:

- a Si-strip and Si(Li) detector array for recoiling target-like reaction products, completed by slow-neutron detectors, and a scintillator array of high granularity for gamma rays and for the total-energy measurement of more energetic target recoils;
- detectors in forward direction for fast ejectiles from the excited projectiles, i.e., for neutrons and light charged particles; and
- heavy-ion detectors for the detection of beam-like reaction products.

All detector components will practically cover the full relevant phase space and have detection efficiencies close to unity.

## 2.1 Overall design of the recoil detector system

The overall design for the recoil and gamma-ray detector for EXL is divided into two major parts, namely the EXL Silicon Particle Array (ESPA), which is assigned to

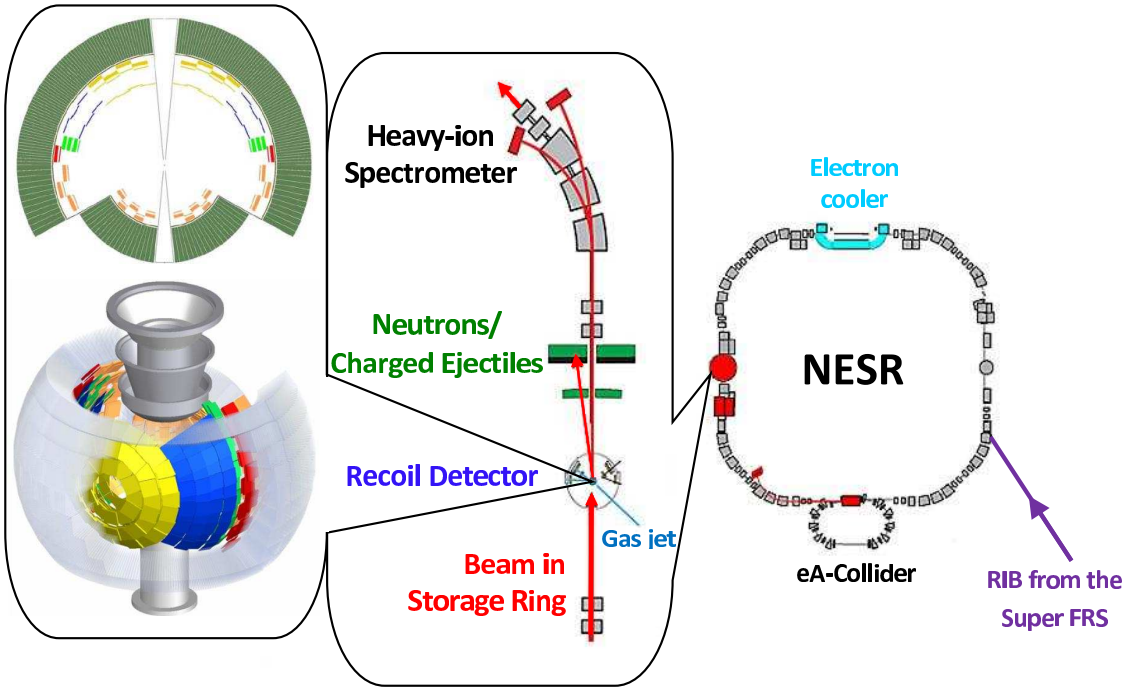


**Figure 2.1:** The EXL detection setup. Right: New Experimental Storage Ring (NESR). Middle: schematic view of the three main parts of EXL. Left: recoil detector setup surrounding the gas-jet target, showing the silicon-detector elements which are covered by the calorimeter crystals. The silicon-detector system consists of five regions covering different angular ranges. These regions are known as A, B, C, D, and E which are colored here as red, green, blue, yellow, and brown, respectively. Except for the region E which covers the scattering angles of $\theta_{LAB} > 90°$, the other four regions are spread over the region with $\theta_{LAB} < 90°$.

detect light charged particles emerging from the target, and the EXL Gamma and Particle Array (EGPA), which covers the whole ESPA solid angle by a scintillator hodoscope and detects the punch-through charged particles as well as the gamma rays. The whole ensemble will be referred to as ERGA (EXL Recoil and Gamma Array). Optionally, low-energy neutrons from $(p, n)$ reactions are detected by the EXL Low-Energy Neutron Array (ELENA). Fig. 2.2 shows some views of the mechanical design (using UGS NX 5), performed at KVI, for the EXL recoil-detector setup. In the realized EXL recoil-detector setup, one has to deal with difficulties like gluing the Si-detector elements to the frame (grid structure) shown on top left-hand side of this figure. The gluing should be performed so neatly, in order to leave a completely sealless spherical structure covered by the Si-detector elements. While this structure would be capable of standing pressure differences of the order of $10^{-5}$ mbar, it should be sealed enough to hold a relative vacuum of $10^{-14}$ mbar for the interior pressure as compared to $10^{-5}$ mbar for the pressure outside the spherical structure.

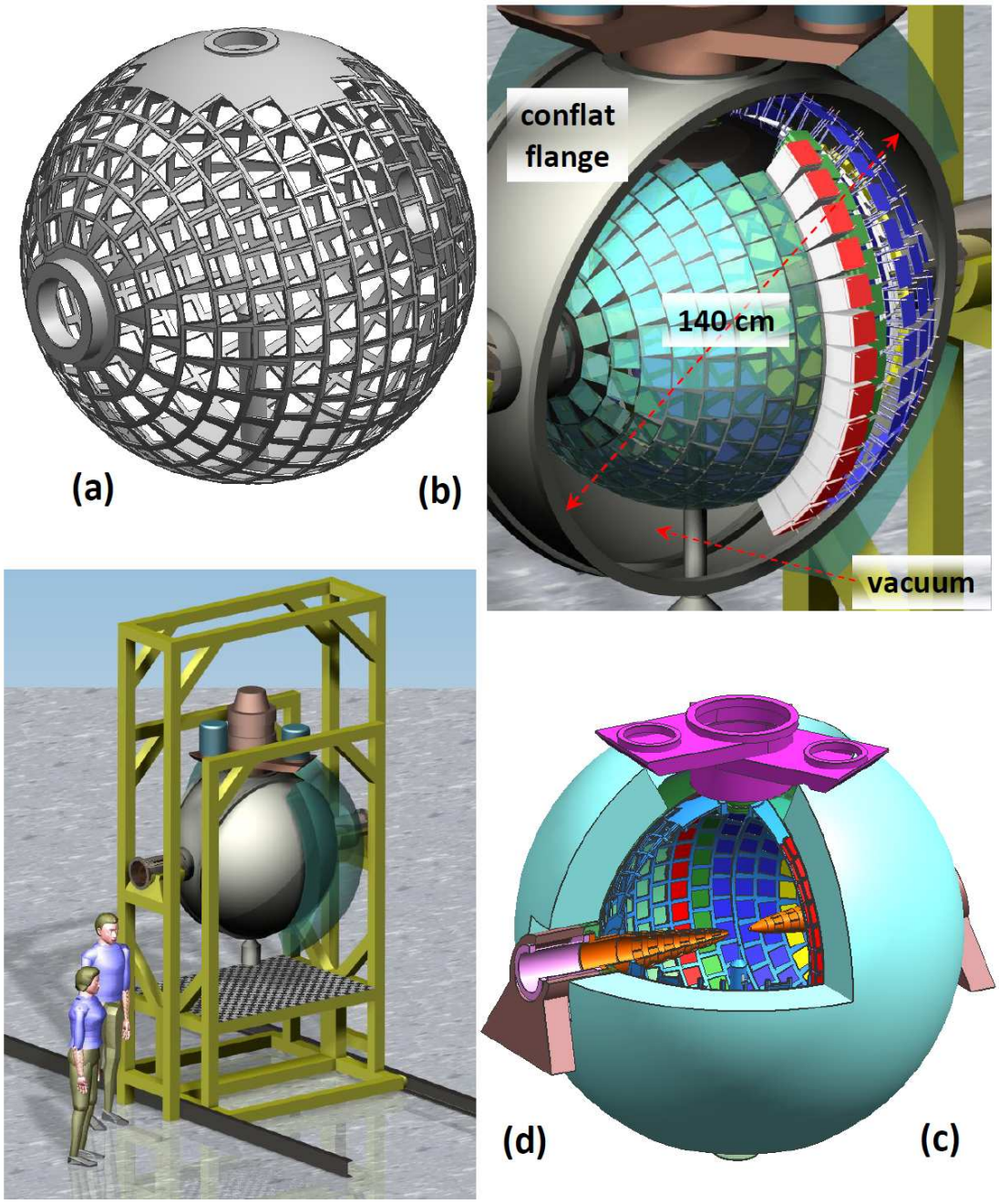


**Figure 2.2:** Mechanical design of various elements of the EXL recoil-detector setup [18]. (a) grid structure for holding the Si-detector elements; (b) Si-detector elements installed on the grid structure and surrounded by the conflat flange; (c) a profile view showing various detection layers. The outermost green layer represents the calorimeter scintillators which are separated from the Si-detectors by a metallic shell holding the vacuum; (d) the outlook of the completed design of the whole recoil-detector setup, installed on a supporting structure.

In contrast, it is the thick spherical shell (connected to the "conflat flange") that would have to stand the high pressure differences of the order of one bar. This shell would separate the calorimeter from the Si-detector elements. More design aspects are outlined in the conceptual design report of EXL [7].

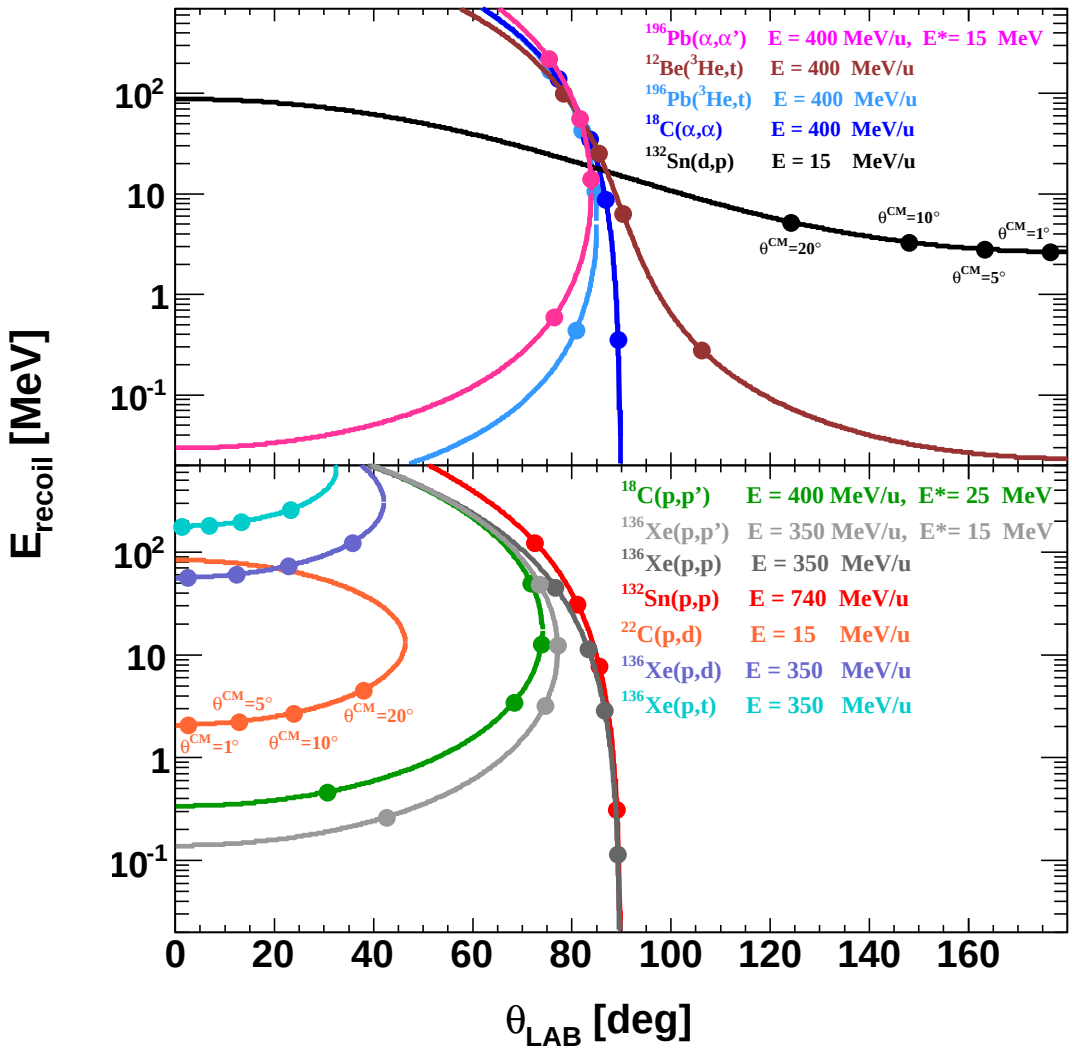


**Figure 2.3:** Kinetic energy of the recoil particle versus its scattering angle, as calculated in inverse kinematics by making use of A.16. Some representative center-of-mass angles for the recoil particle ($\theta_{CM} = 1°, 5°, 10°, 20°$) are also marked on the kinematical curves; the order of the four points on each curve follows the same trend, with respect to the $E_{recoil}$, as those shown for two of the curves. The CM scattering angles are here defined to be supplementary to the ones obtained using A.20. Here, $E^*$ is the excitation energy of the beam particle having undergone inelastic scattering.

### 2.1.1 Kinematical regions of interest

The detector components need to fulfill strong demands concerning angular and energy resolutions, energy threshold, dynamic range, granularity, vacuum compatibility, etc. The kinematical conditions and the resulting constraints on energy resolutions are summarized in Figs. 2.3, 2.4, and 2.5 as well as Tables 2.1 and 2.2 for a few selected typical reactions at different incident energies.

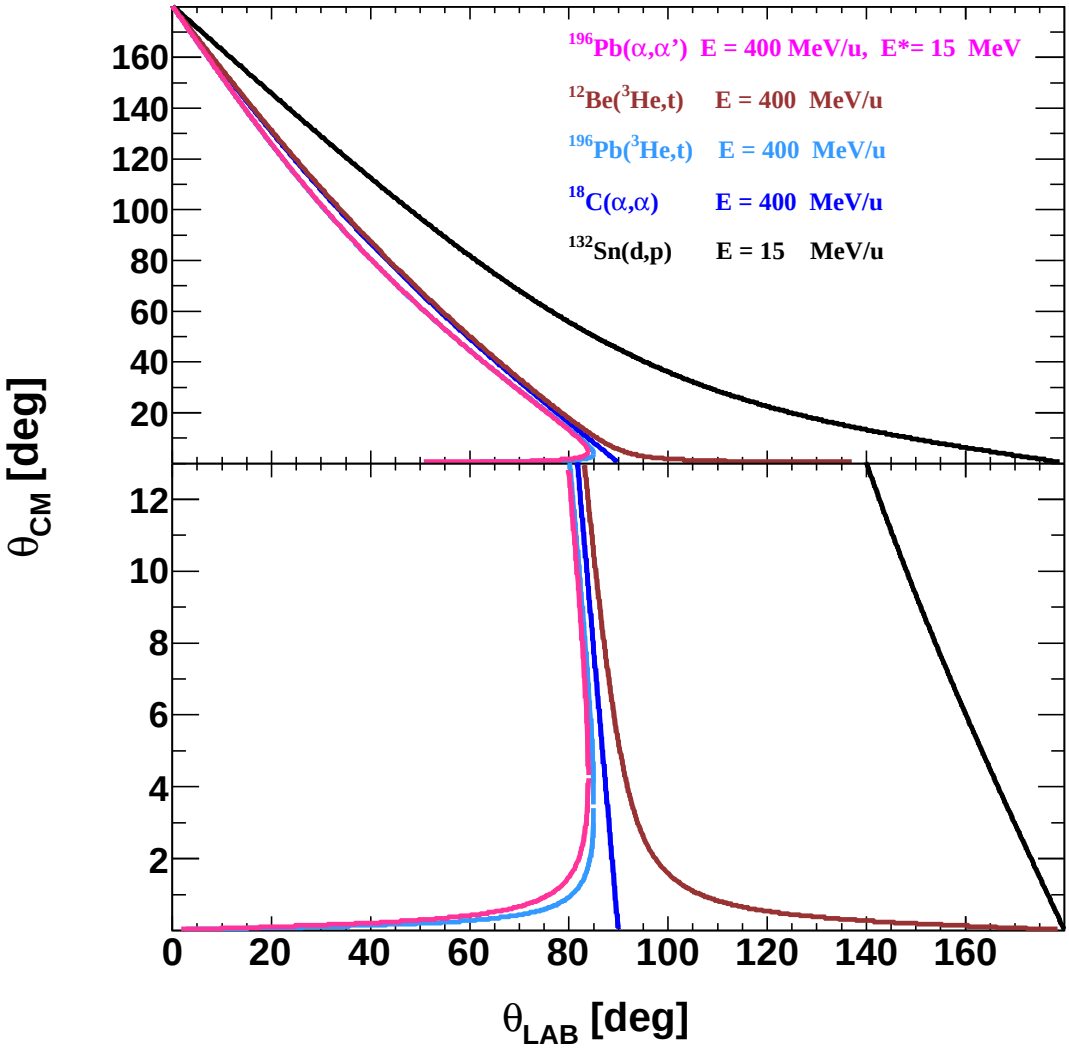


**Figure 2.4:** Same as Fig. 2.3 but for $\theta_{CM}$ instead of kinetic energy. The calculations are based on A.20.

Having in mind that the regular region of interest is, for direct reactions, concentrated for most cases in the CM angular region $0° < \theta_{CM} < 30°$, target-like recoil particles are to be detected in an energy range from about 100 keV up to several hundred MeV, and in an angular region of $30° < \theta_{LAB} < 120°$ (except for transfer

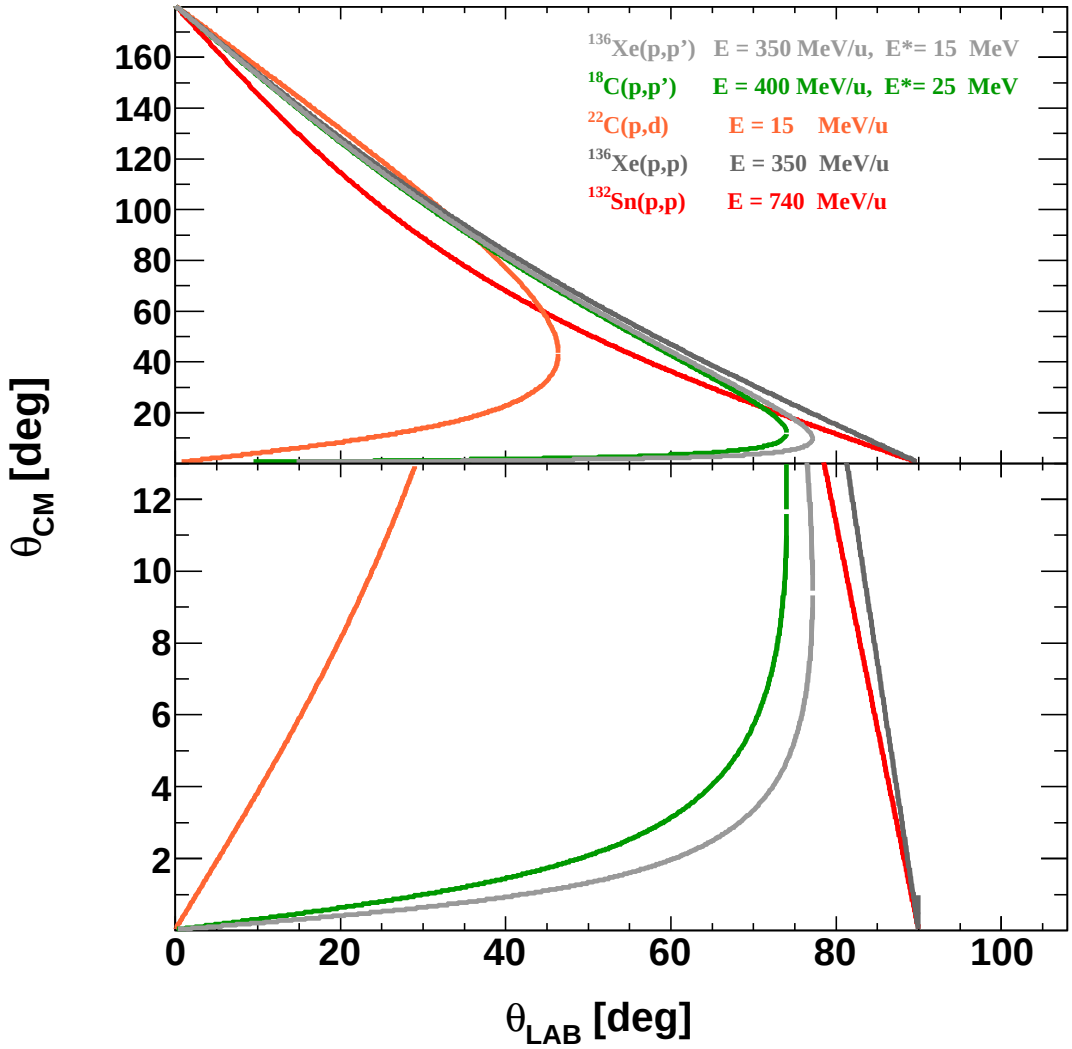


**Figure 2.5:** Same as Fig. 2.4 but for different reaction channels.

reactions, see Fig. 2.3). This defines the constraints concerning detection angle, energy threshold, and dynamic range of the individual detectors. Fig. 2.6 shows the recoil energy as a function of the scattering angle for some selected reactions (shown in Fig. 2.3) which are representative to elastic, inelastic, charge-exchange, and transfer reactions. The dotted curves show the $\pm\sigma$ boundaries for the probability distribution of the kinematical curves when we have a center-of-mass energy resolution of $\sigma = 300$ keV for the recoil particle.

In Tables 2.1 and 2.2 the calculation of the expected resolution ($\sigma = \Delta E^*$) was performed through simulations. In the calculation of the overall resolution of the detector setup we follow the same approach as explained in **??**. Here, we exploit the

**Table 2.1:** Required and expected resolutions for a few selected typical reactions with $E^*$ being the excitation energy of the nucleus (projectile). The required resolution is calculated considering a resolution of 300 keV for the center-of-mass recoil energy. Here, $\sigma^{(\text{detected})}_{E_{\text{recoil}}}$ is the overall energy resolution calculated through simulations for the recoil detector geometry of Fig. **??** without having the UHV shell in the geometry. The superscript (P) is shown for those cases where the majority of the recoil particles punch through the calorimeter. Calculation of $\sigma^{(\text{detected})}_{E_{\text{recoil}}}$ for the three cases in which $\theta_{LAB} \geq 90^\circ$ are yet to be performed after the implementation of the silicon-detector elements of region E (see Fig. 2.1) in the simulations (see the text).

| Reaction<br>E [MeV/u]<br>$E^*$ [MeV] | $\theta_{CM}$<br>($\theta_{LAB}$)<br>[deg] | $E^{LAB}_{\text{recoil}}$<br>[MeV] | Resolution imposed for $\sigma_{E^{CM}_{\text{recoil}}} = 300$ keV<br>$\sigma_{E^{LAB}_{\text{recoil}}}$ [keV] | Resolution expected for EXL setup<br>$\sigma^{(\text{detected})}_{E_{\text{recoil}}}$[keV] |
|---|---|---|---|---|
| $^{12}$Be($^3$He, $t$) | $0.5-5$<br>$(120-91)$ | $0.09-6.3$ | $6-220$ | – |
| 400<br>0 | $5-18$<br>$(91-80)$ | $6.3-81$ | $220-440$ | 40 |
| | $18-25$<br>$(80-75)$ | $81-155$ | $440-460$ | $40-550$ |
| | $25-59$<br>$(75-55)$ | $155-802.1$ | $460-530$ | $550-2650^{(\text{P})}$ |
| $^{132}$Sn($d, p$) | $3-22$<br>$(170-120)$ | $2.8-5.9$ | $90-160$ | – |
| 15<br>0 | $22-45$<br>$(120-90)$ | $5.9-15.3$ | $160-290$ | – |
| $^{136}$Xe($p, p$) | $1.5-14.6$<br>$(89-80)$ | $0.3-26.5$ | $250-440$ | $130-30$ |
| 350<br>0 | $14.6-22.1$<br>$(80-75)$ | $26.5-60.3$ | $440-450$ | $30-140$ |
| | $22.1-37.6$<br>$(75-65)$ | $60.3-170.6$ | $450-470$ | $140-230$ |
| $^{136}$Xe($p, p'$) | a)$5.3-2.5$<br>b)$16.9-35.1$<br>$(75-65)$ | $3.6-0.9$<br>$34.7-145.8$ | $210-40$<br>$650-510$ | 20<br>$80-220$ |
| 350<br>15 | a)$2.5-1.6$<br>b)$35.1-52.6$<br>$(65-55)$ | $0.9-0.4$<br>$145.8-314.6$ | $40-20$<br>$510-530$ | 20<br>$220-420^{(\text{P})}$ |

**Table 2.2:** Continued from Table 2.1.

| Reaction<br>E [MeV/u]<br>$E^*$ [MeV] | $\theta_{CM}$<br>($\theta_{LAB}$)<br>[deg] | $E^{LAB}_{\text{recoil}}$<br>[MeV] | Resolution imposed for $\sigma_{E^{CM}_{\text{recoil}}} = 300$ keV<br>$\sigma_{E^{LAB}_{\text{recoil}}}$ [keV] | Resolution expected for EXL setup<br>$\sigma^{(\text{detected})}_{E_{\text{recoil}}}$[keV] |
|---|---|---|---|---|
| $^{132}$Sn$(p,p)$ | 1.1 – 11.3 | 0.4 – 39.3 | 220 – 340 | 130 – 180 |
| | (89 – 80) | | | |
| | 11.3 – 17.1 | 39.3 – 89.7 | 340 – 350 | 30 – 180 |
| 740 | (80 – 75) | | | |
| 0 | 17.1 – 29.4 | 89.7 – 261.3 | 350 – 380 | 180 – 270 |
| | (75 – 65) | | | |
| $^{18}$C$(\alpha,\alpha)$ | 1.6 – 15.8 | 0.9 – 87.1 | 360 – 470 | 10 – 30 |
| | (89 – 80) | | | |
| | 15.8 – 23.8 | 87.1 – 196.1 | 470 – 480 | 30 – 370 |
| 400 | (80 – 75) | | | |
| 0 | 23.8 – 40.3 | 196.1 – 547.2 | 480 – 500 | 370 – 2200 |
| | (75 – 65) | | | |
| $^{18}$C$(p,p')$ | a)10 – 2.5 | 12.6 – 1.1 | 1050 – 30 | 150 – 20 |
| | b)12.8 – 51.4 | 20.4 – 304.3 | 1650 – 340 | 160 – 300$^{(\text{P})}$ |
| | (74 – 55) | | | |
| 400 | a) 2.5 – 1 | 1.1 – 0.5 | 30 – 12 | 20 |
| 25 | (55 – 30) | | | |
| $^{196}$Pb$(\alpha,\alpha')$ | a)1.5 – 0.9 | 1.3 – 0.5 | 60 – 20 | 20 |
| | b)12.8 – 20.6 | 90.8 – 233.6 | 480 – 460 | 30 – 600 |
| | (80 – 75) | | | |
| 400 | a)0.9 – 0.3 | 0.5 – 0.08 | 20 – 3 | 20 |
| 15 | b)20.6 – 52.5 | 233.6 – 1429 | 460 – 520 | 600 – 4300$^{(\text{P})}$ |
| | (75 – 55) | | | |
| $^{196}$Pb$(^3\text{He},t)$ | a)0.9 – 0.6 | 0.4 – 0.16 | 30 – 14 | 20 |
| | b)13.3 – 20.9 | 75 – 184 | 460 – 450 | 40 – 690 |
| | (80 – 75) | | | |
| 400 | a)0.6 – 0.2 | 0.16 – 0.03 | 14 – 2 | 20 |
| 0 | b)20.9 – 52.5 | 184 – 1094 | 450 – 510 | 690 – 3970$^{(\text{P})}$ |
| | (75 – 55) | | | |
| $^{22}$C$(p,d)$ | a)25 – 4 | 5.9 – 2.3 | 460 – 120 | 30 – 10 |
| 15 | b)74 – 156 | 30.9 – 78 | 1050 – 730 | 40 – 330 |
| 0 | (40 – 10) | | | |

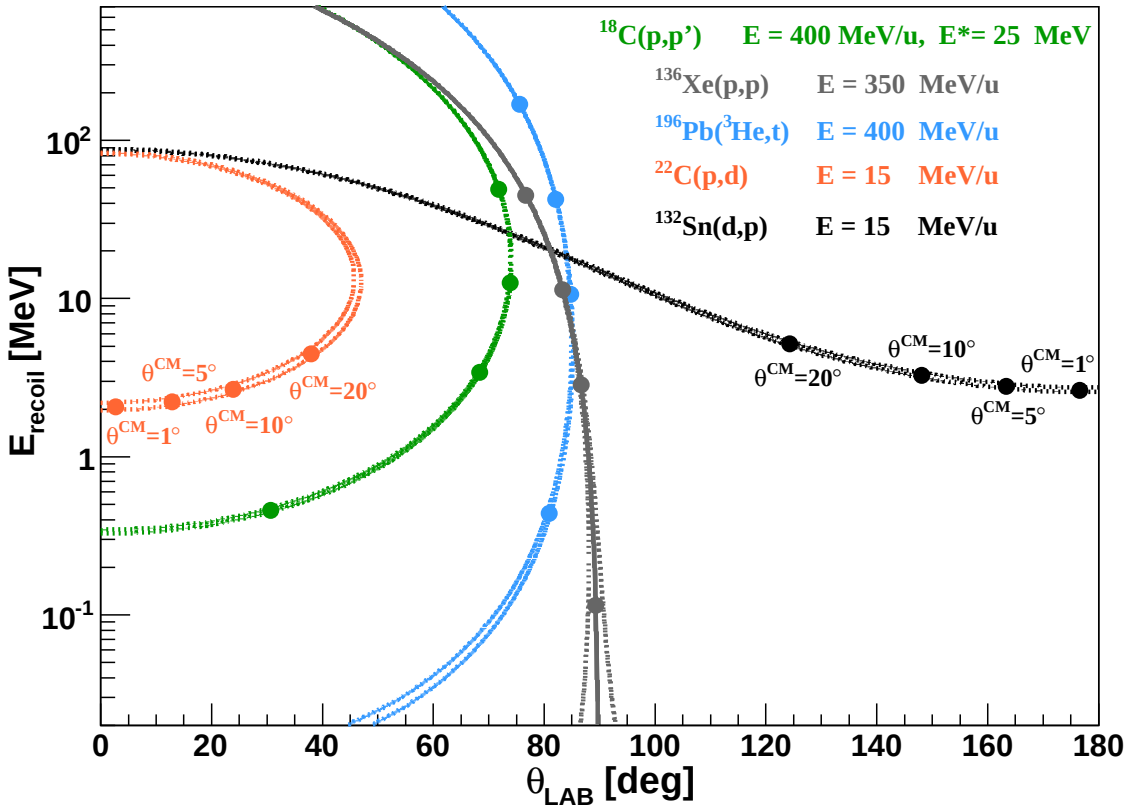


**Figure 2.6:** Same as Fig. 2.3 for some representative reactions. The two dotted curves are corresponding to when we choose the center-of-mass energy of the recoil particle as $E^{CM} = E_0^{CM} \pm 300$ keV, in which $E_0^{CM}$ is the center-of-mass energy of the recoil particle according to the corresponding kinematical curves in Fig. 2.3. Here, the kinematical curve of only $^{136}$Xe$(p,p)$ is shown (solid line); for the other four reactions only the $\sigma = 300$ keV boundaries for the probability distribution of the kinematical curves around $E_0^{CM}$ are shown.

generalized form of Eq. **??** which reads as

$$Histo \rightarrow Fill\Big((E_{sil}^{(tot)} - \mu_{sil}) + (E_{cal}^{(tot)} - \mu_{cal})\Big), \tag{2.1}$$

with $E_{sil}^{(tot)} = \Sigma_i E_{sil}^{(i)}$ and $E_{cal}^{(tot)} = \Sigma_j E_{cal}^{(j)}$, in which $i$ and $j$ run over all the silicon-detector elements and calorimeter crystals that detect energy deposition $E_{sil}$ and $E_{cal}$, respectively, in an event. On the other hand, $\mu_{sil}$ and $\mu_{cal}$ are taken as the means of the Gaussian fits to $\Sigma_k E_{sil}^{(tot)}$ and $\Sigma_k E_{cal}^{(tot)}$ when no detector resolution is folded to silicon-detector elements and calorimeter crystals. Here, $k$ runs over all the events. In the simulations, an intrinsic resolution of FWHM = 50 keV was considered for the Si-detector elements. The resolution of CsI crystals was calculated from Fig. **??** as a function of the deposited energy by the recoil protons

in the individual crystals. For other recoil particles ($d$, $t$, $\alpha$), a resolution of 1% for FWHM was considered. In addition, in order to calculate $\sigma^{(\text{detected})}_{E_{\text{recoil}}}$, I used a Gaussian interaction profile of $\sigma_x = \sigma_y = \sigma_z = 1$ mm as an extended region around the target point within which the recoil particles were generated in the simulations.

For five examples in these tables, we expect the (majority of the) recoil particles to punch through the recoil-detector setup, namely, silicon-detector elements plus calorimeter crystals. For the two reactions $^{18}$C$(p, p')$ and $^{136}$Xe$(p, p')$ with recoil-particle energies of $E^{LAB}_{\text{recoil}} = 304.3$ MeV and 314.6 MeV, respectively, the calculation of resolution was performed based on the energy deposition of those few non-punch-through events (respectively, $\approx 3.5\%$ and 0.5% of the total events). On the other hand, we expect all the events to punch through for the reactions $^{196}$Pb$(^3$He$, t)$, $^{196}$Pb$(\alpha, \alpha')$, and $^{12}$Be$(^3$He$, t)$ with recoil-particle energies of $E_{LAB} = 1094.3$ MeV, 1429.1 MeV, and 802.1 MeV, respectively. In this case, the numbers appeared under $\sigma^{(\text{detected})}_{E_{\text{recoil}}}$ (= 3970 keV, 4300 keV, and 2650 keV, respectively) show the resolutions expected if the kinetic energy of the particles would be measured with 1% resolution after punching through the calorimeter; that is, if one places a thick detector right after the calorimeter to stop these particles with a 1% resolution. In Table 2.1, calculation of the expected resolution $\sigma^{(\text{detected})}_{E_{\text{recoil}}}$ for those cases in which $\theta_{LAB} \geq 90^\circ$ needs to be performed after the implementation of the Si-detector elements of region E (shown schematically in Fig. 2.1) in the simulations. These three cases are $^{12}$Be$(^3$He$, t)$ with $91^\circ \leq \theta_{LAB} \leq 120^\circ$ and $^{132}$Sn$(d, p)$ with $120^\circ \leq \theta_{LAB} \leq 170^\circ$ and $90^\circ \leq \theta_{LAB} \leq 120^\circ$. Considering the range of energies of the corresponding recoil particles ($\leq$ 15.3 MeV), most probably we will have them stopped in the silicon layers (a thickness of 1.6 mm for the Si-detector elements can stop protons of 15.3 MeV). In this case the overall resolution will be the same as the resolution of the silicon elements.

### 2.1.2 Design of upcoming experiments with ESR

Using the simulations, one can calculate the acceptance of different detector elements for various reaction channels. In practice, one can exploit this idea in order to devise a detector setup which is optimized for a specific reaction channel. In the optimization process, one would find the best position for the various detector elements with the aim to maximize the acceptance of individual detectors, while reaching a reasonable coincidence acceptance. For instance, Fig. 2.7 shows the predicted kinematical curves for various reaction channels of $^{56}$Ni in inverse kinematics. It shows the influence of the beam energy as well as the excitation energy on the relation between the kinematical variables $\text{E}_{\text{recoil}}$ and $\theta_{LAB}$. As an example, we consider a proposed experiment with $^{56}$Ni nuclei as beam and $^3$He nuclei as target, in order to find an optimized geometry for the recoil and heavy-ion detectors and derive the respective single and coincidence reaction rates. In the procedure of predicting the reaction rates we would rely on theoretical calculations for the cross section of the channels of interest. Fig. 2.8 shows the theoretical prediction for the cross section

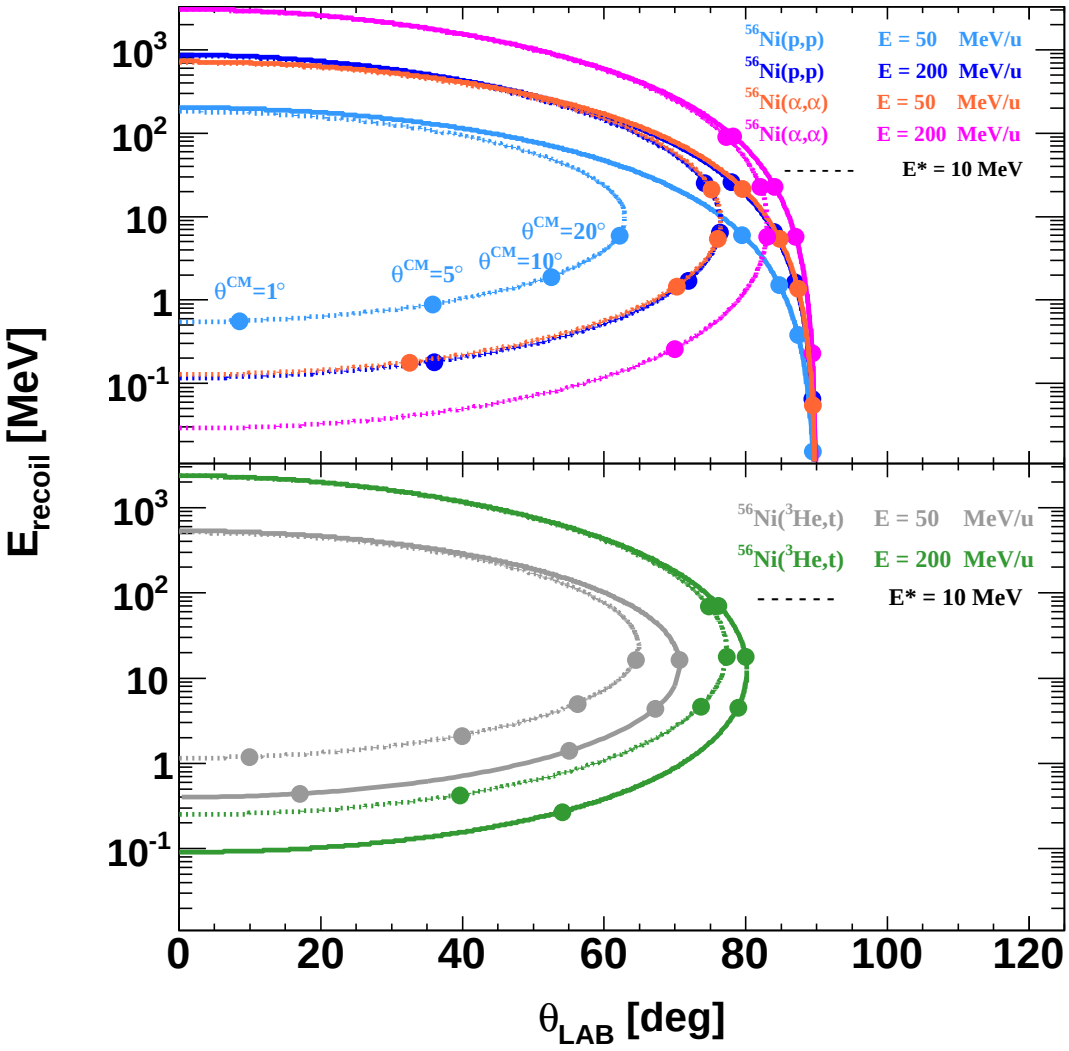


**Figure 2.7:** Top: same as Fig. 2.3 but for $^{56}$Ni$(p,p)$ and $^{56}$Ni$(\alpha,\alpha)$ reactions with beam energies of 50 and 200 MeV/nucleon. The dotted curves show the kinematics, corresponding to the same-color solid curves with no excitation, but considering an excitation energy of $E^* = 10$ MeV for the projectile(-like) nucleus. Bottom: same as top panel for $^{56}$Ni$(^3$He$, t)$ reaction channel. The turning points of the curves are defined as where the low- and high-energy branches meet.

of $^{56}$Ni$(p,n)$ reaction, with beam energies of 50 and 200 MeV/nucleon, as a function of projectile-like excitation energy. It shows that the charge-exchange cross section has a maximum probability at excitation energies around 4 MeV. Fig. 2.9 shows the relation between various kinematical variables of the light ejectile and heavy projectile for a projectile-like excitation energy of 4 MeV for $(p,n)$ and $(^3$He$, t)$ reaction channels. For the sake of illustration, we take for the rest of the discussion the

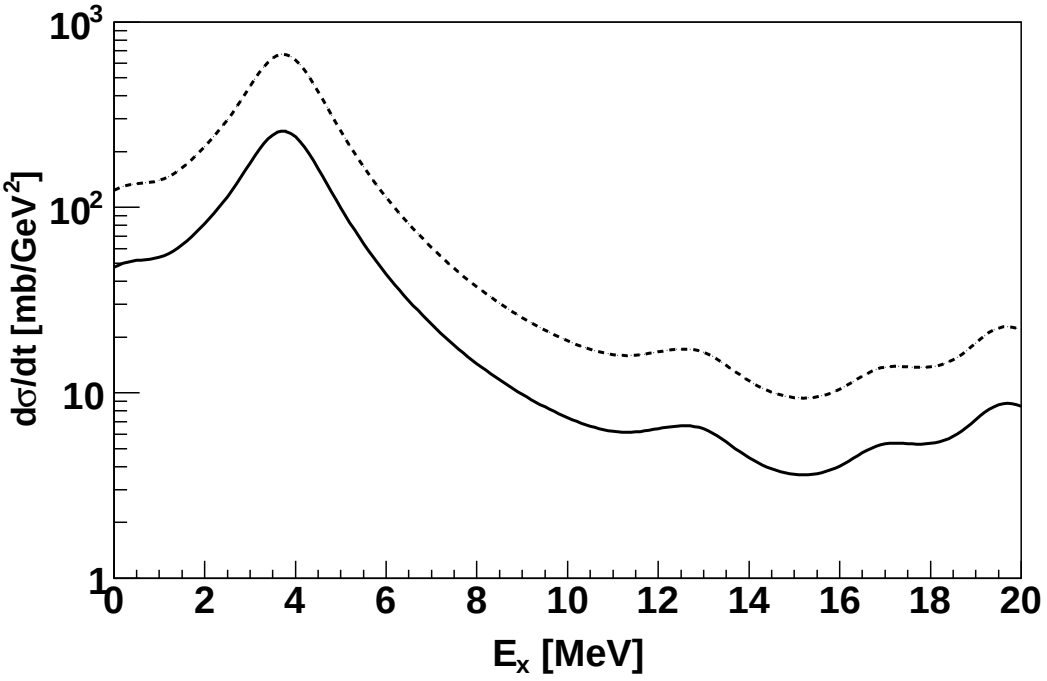


**Figure 2.8:** Theoretical predictions for the differential cross section of $^{56}$Ni$(p, n)$ reaction, with beam energies of 50 (dotted curve) and 200 MeV/nucleon (solid curve), as a function of projectile-like excitation energy [15]. The calculation is performed for the normal kinematics with a light-ion scattering angle of 0.1° in the laboratory frame.

reaction channel $^{56}$Ni$(^3$He$, t)^{56}$Cu for the beam energies 50 and 200 MeV/nucleon.

Consider a detector setup in which we would have a silicon detector with an area of $45 \times 45$ mm$^2$ and a thickness of 300 $\mu$m for the heavy ions (the same dimensions as the p-i-n diode detector in the feasibility experiment 1.3), installed inside the ESR storage ring in possible locations after the dipole magnets. Based on the simulations, the heavy-ion detector would have the highest acceptance for fully-stripped $^{56}$Cu ions, when it is installed right after the last dipole magnet before the quadrupole magnet (see Fig. 1.1 for the geometry of the ESR storage ring). The position optimization for the heavy-ion detector was achieved by moving the detector along (and on both sides of) the beam line as well as changing its distance to the center of the beam pipe. Now consider the low-energy branch of the light-ion kinematics in Fig. 2.9 (recoil energies less than about 17.5 and 15.5 MeV in the $^{56}$Ni$(^3$He$, t)$ reaction channel for the beam energies of 50 and 200 MeV/nucleon, respectively). Based on this convention, the low- and high-energy branches meet at the turning point of $\theta_{LAB}^{(\text{light ion})}$. Having the kinematics of the low-energy branch, there is not much difference in terms of the specific position of this detector in the available space of 70 cm length right after the last dipole magnet. This is the case when we put the detector on the left side of the beam line (when looking along

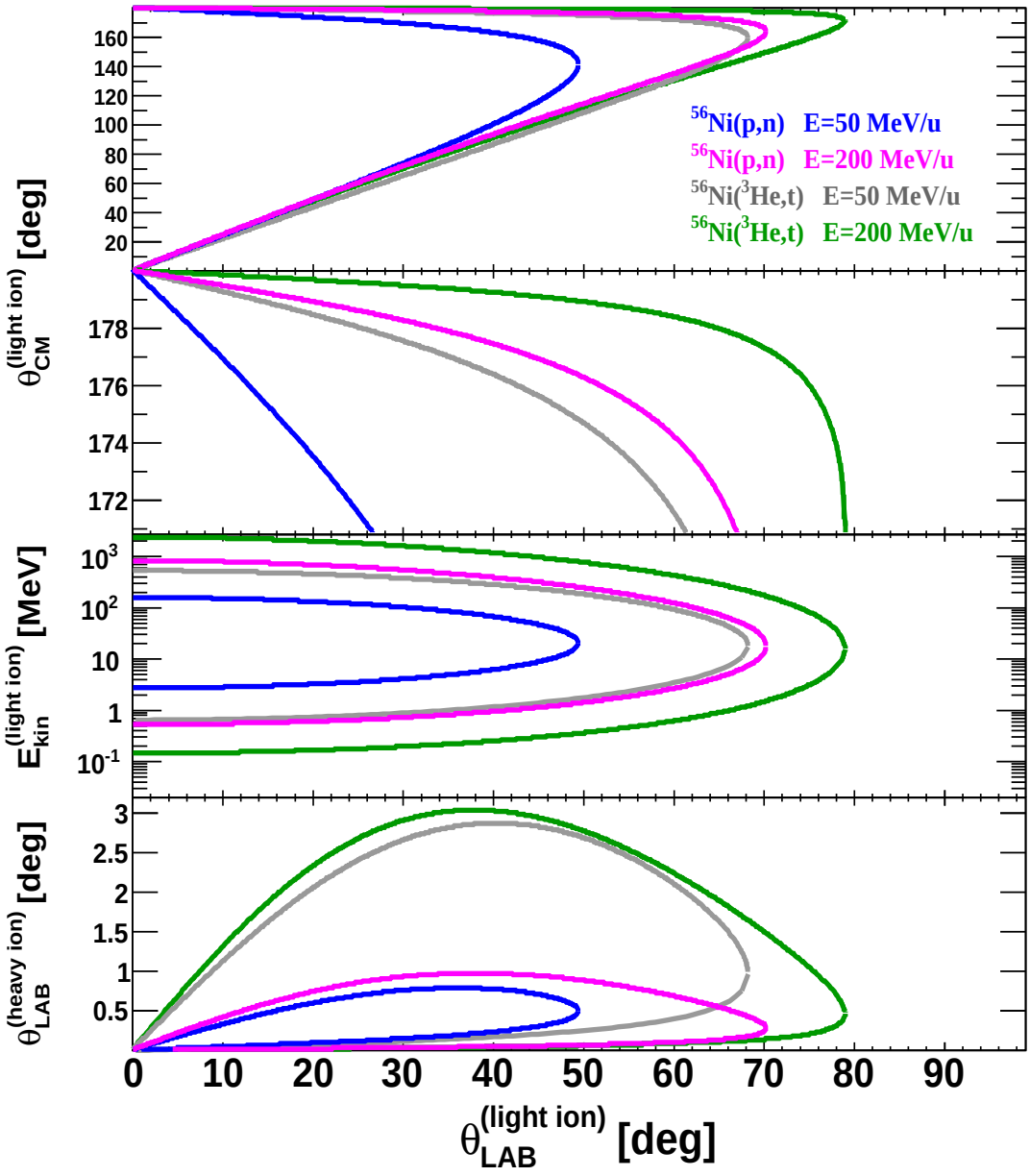


**Figure 2.9:** Top panel: center-of-mass scattering angle of the light ejectile versus its scattering angle in the laboratory frame (LAB) for the reaction channels $^{56}$Ni($^{3}$He, $t$) and $^{56}$Ni($p, n$), with beam energies of 50 and 200 MeV/nucleon and an excitation energy of 4 MeV for $^{56}$Cu ions. The angles are measured with respect to the heavy-ion beam direction. Second panel: the same as above but for a small region of center-of-mass angles. Here, the region close to 180° corresponds to small center-of-mass scattering angles in normal kinematics. Third panel: kinetic energy of the light ejectile versus its laboratory scattering angle. Bottom panel: laboratory scattering angle of the excited $^{56}$Cu versus the laboratory scattering angle of triton.

the direction of the beam), since on the right side the acceptance drops drastically. For the two beam energies, the detector position was fixed at 60 cm after the last dipole magnet perpendicular to the beam direction with its closest edge 5 mm away from the center of the beam pipe. The acceptance of this detector (labeled as $D1$ in

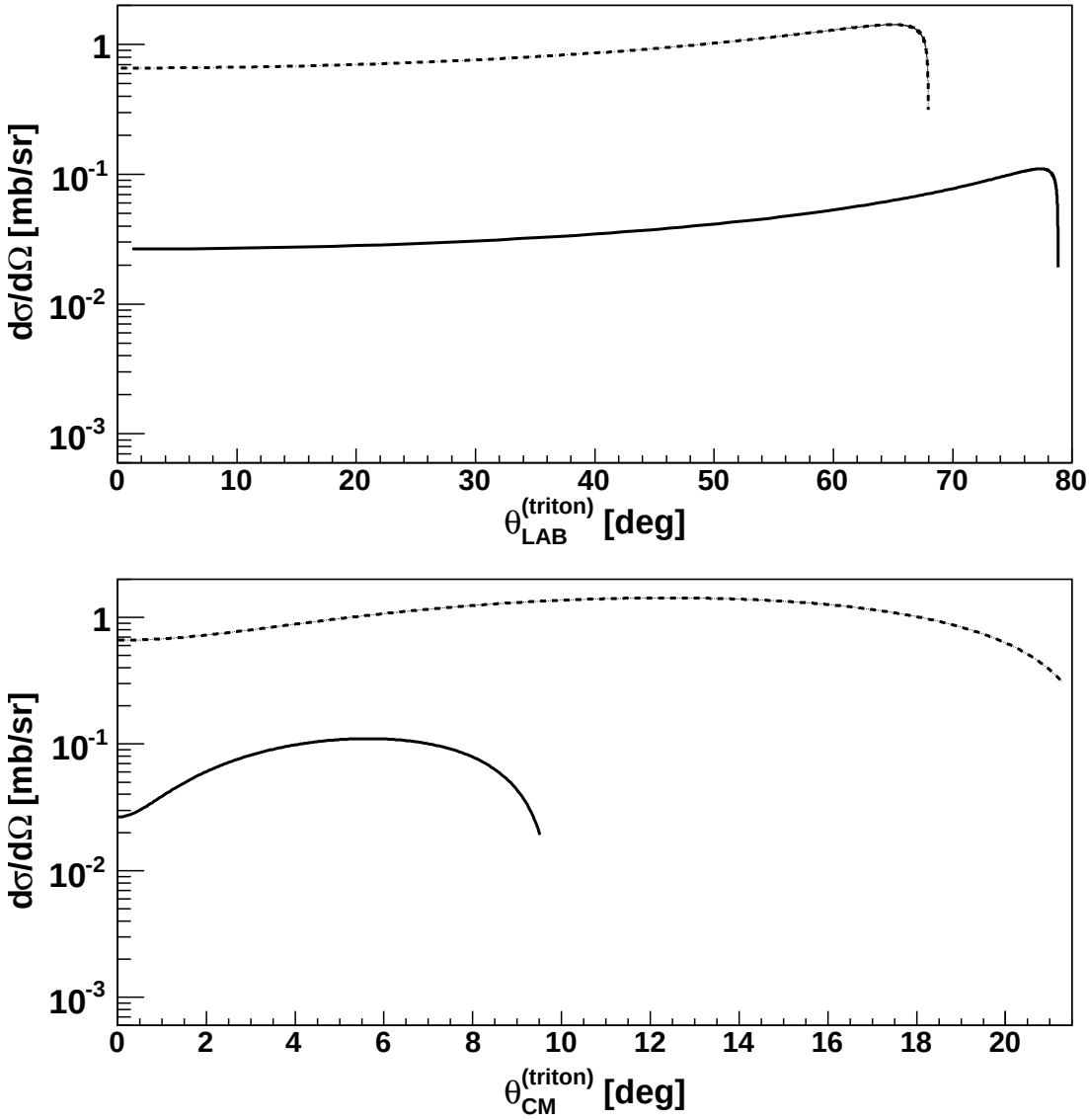


**Figure 2.10:** Theoretical prediction for the inverse-kinematics differential cross section of $^{56}$Ni($^{3}$He, $t$) reaction, with beam energies of 50 (dotted curves) and 200 MeV/nucleon (solid curves), as a function of triton scattering angle in LAB (top panel) and CM (bottom panel) frames [19]. The calculation is performed for a projectile-like excitation energy of 4 MeV and only the cross sections corresponding to the low-energy branch is shown (see Fig. 2.7, bottom panel).

Fig. 2.11) for 50 and 200 MeV/nucleon beam energies was obtained to be 24% and

57% for singles, respectively, when we use a point-like scatterer.

The next stage would be to find the optimized position for the recoil detector setup. For the recoil detector we will have double-sided silicon-strip detectors (DSSD) of 300 $\mu$m thickness and $65 \times 65$ mm$^2$ area. Based on the simulations with the kinematics of low-energy branch, there is no significant difference in the coincidence acceptance of the DSSD detector, whether it is positioned on the right or left side of the beam line inside the target chamber. Using the cross section corresponding to the low-energy branch of the light-ejectile kinematics (Fig. 2.10), we optimized the position of a single DSSD detector in terms of having the maximum amount of coincident events with the heavy-ion detector. The optimization was dictated only by the best angular position for the recoil detector (DSSD (1) in Fig. 2.11) on the left side of the beam line, while the distance of the detector to the center of the interaction profile was set to be 15 cm. This distance is sufficient to cover a range of about 24° for the polar scattering angle, when we have a point-like target. The optimized (in terms of giving the maximum coincidence rate) installation angle for this DSSD detector element was found to be about 53° and 64°, for the beam energies of 50 and 200 MeV/nucleon, respectively. Here, I define the installation angle to be the angle between $\overrightarrow{OR}$ and $\hat{z}$ in Fig. 2.11.

Due to the probable limitations in changing the position of detectors inside the interaction chamber for different beam energies, it is more suitable to work with a common detector geometry for various beam energies. Thus, from now on I will proceed with a common geometry in which $\overrightarrow{OR}$ makes an angle of 53° with $\hat{z}$. Nevertheless, in the discussion of the reaction rates, I will present the reaction rates corresponding to the optimized geometry of DSSD (1) as well, in order to compare with the results of the finalized geometry (see Fig. 2.14). Note that the difference between the optimized and the final geometry would only show up for the 200 MeV/nucleon beam. Having the final geometry, the coincidence acceptance of DSSD (1) with the heavy-ion detector was found to be 2.9% and 0.7% for the beam energies of 50 and 200 MeV/nucleon, respectively, when we have a point-like scatterer. For a Gaussian-type extended interaction profile of $\mathrm{FWHM}_z = 7.4$ mm, $\mathrm{FWHM}_x = 9.0$ mm, and $\mathrm{FWHM}_y = 5.0$ mm, the coincidence acceptance was obtained to be 2.8% (2.9% for the optimized geometry of DSSD (1)) and 0.7% for the beam energies of 50 and 200 MeV/nucleon, respectively. I took the size of the extended interaction profile to be the same as what we had in the feasibility experiment, though it can, in principle, be different.

Apart from DSSD (1) we included six other DSSD elements in the geometry; DSSD (4) has the mirror position of DSSD (1) with respect to the beam direction, DSSD (2) and (3), to be used in combination with DSSD (1), are considered for tracking the light ejectiles, and DSSD (5), (6), and (7) play the same role as DSSD (1), (2), and (3) do, while covering the region of small scattering angles. In order to prevent the deflected heavy ions to hit the DSSD (5) and (7), I ended up with a setup in which $OR''$ makes an angle of about 19° with the beam direction.

In order to obtain the shape of the cross section of a specific reaction channel

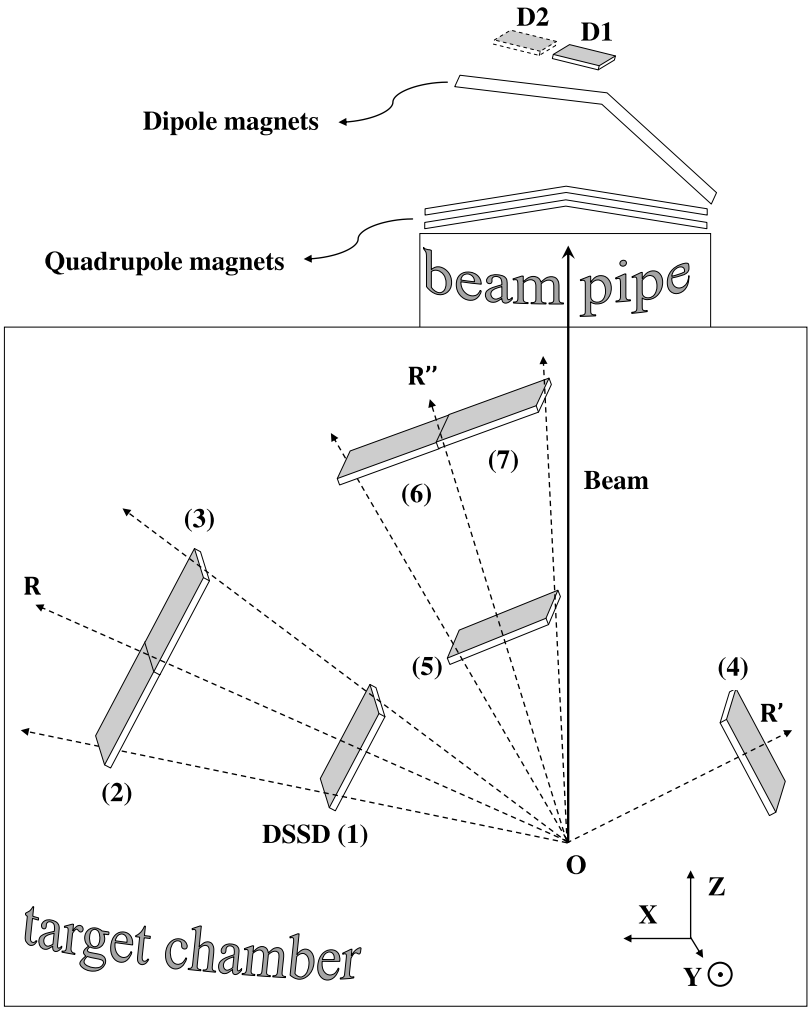


**Figure 2.11:** Schematic view of the ESR recoil Si-detector setup (seven DSSD elements) for the proposed experiment with a beam of $^{56}$Ni and a gas-jet target of $^{3}$He. The lower box represents the interaction chamber which is connected to the beam pipe. The recoil detectors DSSD (1) and (4) are placed symmetric with respect to the beam direction in such a way that their midpoints are 15 cm away from the center of the interaction profile ($O$) and the detector surfaces are perpendicular to the lines connecting $O$ and their midpoints ($OR$ and $OR'$), while two of the sides of their rectangular surfaces are parallel to the direction of gas-jet injection (the $y$-axis). DSSD (2) and (3) are placed next to each other with the same orientation as DSSD (1) in space, but with a distance of 15 cm between their surfaces and the surface of DSSD (1). In the simulations, $OR$ and $OR'$ make an angle of 37° with respect to $\hat{x}$ and $-\hat{x}$, respectively. The detectors DSSD (5), (6), and (7) have the same positions with respect to each other as DSSD (1), (2), and (3) do; $OR''$ makes an angle of 19° with respect to $\hat{z}$. The smallest edge-distance of the heavy-ion detectors $D1$ and $D2$ to the center of the beam pipe are 5 and 60 mm, respectively. $D1$ is approximately 17 m away from $O$.

as a function of scattering angle from the experiment (or simulations), we need to find the respective acceptance as a function of scattering angle. Practically, we need to choose a finite (as opposed to differential) bin size for the scattering angle ($\Delta\theta$). Nevertheless, $\Delta\theta$ should be small enough to show the interesting features of the cross section pattern. Consecutively, we would be able to calculate the corresponding detector count rates for each bin of $\Delta\theta$. In practice, it is the obtained count rates for the consecutive $\Delta\theta$ bins (regions) that would reveal the "measured" shape of the underlying cross section. Dividing the angular range of interest into

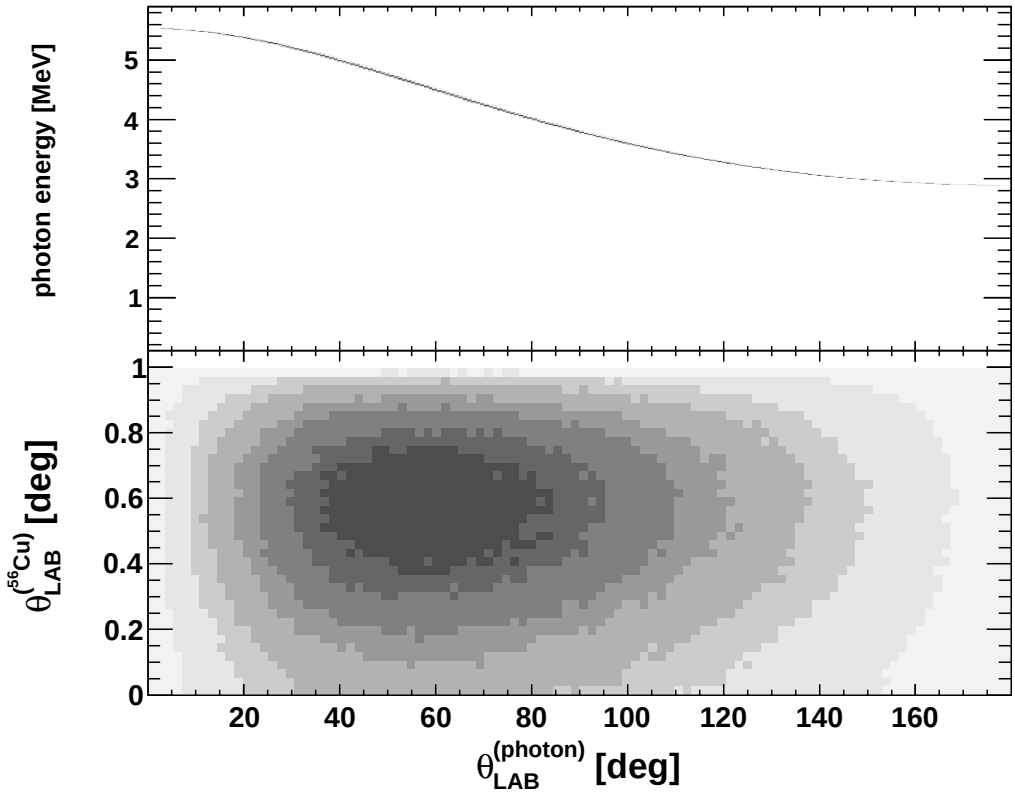


**Figure 2.12:** Top: Energy of the emitted photon in the phase-space decay of $^{56}$Cu$^{*} \rightarrow \gamma + {}^{56}$Cu versus its scattering angle in LAB, considering 4 MeV excitation energy for the daughter nucleus in the reaction channel $^{56}$Ni($^{3}$He, $t$) with a beam energy of 50 MeV/nucleon. Bottom: scattering angle of the de-excited $^{56}$Cu nuclei versus the scattering angle of the emitted $\gamma$ rays. The calculation is done for the kinematics of the low-energy branch (see Fig. 2.9). Different shades in the lower panel refer to different intensities.

$\Delta\theta$ regions of 2° width, we can derive the singles acceptance of a DSSD detector, the singles acceptance of the heavy-ion detector, and the coincidence acceptance of the two detectors for every $\Delta\theta$ region. Tables 2.3 and 2.4 summarize the results. In all the tables presented here, the acceptance of the heavy-ion detector implies the acceptance for $^{56}$Cu ions, de-excited via a phase-space photon decay of the mother

nucleus at the beam-target interaction point. Fig. 2.12 shows the relation between various kinematical variables of the de-excited nuclei and the emitted photons for the low-energy-branch kinematics and 50 MeV/nucleon beam energy.

**Table 2.3:** Acceptance of DSSD (5), the heavy-ion detector $D1$ in Fig. 2.11, and the coincidence acceptance of the two detectors ($a_5$, $b_1$, and $a_{coinc.(5)}$, respectively). The results are from simulations for a detector setup to be installed at the ESR storage ring and for the beam energy of 50 MeV/nucleon (200 MeV/nucleon). The calculation is for the low-energy branch of the reaction channel $^{56}$Ni($^3$He, $t$) with an excitation energy of 4 MeV for the projectile-like particle (see Fig. 2.9), using the theoretical cross sections of Fig. 2.10. The de-excited $^{56}$Cu nuclei were generated (and tracked down) according to the phase space kinematics of an excited nucleus emitting a photon at the center of the interaction profile. "$\theta_{LAB}$-range" represents the triton scattering angle in the laboratory frame.

| $\theta_{LAB}$-range [deg] | $a_5$ [%] | $b_1$ [%] | $a_{coinc.(5)}$ [%] |
|---|---|---|---|
| 1 – 3 | 0.01 (0.02) | 100 (100) | 0.01 (0.02) |
| 3 – 5 | 0.6 (0.5) | 100 (100) | 0.6 (0.5) |
| 5 – 7 | 5.0 (5.0) | 100 (100) | 5.0 (5.0) |
| 7 – 9 | 15.8 (16.6) | 100 (100) | 15.8 (16.6) |
| 9 – 11 | 25.5 (25.7) | 100 (100) | 25.5 (25.7) |
| 11 – 13 | 31.1 (31.5) | 100 (100) | 31.1 (31.5) |
| 13 – 15 | 31.6 (31.5) | 100 (100) | 31.6 (31.5) |
| 15 – 17 | 27.8 (27.0) | 100 (100) | 27.8 (27.0) |
| 17 – 19 | 24.0 (23.7) | 100 (100) | 24.0 (23.7) |
| 19 – 21 | 21.5 (21.2) | 100 (100) | 21.5 (21.2) |
| 21 – 23 | 19.0 (18.9) | 100 (100) | 19.0 (18.9) |
| 23 – 25 | 17.7 (18.2) | 100 (100) | 17.7 (18.2) |
| 25 – 27 | 16.4 (15.7) | 100 (100) | 16.4 (15.7) |
| 27 – 29 | 15.1 (14.3) | 100 (100) | 15.1 (14.3) |
| 29 – 31 | 12.4 (12.6) | 100 (100) | 12.4 (12.6) |
| 31 – 33 | 6.3 (6.2) | 99.9 (100) | 6.3 (6.2) |
| 33 – 35 | 1.0 (1.2) | 99.6 (100) | 1.0 (1.2) |
| 35 – 37 | 0.04 (0.07) | 98.6 (100) | 0.04 (0.07) |

The results presented in Tables 2.3 and 2.4 can, in turn, be used to derive the corresponding reaction rates by making use of B.5. Figs. 2.13 and 2.14 (top panel) show the singles reaction rates of DSSD (1), (4), and (5) as well as their reaction rates in coincidence with the heavy-ion detector, taking a luminosity of $10^{25}$ cm$^{-2}$s$^{-1}$ and beam energies of 50 and 200 MeV/nucleon.

**Table 2.4:** Same as Table 2.3 for DSSD (1) and DSSD (4).

| $\theta_{LAB}$-range [deg] | $a_1$ [%] | $a_4$ [%] | $b_1$ [%] | $a_{coinc.(1)}$ [%] | $a_{coinc.(4)}$ [%] |
|---|---|---|---|---|---|
| 35 – 37 | 0.002 (0) | 0 (0) | 98.6 (100) | 0.002 (0) | 0 (0) |
| 37 – 39 | 0.1 (0.2) | 0.1 (0.2) | 95.9 (100) | 0.1 (0.2) | 0.1 (0.2) |
| 39 – 41 | 2.3 (2.2) | 2.1 (1.9) | 90.1 (100) | 2.3 (2.2) | 2.1 (1.9) |
| 41 – 43 | 6.9 (7.0) | 6.9 (7.1) | 81.4 (100) | 6.9 (7.0) | 6.9 (7.1) |
| 43 – 45 | 9.4 (9.3) | 9.4 (9.4) | 71.4 (100) | 9.4 (9.3) | 9.4 (9.4) |
| 45 – 47 | 9.3 (9.5) | 9.2 (9.1) | 62.1 (100) | 9.3 (9.5) | 9.2 (9.1) |
| 47 – 49 | 9.1 (9.4) | 9.1 (9.2) | 55.4 (100) | 9.1 (9.4) | 9.1 (9.2) |
| 49 – 51 | 8.9 (8.7) | 9.0 (9.0) | 49.9 (100) | 8.9 (8.7) | 9.0 (9.0) |
| 51 – 53 | 8.6 (8.6) | 8.5 (8.7) | 44.8 (100) | 8.6 (8.6) | 8.5 (8.7) |
| 53 – 55 | 8.6 (8.4) | 8.3 (8.6) | 40.4 (100) | 8.6 (8.4) | 8.3 (8.6) |
| 55 – 57 | 8.0 (8.3) | 8.2 (8.4) | 34.6 (100) | 8.0 (8.3) | 6.5 (8.4) |
| 57 – 59 | 8.2 (8.1) | 8.0 (8.0) | 21.7 (100) | 8.2 (8.1) | 0.6 (8.0) |
| 59 – 61 | 7.8 (7.9) | 7.9 (7.8) | 14.9 (100) | 7.8 (7.9) | 0 (7.8) |
| 61 – 63 | 7.6 (7.7) | 7.6 (7.7) | 12.7 (100) | 7.4 (7.7) | 0 (7.7) |
| 63 – 65 | 6.2 (6.3) | 6.2 (6.4) | 3.2 (100) | 1.4 (6.3) | 0 (6.4) |
| 65 – 67 | 2.3 (2.4) | 2.2 (2.4) | 0.0004 (100) | 0 (2.4) | 0 (2.4) |
| 67 – 69 | 0.2 (0.2) | 0.2 (0.2) | 0 (100) | 0 (0.2) | 0 (0.2) |
| 69 – 71 | 0 (0.002) | 0 (0.002) | 0 (99.7) | 0 (0.002) | 0 (0.002) |
| 71 – 73 | 0 (0) | 0 (0) | 0 (96.9) | 0 (0) | 0 (0) |
| 73 – 75 | 0 (0) | 0 (0) | 0 (83.5) | 0 (0) | 0 (0) |
| 75 – 77 | 0 (0) | 0 (0) | 0 (59.1) | 0 (0) | 0 (0) |
| 77 – 79 | 0 (0) | 0 (0) | 0 (31.4) | 0 (0) | 0 (0) |

In order to have a thorough investigation on the reaction rates of a specific reaction channel registered by a detector element, one needs to have an estimation of the rates of other reaction channels in the real experiment. In our case, we need to work out the reaction rates of the high-energy branch as well as the elastic scattering (as a potentially dominant channel and background) rates. It was shown by simulations that the acceptance of the designed recoil detector setup is approximately zero for the elastic events. It is worth mentioning that for the kinematics of the high-energy branch, the acceptance of the heavy-ion detector is significantly reduced. This requires having a second heavy-ion detector installed at a more appropriate location, in order to detect heavy ions originating from the high-energy branch. The optimized location for this detector (labeled as $D2$ in Fig. 2.11) was obtained to be at the same 60 cm after the last dipole magnet, but with an edge distance of 60 mm to the center of the beam pipe (as compared to 5 mm in the case of the heavy-ion detector $D1$). Although the position of this detector is now optimized to detect the heavy ions,

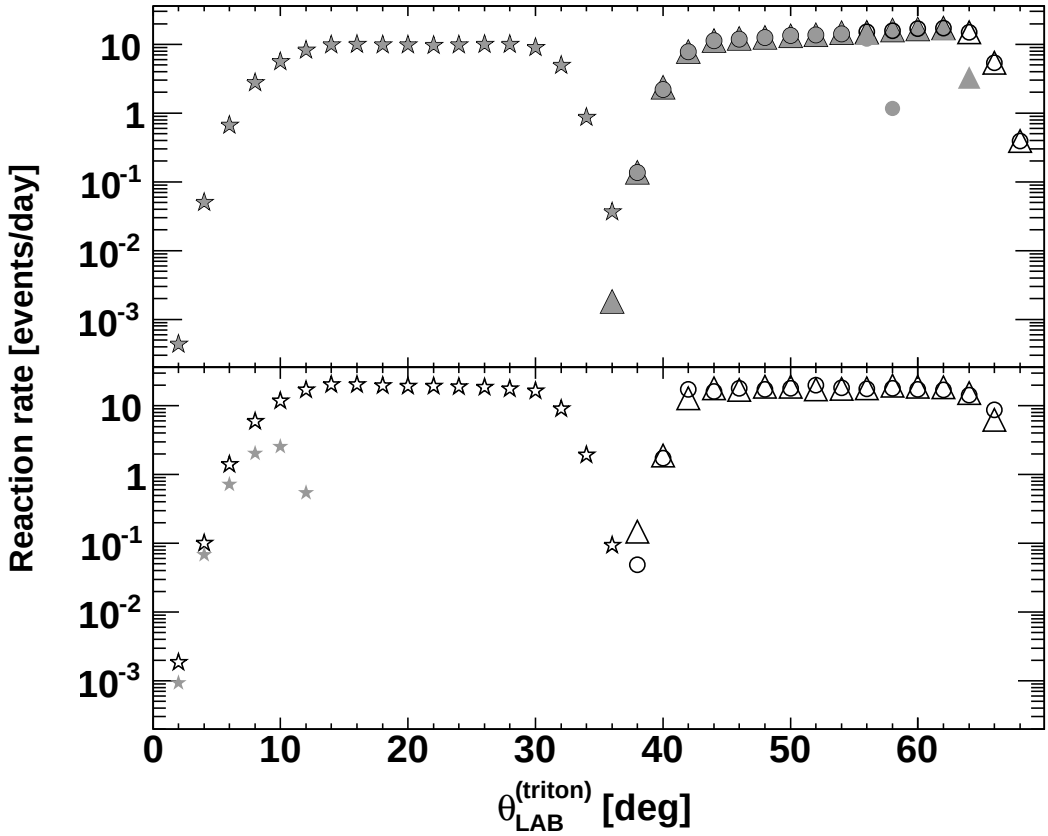


**Figure 2.13:** Top: simulation results showing the reaction rates as a function of triton scattering angle in the reaction $^{56}$Ni($^{3}$He, $t$) for 50 MeV/nucleon beam energy, corresponding to the kinematics of the low-energy branch, as observed by DSSD (1) (hollow triangles), DSSD (4) (hollow circles), and DSSD (5) (hollow stars) as well as the coincidence rates observed by these detector elements and the heavy-ion detector $D1$ in Fig. 2.11 (corresponding solid symbols). Note that the corresponding solid and hollow symbols coincide, for most of the points. A luminosity of $10^{25}$ cm$^{-2}$s$^{-1}$ is considered in the calculations. Bottom: same as top panel but for the high-energy branch. For the high-energy branch, we considered a uniform distribution for the cross section equal to 1.4 mb/sr (see the text). The effect of the acceptance can be seen in the dropping behavior of data points at positions close to the edges of individual detectors. Here, the solid stars are the coincidence rates registered by DSSD (5) and the heavy-ion detector $D2$.

there will be few or no tritons detected in coincidence by various DSSD elements.The corresponding reaction rates are shown in the bottom panels of Figs. 2.13 and 2.14. In order to calculate the reaction rates corresponding to the high-energy branch, we considered a uniform distribution for the cross section equal to 1.4 and 0.1 mb/sr for the beam energies of 50 and 200 MeV/nucleon, respectively. This way, we would have an overestimation of the reaction rates corresponding to high-energy branch;

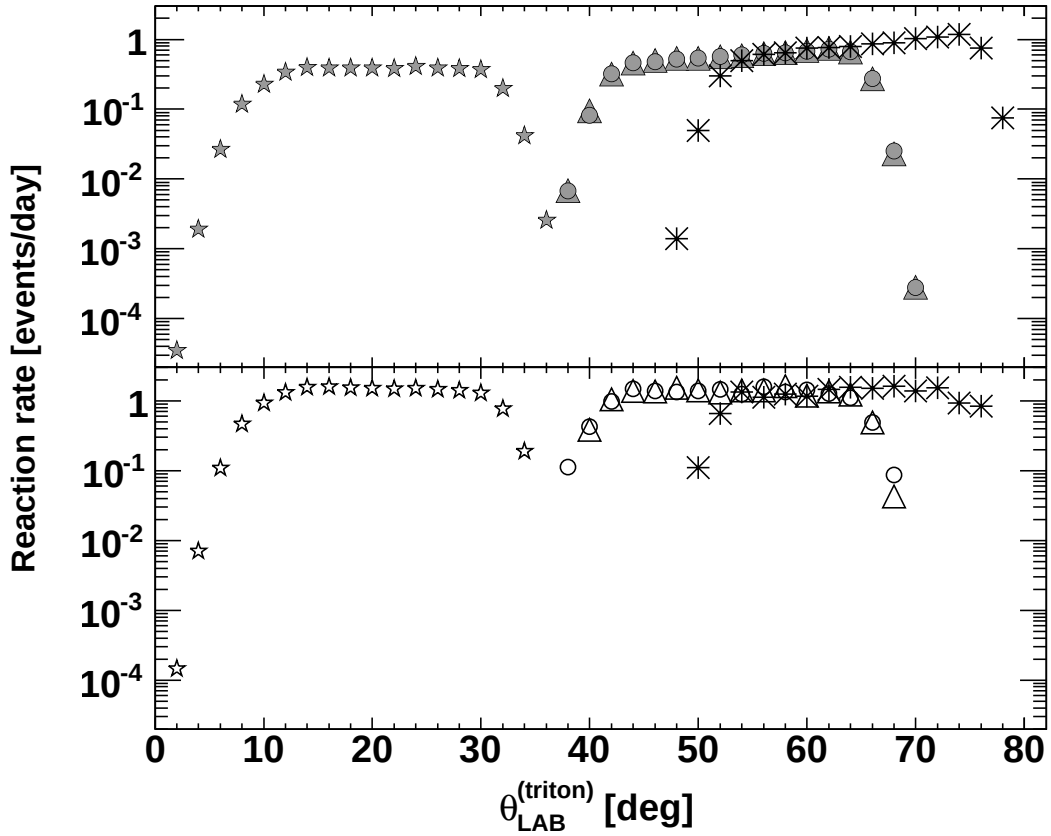


**Figure 2.14:** Same as Fig. 2.13 for the beam energy of 200 MeV/nucleon. For the high-energy branch, we considered a uniform distribution for the cross section equal to 0.1 mb/sr (see the text). The asterisks show the reaction rates observed by DSSD (1) when it is installed at the optimized angle of 64° (instead of 53°) with respect to $\hat{z}$ (see the text).

the actual cross sections are much smaller than these values (see Fig. 2.10). This overestimation allows us to investigate the ratio of the reaction rates corresponding to the low- and high-energy branches. In principle, one should expect a better discrimination of the low-energy-branch events over the high-energy-branch ones in the real experiment. Based on the results of these figures, the heavy-ion detector $D1$ has (approximately) 100% acceptance for the $^{56}$Cu ions corresponding to the kinematics of low-energy branch for the beam energy of 200 (50 MeV/nucleon). In the case of the high-energy branch, only DSSD (5), at beam energy of 50 MeV/nucleon, is capable of registering coincidences with $D2$. As expected, the extracted data points, for the two branches of kinematics, reveal the same trend as the generator cross section of Fig. 2.10. Based on the derived reaction rates from simulations we can have an estimation of the relative errors in determining the cross section. Fig. 2.15 shows the results for the two beam energies and a luminosity of $10^{25}$ cm$^{-2}$s$^{-1}$, with ten days run-time. For the angular range between 11° and 65° (except for the interval

$[31°, 41°]$), the relative error of measurement is obtained to be less than 11% (54%) for the beam energy of 50 (200 MeV/nucleon). For the estimation of the error bars, we have made use of the singles reaction rates of DSSD (1) and (5).

Obeying the kinematics of the low-energy branch (Fig. 2.9), tritons can hardly punch through DSSD (1), making it impossible to track them by DSSD (2) or DSSD (3). Whereas, having the kinematics of the high-energy branch, tritons can be tracked exploiting the latter two recoil detectors (see Fig. 2.11). Fig. 2.16 shows the reconstructed triton scattering angle for the events that are detected by two consecutive DSSD elements (like DSSD (1) and DSSD (2)), as obtained from the simulations. The linear diagonal pattern that shows the relation between the thrown scattering angle and the reconstructed one indicates how good the reconstruction can be performed. In the simulations, a pixel size of $1 \times 1$ mm$^2$ was assumed for the DSSD detectors. The position of the hit pixel is reconstructed from the real position of the hit. The real $x$- and $y$-positions of the hit are extracted from the entrance and exit windows of each DSSD detector. If the particle stops in the detector element, the $x$- and $y$-positions of the hit would be retrieved from the entrance window of the DSSD detector element. The extracted $x$- or $y$-position then gets replaced with the $x$- or $y$-position of the closest pixel center, which would be registered as the reconstructed hit point. The line that connects two reconstructed hit points on two consecutive DSSD detectors (like DSSD (1) and DSSD (2)) would eventually represent the reconstructed scattering direction.

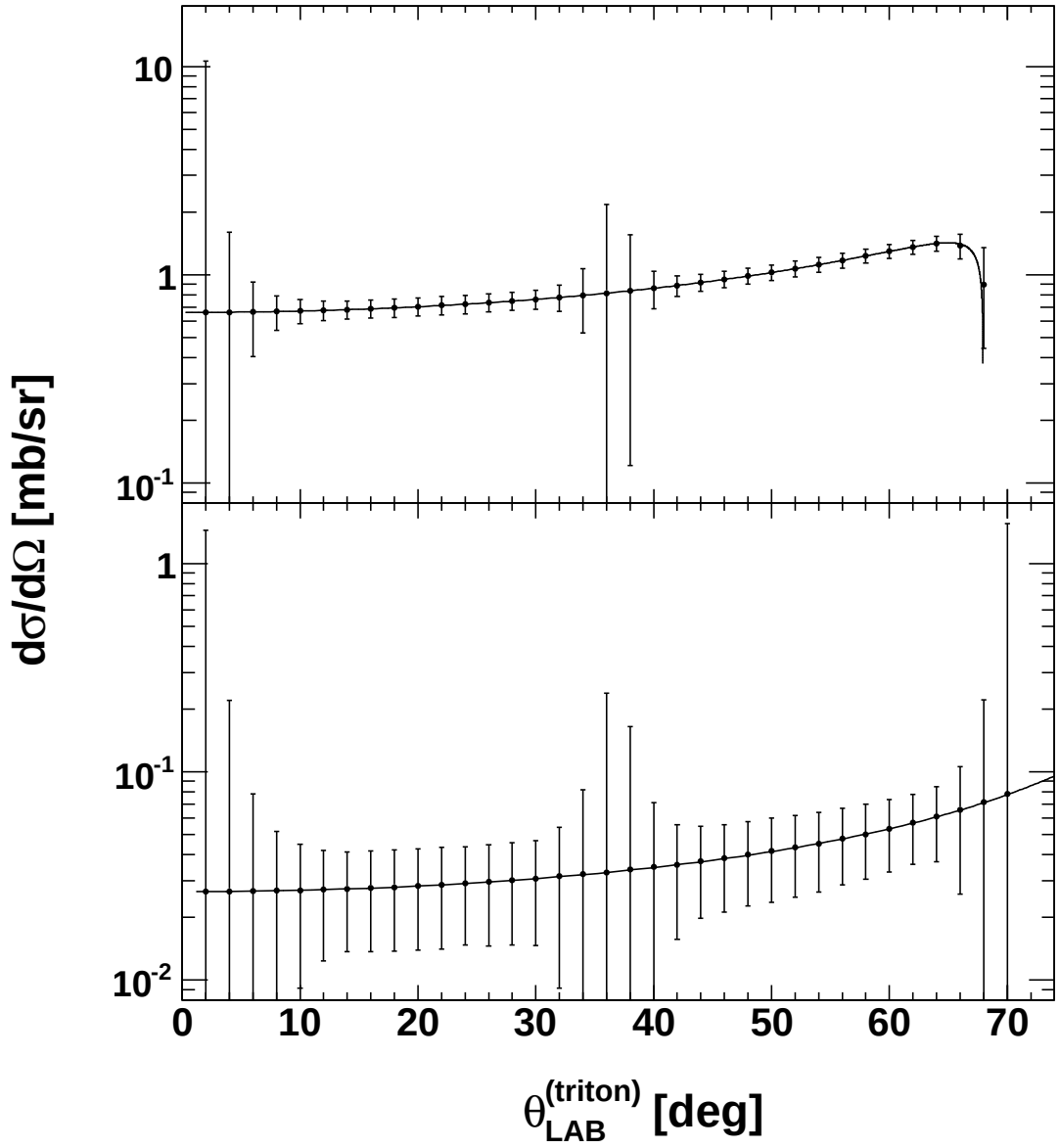


**Figure 2.15:** The extracted cross sections for the low-energy branch of the reaction channel $^{56}$Ni($^{3}$He, $t$), based on the reaction rates of Figs. 2.13 and 2.14 for the beam energies of 50 (top panel) and 200 MeV/nucleon (bottom panel). The error bars are statistical and are estimated to be attainable after ten days of running the experiment, with the assumption of having a luminosity of $10^{25}$ cm$^{-2}$s$^{-1}$. The error bar estimation was done exploiting the singles reaction rates of DSSD (1) and (5). The curves show the theoretical cross sections of Fig. 2.10.

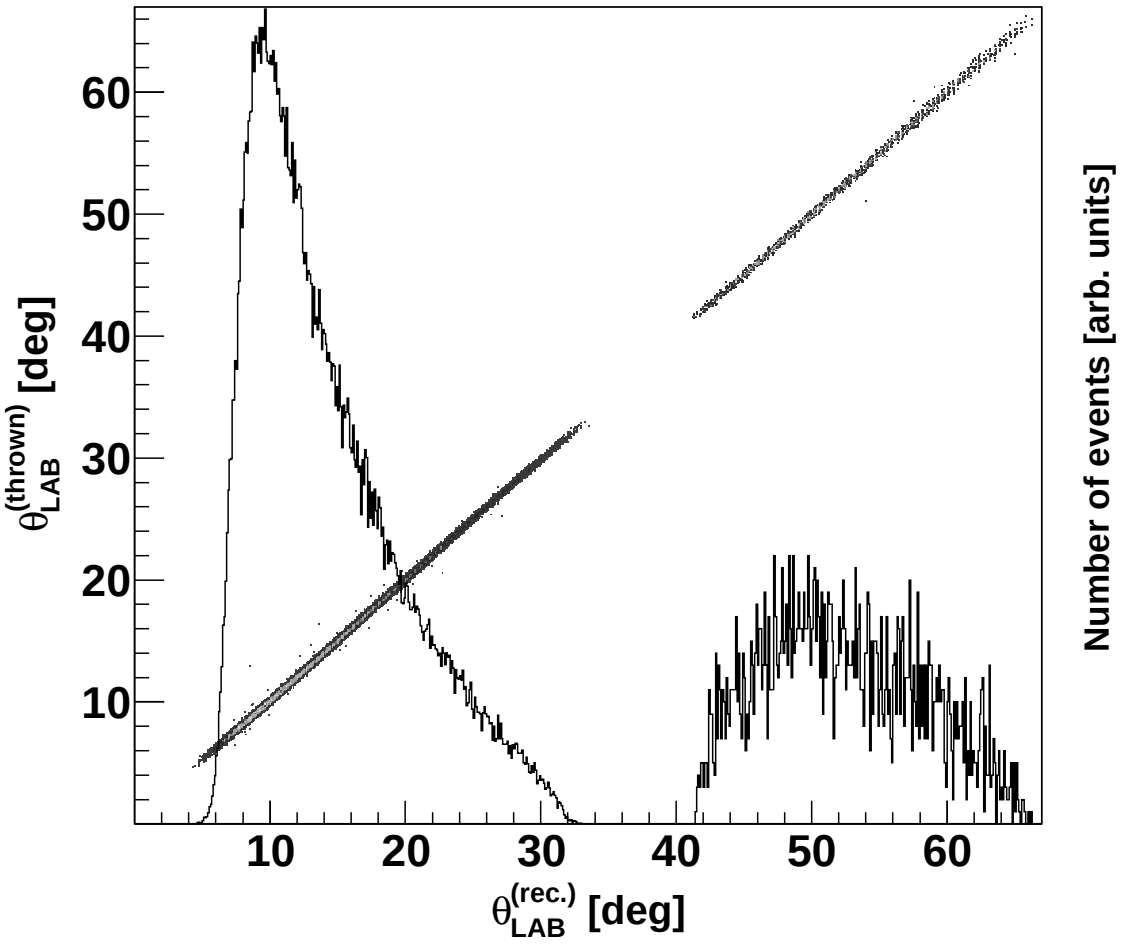


**Figure 2.16:** 2D histogram: The real scattering angle of tritons, as generated in the simulations, versus the reconstructed one by the combination of DSSD (1) and DSSD (2), DSSD (1) and DSSD (3), DSSD (5) and DSSD (6), or DSSD (5) and DSSD (7). The results are for the high-energy branch of the reaction channel $^{56}$Ni($^{3}$He, $t$) with a beam energy of 50 MeV/nucleon. The 1D histogram shows the reconstructed angle for those events that are detected by two consecutive DSSD elements. The left peak is scaled down by a factor of 20.

# A. Relativistic kinematics for two-body interactions

## A.1 Kinematics

In this appendix we try to derive the important kinematical parameters in a two-body interaction. While the energy-momentum conservation restricts the possible configurations between ingoing and outgoing particles in a collision, two arguments make kinematical considerations important in the treatment of collision problems. First, experiments are performed in the laboratory system (LAB) in which the target particle is often at rest. Second, calculations are mostly performed in the center-of-mass (CM) frame, since the dynamics depends only on the relative motion of the colliding particles. To compare theoretical computations with experimental results, one needs to transform from one frame to the other. To link experiments and computations, it is necessary to find the connections between energies, momenta, angles, and cross sections in the two systems, before and after collision.

To establish these connections, we use the Lorentz transformation and conservation of energy and momentum. Although from the point of view of relativistic mechanics all coordinate systems are equal, for practical purposes, however, LAB and CM frames are the two systems of particular importance. All direct observations are in the laboratory system, so it is convenient to use it for reporting experimental results. The CM coordinate system is convenient to use, since in this system the disintegration and collision processes for two particles have the maximum degree of symmetry [20]. Thus, for example if there are no polarization effects, the disintegration of one particle into two others is characterized by a spherically symmetric distribution of secondary particles in the center-of-mass frame.

### A.1.1 Kinematical invariants

The Lorentz transformations can always be performed in order to derive the kinematical variables of interest. Alternatively, we can make use of the appropriate kinematical invariants. This way, the use of the Lorentz transformations is unnecessary. Relativistic invariants have the same value in any system, hence we can express them in a system where they have the simplest form. It is convenient to consider the Mandelstam variables $s$, $t$, and $u$, which are expressed in terms of dot products of the relevant four vectors, as an appropriate set of kinematical invariants in an interaction. This is particularly useful for the case where two particles interact, resulting in only two emerging particles. Take the case of two incoming particles

1 and 2 scattering to produce two outgoing particles 3 and 4 (Fig. A.1). One can

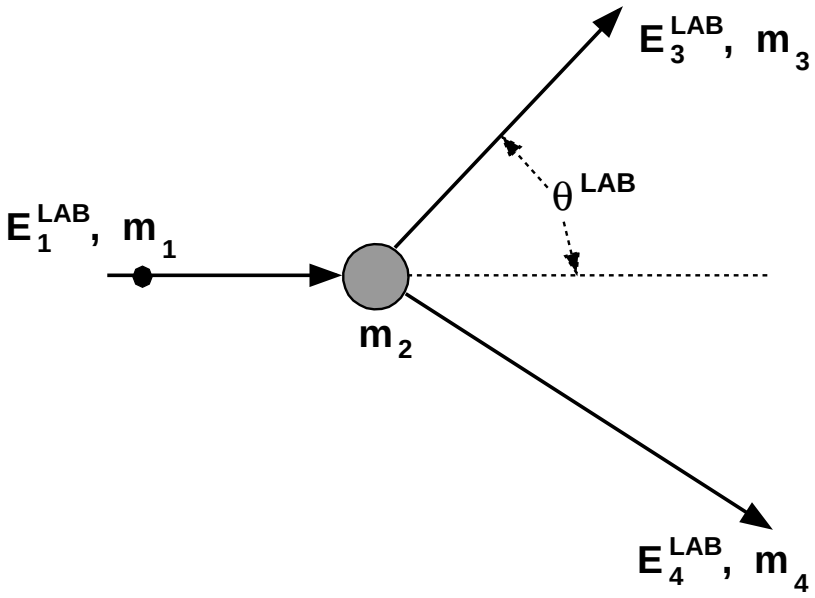


**Figure A.1:** Scattering variables in a typical two-body scattering. Here, $m_i$ is the rest mass of the $i^{th}$ particle and $m_2$ is considered to be at rest in LAB frame. ${E_i}^{LAB}$ represents the total energy of the $i^{th}$ particle in LAB.

define $s$ as the square of the total energy in the CM frame, $t$ as the square of the four-momentum transfer, and $u$ as the crossed four-momentum transfer squared as follows:

$$\begin{aligned} s &= (p_1 + p_2)^2 = (p_3 + p_4)^2 \\ t &= (p_1 - p_3)^2 = (p_4 - p_2)^2 \\ u &= (p_1 - p_4)^2 = (p_3 - p_2)^2, \end{aligned} \tag{A.1}$$

from which it follows that (we use hereafter natural units; $\hbar = c = 1$):

$$s + t + u = {m_1}^2 + {m_2}^2 + {m_3}^2 + {m_4}^2 = const., \tag{A.2}$$

which shows that only two of the three invariants are independent. Experimentally, the total energy of the beam particle in the LAB frame (${E_1}^{LAB}$), mass of the beam particle ($m_1$), and target-particle mass ($m_2$) are fixed. Thus, for given outgoing masses $m_3$ and $m_4$ and for a particular scattering angle $\theta^{LAB}$, the corresponding energies ${E_3}^{LAB}$ and ${E_4}^{LAB}$ can be computed from the four-momentum conservation relation:

$$p_1 + p_2 = p_3 + p_4. \tag{A.3}$$

The kinematical invariant $s$ is then given by:

$$s \equiv (p_1 + p_2)^2{}_{CM} = \left({E_1}^{CM} + {E_2}^{CM},\ 0\right)^2 = \left({E_3}^{CM} + {E_4}^{CM},\ 0\right)^2 \tag{A.4}$$

$$\equiv (p_1 + p_2)^2{}_{LAB} = \left({E_1}^{LAB} + m_2,\ \overrightarrow{p_1}^{LAB}\right)^2 = {m_1}^2 + {m_2}^2 + 2m_2{E_1}^{LAB}.$$

Similarly:

$$\begin{aligned} t &= {m_1}^2 + {m_3}^2 + 2\left(\overrightarrow{p_1} \cdot \overrightarrow{p_3} - E_1E_3\right) \\ &= {m_2}^2 + {m_4}^2 - 2m_2{E_4}^{LAB} \end{aligned} \tag{A.5}$$

$$\begin{aligned} u &= {m_1}^2 + {m_4}^2 + 2\left(\overrightarrow{p_1} \cdot \overrightarrow{p_4} - E_1E_4\right) \\ &= {m_2}^2 + {m_3}^2 - 2m_2{E_3}^{LAB}, \end{aligned} \tag{A.6}$$

in which $E_i$ and $\overrightarrow{p_i}$ are total energy and three-momentum of the $i^{th}$ particle in an arbitrary coordinate system.

Inserting ${E_i}^{CM} = \left(\left(\overrightarrow{p_i}^{CM}\right)^2 + {m_i}^2\right)^{1/2}$, as the total energy of the $i^{th}$ particle in CM frame, into the first equation of A.4 and knowing that $|\overrightarrow{p_1}^{CM}| = |\overrightarrow{p_2}^{CM}|$ and $|\overrightarrow{p_3}^{CM}| = |\overrightarrow{p_4}^{CM}|$ we can obtain the magnitude of the CM momenta as follows:

$$\begin{aligned} |\overrightarrow{p_1}^{CM}| &= \frac{1}{2\sqrt{s}} \cdot \omega\left(s, {m_1}^2, {m_2}^2\right), \\ |\overrightarrow{p_3}^{CM}| &= \frac{1}{2\sqrt{s}} \cdot \omega\left(s, {m_3}^2, {m_4}^2\right), \end{aligned} \tag{A.7}$$

with

$$\omega(x, y, z) = \sqrt{x^2 + y^2 + z^2 - 2xy - 2yz - 2xz}. \tag{A.8}$$

From Eqs. A.4, A.5, and A.6 for a fixed target particle in LAB (${E_2}^{LAB} = m_2$) we obtain

$$\begin{aligned} {E_1}^{LAB} &= \left(s - {m_1}^2 - {m_2}^2\right)/2m_2, \\ {E_3}^{LAB} &= \left({m_2}^2 + {m_3}^2 - u\right)/2m_2, \\ {E_4}^{LAB} &= \left({m_2}^2 + {m_4}^2 - t\right)/2m_2, \end{aligned} \tag{A.9}$$

which in combination with Eqs. A.7 result in

$$\begin{aligned} |\overrightarrow{p_1}^{LAB}| &= \omega\left(s, {m_1}^2, {m_2}^2\right)/2m_2, \\ |\overrightarrow{p_3}^{LAB}| &= \omega\left(u, {m_2}^2, {m_3}^2\right)/2m_2, \\ |\overrightarrow{p_4}^{LAB}| &= \omega\left(t, {m_2}^2, {m_4}^2\right)/2m_2. \end{aligned} \tag{A.10}$$

Furthermore, from Eqs. A.7 we can also get the corresponding CM energies as

follows:

$$\begin{aligned} {E_1}^{CM} &= \left(s + {m_1}^2 - {m_2}^2\right)/2\sqrt{s}, \\ {E_2}^{CM} &= \left(s - {m_1}^2 + {m_2}^2\right)/2\sqrt{s}, \\ {E_3}^{CM} &= \left(s + {m_3}^2 - {m_4}^2\right)/2\sqrt{s}, \\ {E_4}^{CM} &= \left(s - {m_3}^2 + {m_4}^2\right)/2\sqrt{s}. \end{aligned} \tag{A.11}$$

Therefore, using Eqs. A.5 and A.7 and the expressions for ${E_1}^{CM}$ and ${E_3}^{CM}$ from Eq. A.11, we can calculate the scattering angle in CM frame in terms of the kinematical invariants as follows:

$$\cos\left(\theta^{CM}\right) = \frac{\overrightarrow{p_1}^{CM} \cdot \overrightarrow{p_3}^{CM}}{|\overrightarrow{p_1}^{CM}||\overrightarrow{p_3}^{CM}|} \tag{A.12}$$

$$= \frac{s^2 + s\left(2t - {m_1}^2 - {m_2}^2 - {m_3}^2 - {m_4}^2\right) + \left({m_1}^2 - {m_2}^2\right)\left({m_3}^2 - {m_4}^2\right)}{\omega\left(s, {m_1}^2, {m_2}^2\right) \cdot \omega\left(s, {m_3}^2, {m_4}^2\right)}.$$

Similarly, for the scattering angle in LAB frame we obtain

$$\cos\left(\theta^{LAB}\right) = \frac{\overrightarrow{p_1}^{LAB} \cdot \overrightarrow{p_3}^{LAB}}{|\overrightarrow{p_1}^{LAB}||\overrightarrow{p_3}^{LAB}|} \tag{A.13}$$

$$= \frac{\left(s - {m_1}^2 - {m_2}^2\right)\left({m_2}^2 + {m_3}^2 - u\right) + 2{m_2}^2\left({m_2}^2 + {m_4}^2 - s - u\right)}{\omega\left(s, {m_1}^2, {m_2}^2\right) \cdot \omega\left(u, {m_2}^2, {m_3}^2\right)}.$$

It is convenient to have the functional form of the total energy of the outgoing particle $\left({E_3}^{LAB}\right.$ or $\left.{E_4}^{LAB}\right)$ versus the scattering angle in LAB. Substituting for $s$ and $u$ from Eqs. A.4 and A.6 into Eq. A.13, we will have

$$2\cos\left(\theta^{LAB}\right) = \frac{a{E_3}^{LAB} + b}{\sqrt{c\left(\left({E_3}^{LAB}\right)^2 - {m_3}^2\right)}}, \tag{A.14}$$

in which

$$a = 2\left({E_1}^{LAB} + m_2\right),\ b = {m_4}^2 - {m_1}^2 - {m_2}^2 - {m_3}^2 - 2m_2{E_1}^{LAB},\ c = \left({E_1}^{LAB}\right)^2 - {m_1}^2. \tag{A.15}$$

Subsequently, from Eq. A.14 we obtain

$${E_3}^{LAB} = \frac{-ab \pm 2\cos\left(\theta^{LAB}\right) \cdot \sqrt{4c^2{m_3}^2 \cdot \cos^2\left(\theta^{LAB}\right) + c\left(b^2 - a^2{m_3}^2\right)}}{a^2 - 4c \cdot \cos^2\left(\theta^{LAB}\right)}. \tag{A.16}$$

The functional form of ${E_3}^{LAB}$ versus $\theta^{LAB}$ in Eq. A.16 shows that there could be a turning point for $\theta^{LAB}$ as ${E_3}^{LAB}$ increases from zero to higher values. The angle,

$\theta_0^{LAB}$, at which the turning happens can easily be calculated from this expression to be:

$$\theta_0^{LAB} = \cos^{-1}\left(\frac{\sqrt{a^2{m_3}^2 - b^2}}{2m_3\sqrt{c}}\right) \equiv \cos^{-1}\left(\sqrt{\frac{P}{Q}}\right), \tag{A.17}$$

with

$$P = 4\left({m_3}^2 - {m_2}^2\right)\left({E_1}^{LAB}\right)^2 + 4m_2\left({m_3}^2 - {m_2}^2 + {m_4}^2 - {m_1}^2\right)\left({E_1}^{LAB}\right) + \left(2{m_3}^2\left({m_2}^2 - {m_1}^2\right) + 2{m_4}^2\left({m_2}^2 + {m_1}^2\right) - \left({m_1}^2 + {m_2}^2\right)^2 - \left({m_3}^2 - {m_4}^2\right)^2\right)$$

and

$$Q = 4{m_3}^2\left(\left({E_1}^{LAB}\right)^2 - {m_1}^2\right). \tag{A.18}$$

Once we have ${E_3}^{LAB}$ versus $\theta^{LAB}$ (scattering angle of particle #3), we can easily calculate ${E_4}^{LAB}$ versus $\theta^{LAB}$ by making use of the following relation:

$${E_4}^{LAB} = {E_1}^{LAB} + m_2 - {E_3}^{LAB}. \tag{A.19}$$

It might also be of interest to calculate $\theta^{LAB}$ versus $\theta^{CM}$. This we can do by making use of Eqs. A.12 and A.13:

$$\cos\left(\theta^{LAB}\right) = \cos\left(\theta^{CM}\right) \times \frac{\omega\left(s, {m_3}^2, {m_4}^2\right)}{\omega\left(u, {m_2}^2, {m_3}^2\right)} \times \left(\frac{\left(s - {m_1}^2 - {m_2}^2\right)\left({m_2}^2 + {m_3}^2 - u\right) + 2{m_2}^2\left({m_2}^2 + {m_4}^2 - s - u\right)}{s^2 + s\left(2t - {m_1}^2 - {m_2}^2 - {m_3}^2 - {m_4}^2\right) + \left({m_1}^2 - {m_2}^2\right)\left({m_3}^2 - {m_4}^2\right)}\right). \tag{A.20}$$

### A.1.2 Transformation of cross sections

For a two-body reaction, $d\sigma/dt$ and $d\sigma/d\Omega$ are connected by:

$$d\sigma/dt = 2\pi\frac{d(\cos\theta)}{dt}\frac{d\sigma}{d\Omega}. \tag{A.21}$$

Equations A.12 and A.21 immediately give:

$$\left(d\sigma/d\Omega\right)^{CM} = \frac{1}{4\pi s}\omega\left(s, m_1^2, m_2^2\right)\cdot\omega\left(s, m_3^2, m_4^2\right)\frac{d\sigma}{dt}. \tag{A.22}$$

With the help of Eqs. A.9 and A.10, we introduce laboratory quantities and get:

$$d\sigma/dt = \frac{\pi\left(1+\frac{E_1^{LAB}}{m_2}-\cos\theta^{LAB}\frac{E_3^{LAB}}{m_2}\frac{|\overrightarrow{p_1}^{LAB}|}{|\overrightarrow{p_3}^{LAB}|}\right)}{|\overrightarrow{p_1}^{LAB}||\overrightarrow{p_3}^{LAB}|}\left(d\sigma/d\Omega\right)^{LAB}. \tag{A.23}$$

Rewriting Eq. A.22 and using Eq. A.23 we will have:

$$\begin{aligned}\left(\frac{d\sigma}{d\Omega}\right)_{normal}^{CM} &= \frac{1}{4\pi s}\cdot\omega\left(s,m_1^2,m_2^2\right)\cdot\omega\left(s,m_3^2,m_4^2\right)\left(\frac{d\sigma}{dt}\right)_{normal}\\ &\equiv \mathcal{J}_1\times\left(\frac{d\sigma}{d\Omega}\right)_{normal}^{LAB},\end{aligned} \tag{A.24}$$

with

$$\mathcal{J}_1 = \frac{\omega\left(s,m_1^2,m_2^2\right)\cdot\omega\left(s,m_3^2,m_4^2\right)}{4s\cdot|\overrightarrow{p}_1^{LAB}||\overrightarrow{p}_3^{LAB}|}\times\left(1+\frac{E_1^{LAB}}{m_2}-\cos\theta^{LAB}\frac{E_3^{LAB}}{m_2}\frac{|\overrightarrow{p}_1^{LAB}|}{|\overrightarrow{p}_3^{LAB}|}\right), \tag{A.25}$$

where "*normal*" stands for normal kinematics (light projectile on heavy target-particle) and $s = m_1^2 + m_2^2 + 2m_2E_1^{LAB}$. We can have the same expression for the inverse kinematics, where a heavy projectile impinges on the light target-particle (exchanging $m_1$ and $m_2$):

$$\left(\frac{d\sigma}{d\Omega}\right)_{inverse}^{CM} \equiv \mathcal{J}_{1,inv.}\times\left(\frac{d\sigma}{d\Omega}\right)_{inverse}^{LAB}, \tag{A.26}$$

with

$$\begin{aligned}\mathcal{J}_{1,inv.} = \frac{\omega\left(s_{inv.},m_2^2,m_1^2\right)\cdot\omega\left(s_{inv.},m_3^2,m_4^2\right)}{4s_{inv.}\cdot|\overrightarrow{p}_{1,inv.}^{LAB}||\overrightarrow{p}_{3,inv.}^{LAB}|}\times\\ \left(1+\frac{E_{1,inv.}^{LAB}}{m_1}-\cos\theta_{inv.}^{LAB}\frac{E_{3,inv.}^{LAB}}{m_1}\frac{|\overrightarrow{p}_{1,inv.}^{LAB}|}{|\overrightarrow{p}_{3,inv.}^{LAB}|}\right),\end{aligned} \tag{A.27}$$

in which $s_{inv.} = m_2^2 + m_1^2 + 2m_1E_{1,inv.}^{LAB}$ and "*inv.*" shows the respective quantity in inverse kinematics with the following numbering convention for the particles: particle #1 with mass $m_2$, particle #2 with mass $m_1$, particle #3 with mass $m_3$, and particle #4 with mass $m_4$. Hence, based on this notation, $E_{1,inv.}^{LAB}$ and $\overrightarrow{p}_{1,inv.}^{LAB}$ are the total energy of the beam particle (heavier than the target particle) and its 3-momentum in the LAB frame; $E_{3,inv.}^{LAB}$, $\overrightarrow{p}_{3,inv.}^{LAB}$, and $\theta_{inv.}^{LAB}$ are the total energy, 3-momentum, and scattering angle of the scattered light particle in the LAB frame.

We have also from Eq. A.22:

$$\frac{\left(\frac{d\sigma}{d\Omega}\right)^{CM}_{inverse} \cdot 4s_{inv.}}{\omega\left(s_{inv.}, m_2^2, m_1^2\right) \cdot \omega\left(s_{inv.}, m_3^2, m_4^2\right)} \equiv \frac{1}{\pi} \cdot \left(\frac{d\sigma}{dt}\right)_{inverse}, \tag{A.28}$$

which, using Eq. A.26, results in:

$$\left(\frac{d\sigma}{dt}\right)_{inverse} = \frac{\pi}{|\overrightarrow{p}^{LAB}_{1,inv.}||\overrightarrow{p}^{LAB}_{3,inv.}|} \times \left(1 + \frac{E^{LAB}_{1,inv.}}{m_1} - \cos\theta^{LAB}_{inv.} \frac{E^{LAB}_{3,inv.}}{m_1} \frac{|\overrightarrow{p}^{LAB}_{1,inv.}|}{|\overrightarrow{p}^{LAB}_{3,inv.}|}\right) \left(\frac{d\sigma}{d\Omega}\right)^{LAB}_{inverse}. \tag{A.29}$$

This, as well, could have been intuitively concluded from Eq. A.23, in which $d\sigma/dt$ and $(d\sigma/d\Omega)^{LAB}$ are for normal kinematics.

Now in Eq. A.29, $\left(\frac{d\sigma}{d\Omega}\right)^{LAB}_{inverse}$ can be obtained from Eqs. A.24 and A.26, using the intuitive fact that $\left(\frac{d\sigma}{d\Omega}\right)^{CM}_{normal} \equiv \left(\frac{d\sigma}{d\Omega}\right)^{CM}_{inverse}$, (which in turn translates into $s_{inv.} \equiv s$):

$$\left(\frac{d\sigma}{d\Omega}\right)^{LAB}_{inverse} = \left(\frac{d\sigma}{d\Omega}\right)^{LAB}_{normal} \times \mathcal{J}_2, \tag{A.30}$$

in which

$$\mathcal{J}_2 = \frac{|\overrightarrow{p}^{LAB}_{1,inv.}||\overrightarrow{p}^{LAB}_{3,inv.}|}{|\overrightarrow{p}^{LAB}_{1}||\overrightarrow{p}^{LAB}_{3}|} \times \frac{\left(1 + \frac{E^{LAB}_{1}}{m_2} - \cos\theta^{LAB} \frac{E^{LAB}_{3}}{m_2} \frac{|\overrightarrow{p}^{LAB}_{1}|}{|\overrightarrow{p}^{LAB}_{3}|}\right)}{\left(1 + \frac{E^{LAB}_{1,inv.}}{m_1} - \cos\theta^{LAB}_{inv.} \frac{E^{LAB}_{3,inv.}}{m_1} \frac{|\overrightarrow{p}^{LAB}_{1,inv.}|}{|\overrightarrow{p}^{LAB}_{3,inv.}|}\right)}. \tag{A.31}$$

This, using Eqs. A.29 and A.30, results in:

$$\left(\frac{d\sigma}{dt}\right)_{inverse} = \left(\frac{d\sigma}{d\Omega}\right)^{LAB}_{normal} \times \frac{\pi\left(1 + \frac{E^{LAB}_{1}}{m_2} - \cos\theta^{LAB} \frac{E^{LAB}_{3}}{m_2} \frac{|\overrightarrow{p}^{LAB}_{1}|}{|\overrightarrow{p}^{LAB}_{3}|}\right)}{|\overrightarrow{p}^{LAB}_{1}||\overrightarrow{p}^{LAB}_{3}|}, \tag{A.32}$$

which could be rewritten, using Eq. A.23, to give:

$$\left(\frac{d\sigma}{dt}\right)_{inverse} \equiv \left(\frac{d\sigma}{dt}\right)_{normal} = \left(\frac{d\sigma}{dt}\right). \tag{A.33}$$

Therefore, we can summarize Eq. A.23 as follows:

$$\left(\frac{d\sigma}{d\Omega}\right)^{LAB}_{normal} = \left(\frac{d\sigma}{dt}\right) \times \mathcal{J}_3, \quad \left(\frac{d\sigma}{d\Omega}\right)^{LAB}_{inverse} = \left(\frac{d\sigma}{dt}\right) \times \mathcal{J}_4. \tag{A.34}$$

in which

$$\mathcal{J}_3 = \frac{|\overrightarrow{p}_1^{LAB}||\overrightarrow{p}_3^{LAB}|}{\pi\left(1+\frac{E_1^{LAB}}{m_2}-\cos\theta^{LAB}\frac{E_3^{LAB}}{m_2}\frac{|\overrightarrow{p}_1^{LAB}|}{|\overrightarrow{p}_3^{LAB}|}\right)},$$
$$\mathcal{J}_4 = \frac{|\overrightarrow{p}_{1,inv.}^{LAB}||\overrightarrow{p}_{3,inv.}^{LAB}|}{\pi\left(1+\frac{E_{1,inv.}^{LAB}}{m_1}-\cos\theta_{inv.}^{LAB}\frac{E_{3,inv.}^{LAB}}{m_1}\frac{|\overrightarrow{p}_{1,inv.}^{LAB}|}{|\overrightarrow{p}_{3,inv.}^{LAB}|}\right)}. \tag{A.35}$$

## An example

In this subsection, we will try to derive a differential cross section as function of the scattering angle for a specific channel, using the experimental data available for some other reactions and having only one cross section point at one angle for our reaction of interest. Consider the reaction channel $^{56}$Ni$(p,n)^{56}$Cu with an excitation energy of 4 MeV. The calculation of Fig. 2.8 gives the cross section $d\sigma/dt$ at a single point (0.1° in normal kinematics or equivalently at 0.34° and 1.96° in inverse kinematics for 50 and 200 MeV/nucleon, respectively), which is 623 and 240 mb/(GeV)$^2$ for 4 MeV excitation energy at the beam energies of 50 and 200 MeV/nucleon, respectively. Thus, from Eq. A.34 we will have $\left(\frac{d\sigma}{d\Omega}\right)_{inverse}^{LAB} = 1.3078$ and 0.07896 mb/sr for these two energies, respectively. Having this single cross section point in inverse kinematics and exploiting the experimental cross section for $^{90}$Zr$(p,n)$ reaction in normal kinematics (Fig. A.2), we attempt to derive the cross section $\left(\frac{d\sigma}{d\Omega}\right)_{inverse}^{LAB}$ for the reaction channel $^{56}$Ni$(p,n)$. The way we do this is to normalize to the experimental data. From Eq. A.34 we obtain $\left(\frac{d\sigma}{d\Omega}\right)_{normal}^{LAB} = 14.65$ and 29.95 mb/sr for the beam energies of 50 and 200 MeV/nucleon, respectively. The normalization procedure is performed for the cross sections when represented as functions of $qR$, in which $q$ is the 3-momentum transfer and $R$ is the nuclear radius. At $\theta_{normal}^{LAB} = 0.1°$ we obtain $qR = 0.341$ and 0.170 GeV.fm/c for beam energies of 50 and 200 MeV/nucleon, respectively. Here, $R = 4.629$ fm is used as the radius of $^{56}$Ni nucleus. On the other hand, for the $^{90}$Zr$(p,n)$ reaction in normal kinematics at 295 MeV proton energy and $E_x = 10$ MeV and $\Delta L = 0$ we have $\left(\frac{d\sigma}{d\Omega}\right)_{normal}^{LAB} = 2.1$ and 7.26 mb/sr [21] at $qR_0 = 0.341$ and 0.170 GeV.fm/c, respectively, in which $R_0 = 5.422$ fm is the radius of $^{90}$Zr nucleus (see Tables A.1 and A.3). Therefore, the normalization factors for proton beam energies of 50 and 200 MeV are obtained to be $14.65/2.1 = 6.976$ and $29.95/7.26 = 4.125$, respectively. Tables A.1, A.2, and A.3 show the results of the normalization procedure for the proton beam energies of 50 and 200 MeV.

Fig. A.3 (top panel) shows the derived cross sections in normal kinematics (based on Tables A.1, A.2, and A.3) for the two beam energies. Using Eq. A.30 we can then extract the corresponding cross sections in inverse kinematics. Fig. A.3 (bottom panel) compares the results of this procedure with the actual theoretical prediction for the cross sections of $^{56}$Ni$(p,n)$ reaction at beam energies of 50 and

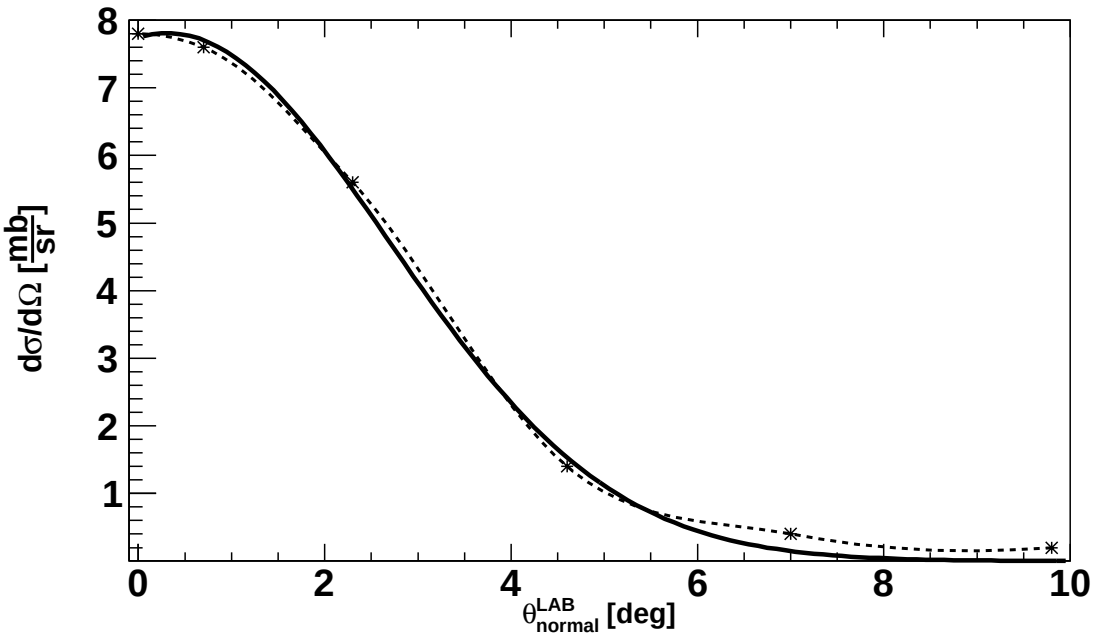


**Figure A.2:** Cross sections for the reaction channel $^{90}\mathrm{Zr}(p,n)$ in normal kinematics for the beam energy of 295 MeV and an excitation energy of $E_x = 10$ MeV with $\Delta L = 0$. The six data points shown here are the results of multipole-decomposition-analysis (MDA) and extracted from [21]. While the solid curve is a Gaussian fit to data points, the dotted curve is taken as the cross section in Tables A.1, A.2, and A.3, which is maximum at $\theta^{LAB}_{normal} = 0°$.

200 MeV/nucleon in inverse kinematics. The figure shows that the method of normalizing from one nucleus to another one is rather reliable for making rate estimates.

## A.2 Momentum transfer analysis in $^{136}\mathrm{Xe}\,(p,p)$

For a given $s$, both $t$ and $u$ depend linearly on the cosine of the CM scattering angle by:

$$\begin{aligned} -t &= 2E_1^{CM}E_3^{CM} - m_1^2 - m_3^2 - 2p_1^{CM}p_3^{CM}\cdot\cos\theta^{CM} \\ -u &= 2E_2^{CM}E_3^{CM} - m_2^2 - m_3^2 - 2p_2^{CM}p_3^{CM}\cdot\cos\theta^{CM}. \end{aligned} \tag{A.36}$$

In the case of elastic scattering $\left(m_1 = m_3 \text{ and } E_1^{CM} = E_3^{CM}\right)$ and again for fixed $s$ we can easily derive $t$, for it is an invariant variable which is the same in the LAB and CM frames:

$$-t = 2\left(p^{CM}\right)^2\left(1-\cos\theta^{CM}\right), \tag{A.37}$$

**Table A.1:** Calculation of the cross section of $^{56}$Ni$(p,n)$ for 4 MeV excitation energy in $^{56}$Cu in normal kinematics for $E_p = 200$ MeV through normalization to the available normal kinematics cross section of $^{90}$Zr$(p,n)$ with a beam energy of $E_p = 295$ MeV and an excitation energy of $E_x = 10$ MeV. The normalization factor at $\theta^{LAB}_{(^{56}\mathrm{Ni})} = 0.1^\circ$ was obtained to be 4.125 for this beam energy.

| $qR$ [GeV.fm/c] | $\theta^{LAB}_{(^{90}\mathrm{Zr})}$ [deg] | $^{90}$Zr$(p,n)$ $(d\sigma/d\Omega)^{LAB}_{normal}$ [mb/sr] | $^{56}$Ni$(p,n)$ $(d\sigma/d\Omega)^{LAB}_{normal}$ [mb/sr] | $\theta^{LAB}_{(^{56}\mathrm{Ni})}$ [deg] |
|---|---|---|---|---|
| 0.170 | 1.21 | 7.26 | 29.95 | 0.1 |
| 0.174 | 1.31 | 7.15 | 29.49 | 0.75 |
| 0.178 | 1.41 | 7.00 | 28.87 | 1.07 |
| 0.183 | 1.51 | 6.87 | 28.34 | 1.33 |
| 0.188 | 1.61 | 6.71 | 27.69 | 1.57 |
| 0.192 | 1.71 | 6.56 | 27.06 | 1.78 |
| 0.197 | 1.81 | 6.40 | 26.40 | 1.98 |
| 0.203 | 1.91 | 6.22 | 25.66 | 2.18 |
| 0.208 | 2.01 | 6.03 | 24.87 | 2.36 |
| 0.213 | 2.11 | 5.86 | 24.17 | 2.55 |
| 0.219 | 2.21 | 5.68 | 23.43 | 2.73 |
| 0.225 | 2.31 | 5.47 | 22.56 | 2.90 |
| 0.230 | 2.41 | 5.29 | 21.82 | 3.07 |
| 0.236 | 2.51 | 5.08 | 20.95 | 3.24 |
| 0.242 | 2.61 | 4.89 | 20.17 | 3.41 |
| 0.248 | 2.71 | 4.70 | 19.39 | 3.57 |
| 0.254 | 2.81 | 4.49 | 18.52 | 3.74 |
| 0.260 | 2.91 | 4.30 | 17.74 | 3.90 |
| 0.267 | 3.01 | 4.12 | 16.99 | 4.06 |
| 0.273 | 3.11 | 3.89 | 16.05 | 4.22 |
| 0.279 | 3.21 | 3.71 | 15.30 | 4.38 |
| 0.286 | 3.31 | 3.51 | 14.48 | 4.54 |
| 0.292 | 3.41 | 3.34 | 13.78 | 4.70 |
| 0.299 | 3.51 | 3.14 | 12.95 | 4.85 |
| 0.305 | 3.61 | 2.98 | 12.29 | 5.01 |
| 0.312 | 3.71 | 2.80 | 11.55 | 5.17 |

which has the bounds $0 \leq -t \leq 4\left(p^{CM}\right)^2$. Clearly, $p^{CM}$ is the 3-vector of momentum in the CM frame and can be calculated via

$$s = \left(E_1^{CM} + E_2^{CM}\right)^2 = \left(\sqrt{m_1^2 + \left(p^{CM}\right)^2} + \sqrt{m_2^2 + \left(p^{CM}\right)^2}\right)^2. \tag{A.38}$$

**Table A.2:** Continued from Table A.1.

| $qR$ [GeV.fm/c] | $\theta^{LAB}_{(^{90}\mathrm{Zr})}$ [deg] | $^{90}\mathrm{Zr}(p,n)$ $(d\sigma/d\Omega)^{LAB}_{normal}$ [mb/sr] | $^{56}\mathrm{Ni}(p,n)$ $(d\sigma/d\Omega)^{LAB}_{normal}$ [mb/sr] | $\theta^{LAB}_{(^{56}\mathrm{Ni})}$ [deg] |
|---|---|---|---|---|
| 0.318 | 3.81 | 2.64 | 10.89 | 5.32 |
| 0.325 | 3.91 | 2.47 | 10.19 | 5.48 |
| 0.332 | 4.01 | 2.31 | 9.53 | 5.63 |
| 0.338 | 4.11 | 2.18 | 8.99 | 5.78 |
| 0.345 | 4.21 | 2.03 | 8.37 | 5.94 |
| 0.352 | 4.31 | 1.88 | 7.75 | 6.09 |
| 0.359 | 4.41 | 1.76 | 7.26 | 6.24 |
| 0.366 | 4.51 | 1.63 | 6.72 | 6.40 |
| 0.372 | 4.61 | 1.52 | 6.27 | 6.55 |
| 0.379 | 4.71 | 1.40 | 5.77 | 6.71 |
| 0.386 | 4.81 | 1.29 | 5.32 | 6.86 |
| 0.393 | 4.91 | 1.20 | 4.95 | 7.01 |
| 0.400 | 5.01 | 1.10 | 4.54 | 7.16 |
| 0.407 | 5.11 | 1.01 | 4.17 | 7.31 |
| 0.414 | 5.21 | 0.93 | 3.84 | 7.46 |
| 0.421 | 5.31 | 0.85 | 3.51 | 7.62 |
| 0.428 | 5.41 | 0.78 | 3.22 | 7.77 |
| 0.435 | 5.51 | 0.70 | 2.89 | 7.92 |
| 0.442 | 5.61 | 0.65 | 2.68 | 8.07 |
| 0.449 | 5.71 | 0.59 | 2.43 | 8.22 |
| 0.456 | 5.81 | 0.54 | 2.23 | 8.37 |
| 0.463 | 5.91 | 0.48 | 1.98 | 8.52 |
| 0.470 | 6.01 | 0.43 | 1.77 | 8.67 |
| 0.477 | 6.11 | 0.40 | 1.65 | 8.82 |
| 0.484 | 6.21 | 0.36 | 1.48 | 8.98 |
| 0.491 | 6.31 | 0.32 | 1.32 | 9.13 |
| 0.499 | 6.41 | 0.29 | 1.20 | 9.28 |
| 0.506 | 6.51 | 0.26 | 1.07 | 9.43 |
| 0.513 | 6.61 | 0.23 | 0.95 | 9.57 |
| 0.520 | 6.71 | 0.21 | 0.87 | 9.73 |
| 0.527 | 6.81 | 0.19 | 0.78 | 9.88 |
| 0.534 | 6.91 | 0.16 | 0.66 | 10.03 |
| 0.541 | 7.01 | 0.15 | 0.62 | 10.17 |

**Table A.3:** Same as Table A.1 for 50 MeV/nucleon beam energy. The normalization factor at $\theta^{LAB}_{(^{56}\mathrm{Ni})} = 0.1^\circ$ was obtained to be 6.976.

| $qR$ [GeV.fm/c] | $\theta^{LAB}_{(^{90}\mathrm{Zr})}$ [deg] | $^{90}\mathrm{Zr}(p,n)$ $(d\sigma/d\Omega)^{LAB}_{normal}$ [mb/sr] | $^{56}\mathrm{Ni}(p,n)$ $(d\sigma/d\Omega)^{LAB}_{normal}$ [mb/sr] | $\theta^{LAB}_{(^{56}\mathrm{Ni})}$ [deg] |
|---|---|---|---|---|
| 0.341 | 4.15 | 2.1 | 14.65 | 0.1 |
| 0.345 | 4.21 | 2.03 | 14.16 | 2.41 |
| 0.352 | 4.31 | 1.88 | 13.11 | 3.95 |
| 0.359 | 4.41 | 1.76 | 12.28 | 5.06 |
| 0.365 | 4.51 | 1.63 | 11.37 | 5.99 |
| 0.372 | 4.61 | 1.52 | 10.60 | 6.81 |
| 0.379 | 4.71 | 1.40 | 9.77 | 7.56 |
| 0.386 | 4.81 | 1.29 | 9.00 | 8.25 |
| 0.393 | 4.91 | 1.20 | 8.37 | 8.91 |
| 0.400 | 5.01 | 1.10 | 7.67 | 9.53 |
| 0.407 | 5.11 | 1.01 | 7.05 | 10.12 |
| 0.414 | 5.21 | 0.93 | 6.49 | 10.70 |
| 0.421 | 5.31 | 0.85 | 5.93 | 11.26 |
| 0.428 | 5.41 | 0.78 | 5.44 | 11.79 |
| 0.435 | 5.51 | 0.70 | 4.88 | 12.32 |
| 0.442 | 5.61 | 0.65 | 4.53 | 12.83 |
| 0.449 | 5.71 | 0.59 | 4.12 | 13.33 |
| 0.456 | 5.81 | 0.54 | 3.77 | 13.82 |
| 0.463 | 5.91 | 0.48 | 3.35 | 14.31 |
| 0.470 | 6.01 | 0.43 | 3.00 | 14.78 |
| 0.477 | 6.11 | 0.40 | 2.79 | 15.25 |
| 0.484 | 6.21 | 0.36 | 2.51 | 15.71 |
| 0.491 | 6.31 | 0.32 | 2.23 | 16.17 |
| 0.499 | 6.41 | 0.29 | 2.02 | 16.63 |
| 0.506 | 6.51 | 0.26 | 1.81 | 17.07 |
| 0.513 | 6.61 | 0.23 | 1.60 | 17.52 |
| 0.520 | 6.71 | 0.21 | 1.46 | 17.95 |
| 0.527 | 6.81 | 0.19 | 1.32 | 18.39 |
| 0.534 | 6.91 | 0.16 | 1.12 | 18.82 |
| 0.541 | 7.01 | 0.15 | 1.05 | 19.25 |

For a frame (e.g., CM) moving along an arbitrary $z$-direction we have $E^{CM} = \gamma(E - vp_z)$, in which $v$, $E$, and $p_z$ are the velocity of the frame, the particle energy, and $z$-component of particle momentum in LAB (target) frame; $E^{CM}$ is the energy

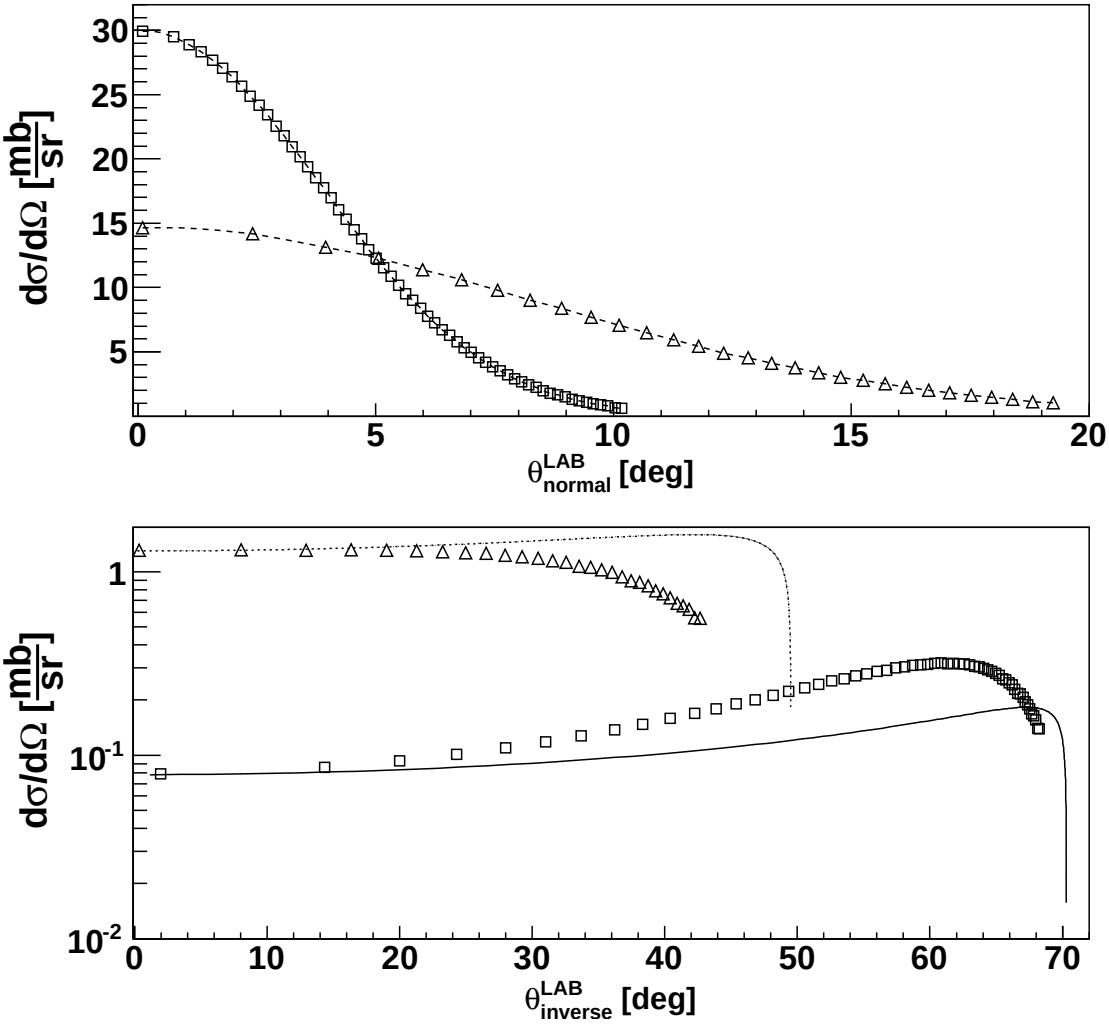


**Figure A.3:** Top: Cross section of the reaction channel $^{56}$Ni$(p, n)$ in normal kinematics for the proton energies of 50 (triangles) and 200 MeV (squares) and an excitation energy of 4 MeV, derived through normalization to the experimental data of Fig. A.2. Bottom: theoretical prediction for the cross section in inverse kinematics for the reaction channel $^{56}$Ni$(p, n)$ with beam energies of 50 (dotted curve) and 200 MeV/nucleon (solid curve) [19]. For comparison the extracted cross sections from the method of normalization to experimental data is also shown for the beam energies of 50 (triangles) and 200 MeV/nucleon (squares). For an extensive discussion on the derivation of the method, see the text.

of particle in CM frame. Alternatively, we can have the following transformations:

$$E = \gamma \left( E^{CM} + v p_z^{CM} \right), \; p_z = \gamma \left( p_z^{CM} + \beta E^{CM} \right), \; p_y = p_y^{CM}, \text{ and } p_x = p_x^{CM}, \quad \text{(A.39)}$$

with $\gamma = \left(1 - (v/c)^2\right)^{-1/2}$ and $c = 1$ in natural units. Consequently,

$$\tan\left(\theta^{LAB}\right) = \frac{\sqrt{p_x^2 + p_y^2}}{p_z} = \frac{\tan\left(\theta^{CM}\right)}{\gamma^{LAB}\left(1 + \frac{v \cdot E^{CM}}{p_z^{CM}}\right)}, \tag{A.40}$$

in which $\theta^{LAB}$ ($\theta^{CM}$) is the scattering angle in the laboratory (center-of-mass) frame and $v$ is the velocity of the CM frame relative to the LAB frame (hence substituting $\gamma$ and $\beta$ with $\gamma^{LAB}$ and $\beta^{LAB}$). Therefore, for a two-body scattering we would have

$$\tan\left(\theta_i^{LAB}\right) = \frac{\tan\left(\theta_i^{CM}\right)}{\gamma^{LAB}\left(1 + \frac{v \cdot E_i^{CM}}{p_i^{CM} \cdot \cos\left(\theta^{CM}\right)}\right)}, \qquad i = 1, 2 \tag{A.41}$$

in which $|p_1^{CM}| = |p_2^{CM}| = p^{CM}$ and $\theta_2^{CM} = \pi - \theta_1^{CM}$. Therefore,

$$\tan\left(\theta_i^{LAB}\right) = \frac{\sin\left(\theta_i^{CM}\right)}{\gamma^{LAB}\left(\cos\left(\theta_i^{CM}\right) + \beta^{LAB}\frac{E_i^{CM}}{p^{CM}}\right)}, \qquad i = 1, 2 \tag{A.42}$$

The 4-momenta of the beam particle, moving in $z$-direction, and the target particle, fixed in LAB, can be written as

$$p_1 = (E_1, 0, 0, p_z) \quad , \quad p_2 = (E_2, 0, 0, 0) \tag{A.43}$$

Hence,

$$s = {m_1}^2 + {m_2}^2 + 2m_2\left(m_1 + K_b\right), \tag{A.44}$$

in which $K_b$ is the kinetic energy of the beam particle in LAB. Therefore, from Eqs. A.38 and A.44 we can calculate $p^{CM}$, $\beta^{LAB}$, and $\gamma^{LAB}$. For a $^{136}$Xe beam energy of 350 MeV/nucleon these parameters are obtained to be 0.8779 GeV, 0.6832, and 1.3695, respectively. On the other hand, from Eq. A.37, $-t$ is given by the following relations:

$$\begin{aligned} -t &= 2\left(p^{CM}\right)^2\left(1 - \cos\left(\theta_{ion}^{CM}\right)\right) \\ &= 2\left(p^{CM}\right)^2\left(1 + \cos\left(\theta_p^{CM}\right)\right), \end{aligned} \tag{A.45}$$

since in our case, the beam (ion) is moving in $z$-direction and the target (proton) is fixed. Therefore,

$$\tan\left(\theta_{ion}^{LAB}\right) = \frac{\sqrt{(-t) - \frac{(-t)^2}{4\left(p^{CM}\right)^2}}}{\gamma^{LAB}\left(p^{CM} - \frac{(-t)}{2p^{CM}} + \beta^{LAB}\sqrt{\left(p^{CM}\right)^2 + \left(m_{ion}\right)^2}\right)}, \tag{A.46}$$

$$\tan\left(\theta_p^{LAB}\right) = \frac{\sqrt{(-t) - \frac{(-t)^2}{4(p^{CM})^2}}}{\gamma^{LAB}\left(\frac{(-t)}{2p^{CM}} - p^{CM} + \beta^{LAB}\sqrt{(p^{CM})^2 + (m_p)^2}\right)}, \tag{A.47}$$

in which $\theta_{ion}^{LAB}$ and $\theta_p^{LAB}$ are the $^{136}$Xe and proton scattering angles in LAB, and $m_{ion} = 126.5962$ GeV and $m_p = 0.9383$ GeV are their respective rest masses. We can also calculate $-t$ with respect to $\theta_p^{LAB}$ from Eq. A.42, knowing that for the elastically-scattered proton, we expect $\theta_p^{CM} > \pi/2$ (in the CM frame, the $z$-component of the proton momentum is negative):

$$\tan\left(\theta_p^{LAB}\right) = \frac{\sin\left(\theta_p^{CM}\right)}{\gamma^{LAB}\left(b + \cos\left(\theta_p^{CM}\right)\right)}, \tag{A.48}$$

in which $b = \beta^{LAB}\frac{E_p^{CM}}{p^{CM}} = 1$, since $p^{CM} = m_p^{CM}\beta^{LAB}$ and $m_p^{CM} \equiv E_p^{CM}$. Thus, from Eqs. A.45 and A.48 we obtain

$$-t = 4\left(p^{CM}\right)^2\left(\frac{1}{1 + \left(\gamma^{LAB}\right)^2 \cdot \tan^2\left(\theta_p^{LAB}\right)}\right). \tag{A.49}$$

It is also possible to calculate $-t$ versus the proton kinetic energy $(K_p^{LAB})$ after collision with the heavy ion:

$$E_p^{LAB} = \gamma^{LAB}\left(E_p^{CM} + \beta^{LAB}p^{CM} \cdot \cos\left(\theta_p^{CM}\right)\right), \tag{A.50}$$

with $E_p^{CM} = \sqrt{m_p^2 + (p^{CM})^2}$. Thus,

$$K_p^{LAB} = \gamma^{LAB}\left(\gamma^{LAB}m_p + \beta^{LAB}p^{CM} \cdot \cos\left(\theta_p^{CM}\right)\right) - m_p, \tag{A.51}$$

since before the collision, proton is assumed to be at rest $\left(E_p^{CM} = \gamma^{LAB}m_p\right)$. Thus,

$$2m_pK_p^{LAB} = 2\left(p^{CM}\right)^2\left(1 + \cos\left(\theta_p^{CM}\right)\right) \equiv -t, \tag{A.52}$$

using the fact that $m_p\gamma^{LAB} \equiv m_p^{CM}$.

# B. Reaction rates

An often used quantity in storage ring experiments is the integrated luminosity $\int \mathcal{L}dt$. The number of reactions which can be observed in a given reaction time is just the product of the integrated luminosity and the cross section. For a specific reaction channel, the total reaction rate is

$$\dot{N} = \mathcal{L} \cdot \int_{\text{whole phase space}} (d\sigma/d\Omega)\Delta\Omega = \mathcal{L}(2\pi) \int_0^\pi (d\sigma/d\Omega)d\theta \cdot \sin\theta. \tag{B.1}$$

Considering $\mathcal{L} = x \times 10^{28}$ cm$^{-2}$s$^{-1}$, we will have $\mathcal{L} = 10x$ mb$^{-1}$s$^{-1}$ which results in

$$\dot{N} = 20\pi x \int (d\sigma/d\Omega)d\theta \cdot \sin\theta, \tag{B.2}$$

in which $d\sigma/d\Omega$ should be inserted in units of mb/sr. Equivalently,

$$\dot{N} = (20\pi x) \sum_i (d\sigma/d\Omega)_i (\Delta\theta)_i \sin\theta_i, \tag{B.3}$$

in which $\theta_i$ runs over the whole phase space of the respective cross section. Choosing $(\Delta\theta)_i = 2^\circ$, we will end up with

$$\dot{N} = (20\pi x)(2/180)\pi \sum_i \sin\theta_i \cdot (d\sigma/d\Omega)_i, \tag{B.4}$$

in which $(d\sigma/d\Omega)_i$ is, in principle, the mean value of every $(d\sigma/d\Omega)_j$ inside the $(\Delta\theta)_i$ at a specific $\theta_i$.

In practice, only a fraction of all the reactions is observed by detectors. Thus, the observed reaction rate by a detector at $\theta_i$ would be

$$\Delta\dot{N}_{\text{observed}} = a_i(2\pi^2/9)x \cdot (d\sigma/d\Omega)_i \cdot \sin\theta_i, \tag{B.5}$$

in which $a_i$ ("detector acceptance") is the ratio of the number of detected light ejectiles generated at $\theta_i$ to the total number of generated light ejectiles at $\theta_i$. Thus, the total reaction rate detected by the detector is

$$\dot{N}_{\text{observed}} = \sum_i (\Delta\dot{N})_i^{\text{observed}} = (2\pi^2/9)x \cdot \sum_i a_i (d\sigma/d\Omega)_i \cdot \sin\theta_i. \tag{B.6}$$

# Bibliography


[1] J. Al-Khalili and E. Roeckl, *The Euroschool Lectures on Physics with Exotic Beams, Vol. II* (Springer-Verlag, Berlin, 2006).

[2] P. Egelhof, O. Kiselev, S. R. Neumaier G. Münzenberg, and H. Weick, Physica Scripta **T104**, 151 (2003).

[3] I. Tanihata *et al.*, Phys. Rev. Lett. **55**, 2676 (1985).

[4] I. Tanihata *et al.*, Phys. Lett. B **160**, 380 (1985).

[5] P. Egelhof, PRAMANA-journal of physics **53**, 365 (1999).

[6] *FAIR Baseline Technical Report, GSI Darmstadt*, 2006.

[7] *Technical Proposal for the Design, Construction, Commissioning and Operation of the EXL Project*, 2006.

[8] http://www-ap.gsi.de/research/posters/jet/index.html.

[9] S. Ilieva, Ph.D. thesis, University of Mainz, 2009.

[10] A. Bleile *et al.*, GSI Scientific Report, p. 92 (2004).

[11] S. Ilieva, O. Kiselev, H. Emling, P. Egelhof, K. Boretzky, J. P. Meier, H. Simon, K. Mahata, T. Le Bleis, A. Chatillon, F. Aksouh, K. Beckert, P. Beller, C. Kozhuharova, Y. Litvinov, X.C. Le Xuang, F. Nolden, M. Steck, T. Stöhlker, G. Ickert, U. Popp, H. Weick, D. Kiselev, J. Jourdan, D. Werthmüller, H. Moeini, A. Zalite, S. Paschalis, and the EXL collaboration, Eur. Phys. J. Special Topics **150**, 357 (2007).

[12] I. Hřivnáčová *et al.*, Proc. of Computing in High Energy and Nuclear Physics (La Jolla) Id THJT006 (2003).

[13] R. J. Glauber, in: Lectures in theoretical physics, Vol. I, eds. W. E. Brittin *et al.* (Interscience Publishers, New York, 1959), p. 315 .

[14] G. Colò, private communication.

[15] J.M. Udias, private communication.

[16] P. Egelhof, Progress in Particle and Nuclear Physics **46**, 307 (2001).

[17] A. Ozawa, T. Suzuki, and I. Tanihata, Nucl. Phys. **A693**, 32 (2001).

[18] M. Lindemulder, private communication, 2010.

[19] J.R. Vignote, J.M. Udias, and P. Sarriguren, private communication.

[20] A. M. Baldin, V. I. Gol'danskii, and I. L. Rozenthal, *Kinematics of nuclear reactions* (Pergamon Press, Oxford, New York, 1961).

[21] M. N. Harakeh and A. van der Woude, *Giant Resonances* (Oxford University Press, Oxford, 2001).